Laboratory for Atmospheric and Space Physics

University of Colorado
Boulder, Colorado

National Aeronautics and Space Administration
Total and Spectral Solar Irradiance Sensor
(NASA TSIS-1)

Algorithm Theoretical Basis Document

Document No. 151430 Date: June 30th, 2017

Prepared by Odele M. Coddington Date _____

Approved by _____ Date _____

Approved by _____ Date _____

Approved by _____ Date _____

Approved by _____ Date _____

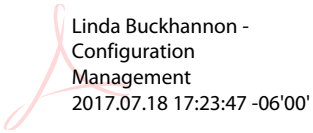

Revisions

Rev	Description of Change	By	Approved	Date
2	revisions requested by reviewers for v2 submission	Odele Coddington		June 14, 2017
A	Formal release with revisions requested by GSFC	Odele Coddington		June 30, 2017
A	Minor editorial revisions addressed	Odele Coddington		July 10, 2017

Contents

List of Figures

List of Tables

1 Introduction

1.1 Purpose of this Document

This Algorithm Theoretical Basis Document (ATBD) describes the algorithms used to produce all data levels of solar and spectral irradiance for the Total Solar Irradiance Sensor (TSIS) instrument complement. The current state of understanding of total and spectral solar irradiance is summarized and the scientific motivations and objectives for the TSIS mission are described. A brief introduction to the instruments is provided in order to aid the understanding of the detailed measurement algorithms including the instrument characterization and calibration that is needed to convert measured signal to irradiance units. The ATBD also describes the predicted science and housekeeping operation modes and the plan to monitor and correct for instrument degradation. The ATBD is not meant to be the sole reference for the TSIS instruments, data and their algorithms. Other documents will be generated to explain, in much greater detail than presented here, instrument design and operation, instrument calibration, and the ground data system. These related documents should be consulted to complement the information contained here. This ATBD provides one step towards insuring proper data stewardship of measurements of total and spectral solar irradiance since a well-documented calibration history will allow for the comparison and evaluation of the TSIS instruments to their future analogs.

1.2 Scope

This document describes those algorithms required to generate solar spectral and total irradiance data sets from direct observations of the Sun from space. The algorithms are described as they are known during the design phase of the instruments. Future changes in instrument design and results of laboratory calibration and testing may incur modifications to parts of certain algorithms.

1.3 Applicable Documents

A number of documents (listed below) presently exist or are being developed to complement this ATBD.

Table 1: Related Documents

Document Name	**Document #**
TSIS Level 1 Requirements	TSIS Joint L1RD, v1.1, August 16, 2011
TSIS Performance Specification	109170
TSIS Science and Mission Requirements	NCS-421-005
TSIS SIM Calibration and Validation Plan, Rev A	LASP Engineering Document No. 141313
TSIS SIM Flight ESR Calibration	LASP Engineering Document No. 141313
NIST L-1 Cryo to LASP L-1 Cryo Trap Transfer	LASP Engineering Document No. 151431
Report of Calibration SIM Apertures	NIST Test No: 685/281015-11
TSIS Project Data Management Plan	LASP Engineering Document No. 145520
TSIS Instrument Operations Concept	110249
International Space Station Guidance Navigation and Control System Memo for Payloads-July 2015	NASA Document EG-15-22
TIM Handbook	GLO-S-44030
SORCE Algorithm Theoretical Basis Document	20560-T6-0006
The Solar Radiation and Climate Experiments (SORCE)	*Solar Physics* (2005) special issue

1.4 Contributing Authors

Peter Pilewskie	Principal Investigator
Erik Richard	SIM Instrument Scientist
Greg Kopp	TIM Instrument Scientist
David Harber	Calibration Scientist
Karl Heuerman	Calibration Scientist
Odele Coddington	Instrument Scientist
Ed Hartnett	TSIS Ground System Manager
Stéphane Beland	Science Data Processing
Kim Kokkonen	Science Data Processing

2 Overview and Background Information

2.1 The Role of the Sun

The Sun is the dominant energy source for the Earth. The next dominant energy source is heat flux from the Earth's interior, which contributes roughly only 0.03% with respect to the total solar irradiance [*Sellers,* 1965; *Kren et al*., 2017]. The Sun varies on timescales ranging from minutes to decades. The dominant cycle in total solar irradiance (TSI) is approximately 11-years in length, with peak-to-peak amplitudes of 0.1%. A visible manifestation of solar variability is the appearance of dark sunspots and bright faculae on the Sun's surface, which are caused by magnetic phenomena within the Sun that pass across the solar disk as the Sun rotates in an approximate 27-day period, producing larger variations in energy output of roughly 0.2%. Variability also exists at shorter time scales related to eruptive events such as solar flares [*Hock*, 2012] and at century (and longer) time scales as indirectly evidenced by isotopic tracer proxies such as beryllium [*Uroskin*, 2013].

Solar energy is distributed across wavelengths spanning gamma rays (10^{-10} m) through radio waves (> 100 m). However, as shown in Figure 1 roughly 97% of the total solar energy occurs at the ultraviolet (UV), visible, and near-infrared portions (~200-2400 nm) of the spectrum [*Harder et al*., 2009]. The relative variability in solar spectral irradiance (SSI: 200-2400 nm) over the solar cycle can span 5 orders of magnitude greatly surpassing the variability in TSI [*Harder et al*., 2009; *Coddington et al*., 2016].

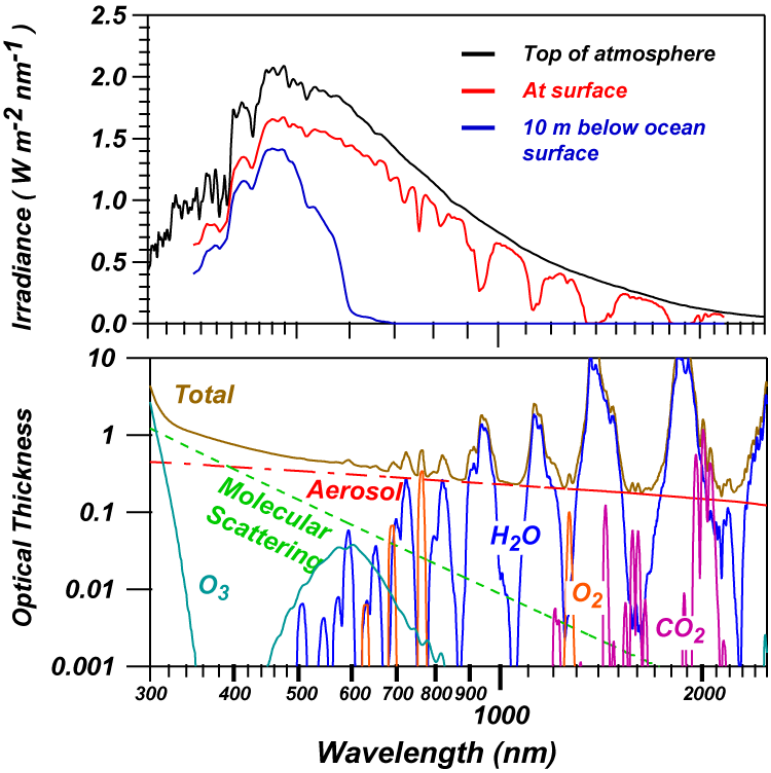

Figure 1: The wavelength-dependency of solar radiation at various levels within the Earth system: The dependency is due to the scattering and absorption of the sunlight induced by aerosols, the surface, and vertical profiles of molecular gas species. The strong absorption bands in the infrared are predominantly due to water vapor, with oxygen (O_2), carbon dioxide (CO_2), and methane also playing a role. The complete extinction of radiation at wavelengths shorter than ~300 nm is due to ozone (O_3).

Because of selective absorption and scattering processes in the Earth's atmosphere, the climate system responds in distinct ways to solar energy inputs in different spectral regions. The Earth's atmosphere absorbs completely solar radiation in the ultraviolet (UV) spectrum at wavelengths shortward of 315 nm. This radiation becomes the dominant direct energy input to the middle atmosphere and plays a major role in the physical processes there — including the photochemistry, dynamics, temperature, composition and structure. It is critical for both the formation and destruction of ozone. Even small changes in the incoming solar UV radiation produce commensurate changes in middle atmosphere parameters. Longer wavelength visible and near infrared radiation penetrates to the lower atmosphere and to the Earth's surface. When averaged over the globe, roughly half of the incoming solar radiation is either absorbed in the atmosphere or scattered back into space, the remaining half being absorbed at the surface. Since atmospheric scattering and absorption processes are all wavelength-dependent, it is essential to understand the variation of the Sun's radiation as a function of wavelength to properly understand the physical processes by which solar irradiance variability may influence climate. Solar ultraviolet radiation comprises less than 1% of TSI, yet may account for 30% of its 11-year cycle variation. From a combination of observations and model calculations *Trenberth et al.* [2009], *Stephens et al*., [2012] and *Wild et al*. [2013] suggest that approximately 22-23% of the TSI is absorbed principally by clouds, stratospheric ozone and other minor constituents, and tropospheric water vapor - all processes that are strongly wavelength dependent (see also Figure 1).

To accurately understand the Sun's role in Earth's climate, knowledge in both the total energy and its spectral distribution are required. Implications of a solar role are evident in most climate records [*Lean et al*., 2005]. Two proposed mechanisms of solar variability on climate include the top-down [*Gray et al*., 2010] and bottom-up [*Meehl et al*., 2009] mechanisms. In the top-down mechanism, the transfer of energy at ultraviolet wavelengths into the

stratosphere impacts the formation of ozone at these altitudes; a process which releases energy into the stratosphere that is transferred to the troposphere by stratospheric-tropospheric coupling [*Gray et al*., 2010]. In the bottom-up mechanism, localized increases in surface heating (such as cloud-free regions in the subtropical oceans) occur from increases in total solar irradiance at solar maximum conditions and impact the overarching Hadley and Walker circulation cells to ultimately affect winds, clouds, and precipitation patterns.

Evidence suggests that reductions in the Sun's energy have had a large impact on Earth's historic climate. A period of time (the Maunder Minimum: 1645-1715) with little to no sunspots and a reduction of solar irradiance by 0.24% [*Lean et al.,* 1995] has been correlated to a time where European winters were much colder and glacial activity progressed further south [*Eddy*, 1976; *Lean and Rind*, 1998]. There are various estimates of the increase in TSI from the Maunder Minimum to contemporary times ranging from 0.002% to 0.2% [*Feulner*, 2011; *Judge et al*., 2012]. Correlations between surface temperatures and solar activity have decreased in present times, a fact that is thought to be due to the increasing influence of anthropogenic emissions [*Reid*, 1991, 1997; *Lean et al*., 1995].

Determining the Sun's role in climate variability and change will require uninterrupted time series measurements of total and spectral solar irradiance that are of sufficient length, consistency, and continuity. Gaps in the time series of TSI will prohibit the construction of composite data sets inducing large uncertainties that will hamper insight into the true variability of TSI. The uncertainties arise from the use of ambiguous proxy or model data that would be needed to fill a gap and because the instrumental record would rely on individual, instrument accuracies in bridging any breaks in the data.

The TSIS TIM and SIM instruments are designed with the requirements needed to detect possible long-term solar variability in mind. *Kopp and Lean* [2011] discusses the uncertainties that will be induced in the current total solar irradiance record through undesirable gaps in the continuous measurement record. A TSI Calibration Transfer Experiment (TCTE), where the SORCE TIM "witness" unit that was launched late 2013 helps to bridge the gap between the SORCE and TSIS measurement records albeit with increased uncertainty than TSIS TIM. .

2.2 Recent Observations of Solar Variability

2.2.1 SORCE and Glory Contributions to Observations of Total Solar Irradiance

Prior to measurements obtained by the Solar Radiation and Climate Experiment (SORCE), launched in 2003, a generally accepted value for the total solar irradiance arriving at the top of the Earth's atmosphere was 1366 Wm^{-2} with an uncertainty of ±2 Wm^{-2} providing a globally averaged value of 342 Wm^{-2}. A significant SORCE contribution has been a decrease in the magnitude and uncertainty attributed to the total solar irradiance at the top of the atmosphere. This mean value is now accepted to be 1361 W m^{-2} with an uncertainty of 0.01% [*Kopp and Lean*, 2011], providing a globally averaged value nearer to 340 W m^{-2}.

A continuous record of total solar irradiance exists now for more than 38 years from space-based observations, shown in Figure 2 (left plot) from *http://spot.colorado.edu/~koppg/TSI/* (url last accessed 03/27/2017). Evident in this combined record is an 11-year cycle with peak-to-peak amplitude on the order of 0.1% due to magnetic activity in the photosphere with a positive contribution originating in the bright faculae and a negative contribution from the dark sunspots [*Rottman*, 2006]. Shorter-term variations are a factor of 2 to 3 greater on monthly time scales associated with the passage of dark sunspots across the disk of the Sun. The shorter-term variability is far more prominent when sunspots are abundant during solar maximum conditions. TSI variability occurs over essentially all time scales observed thus far, from minutes to the 11-year solar cycle.

The TSI record spread in Figure 2 (left plot) exceeds the variability in the 11-year cycle and is largely of instrumental origin. The individual TSI datasets from 1978 to the present time include observations made by ERB on Nimbus-7, ACRIM-I on SMM, ERBE on the ERBS satellite, solar monitors on NOAA 9 and NOAA 10, ACRIM-II on UARS, the SOVA2 on EUREKA, VIRGO on SOHO, ACRIM III on ACRIMSAT, TIM on SORCE, SOVIM on SOLAR,

PREMOS and SOVAP on PICARD, and TIM on TCTE [*Kyle et al*., 1993, *Willson*, 1994, *Fröhlich*, 1994, *Lee et al.*, 1995, *Fröhlich*, 1996, *Willson*, 2001, *Kopp et al*., 2005, and *Schmutz et al*., 2009]. These data were all recorded with ambient temperature sensors, each of which has its own individual instrumental error budget, typically on the order of 0.2 to 0.3% (2000 to 3000 ppm). The offsets are a result of slight differences in the calibration and traceability of each instrument to the SI units of Watt and meter squared, and to instrumental effects such as scattered light contributions [*Rottman*, 2006]. SOHO/VIRGO, SORCE/TIM and TCTE/TIM continue to make observations.

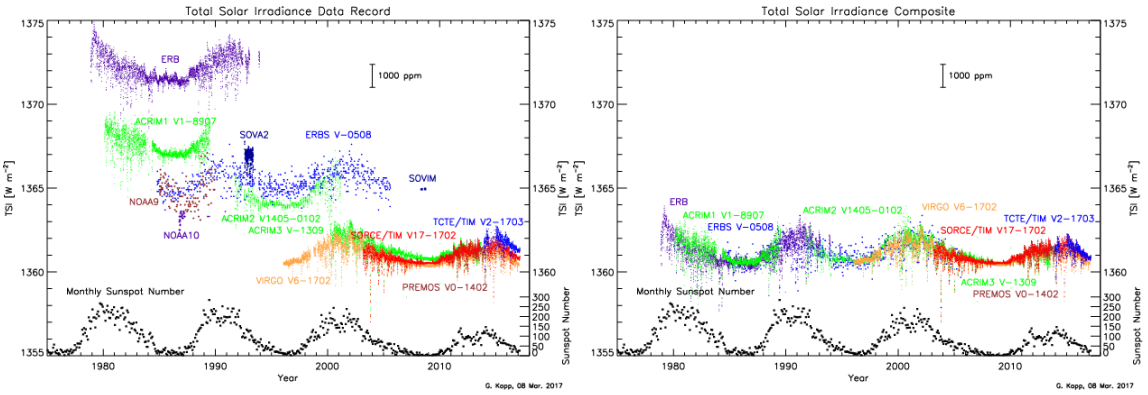

Figure 2: The spaceborne TSI data record: The record has been continuous since 1978 (left plot). Offsets due to calibration differences are adjusted by overlap between successive instruments. The composite record (right plot) relies on measurement continuity and instrument stability.

The Glory mission contained a follow-on to the SORCE TIM instrument and was meant to bridge a potential gap in measured total solar irradiance between the aging SORCE instruments and the TSIS TIM measurements. However, Glory TIM didn't reach orbit due to a failure of the launch vehicle. Nonetheless, the Glory project funded the creation of the TSI Radiometer Facility (TRF) at LASP (see Section 2.4.1). The TRF is the only calibration facility in the world able to characterize TSI instruments at the desired accuracy (0.01% absolute accuracy) and power levels under flight-like vacuum conditions. Experiments performed at the TRF have confirmed that erroneous increases in TSI signal occur from uncorrected diffracted and scattered light. This essential knowledge allows for improved accuracy in the composite record of TSI shown in Figure 2 (right plot) through post-processing instrument stability and scattered light corrections. More information about the TRF is available at *Kopp et al*. [2007] and http://lasp.colorado.edu/home/scrc/facilities/engineering-division/facilities/tsi-radiometer-facility/ (url last accessed 03/27/2013).

The SORCE TIM instrument has also contributed to knowledge of how sudden solar changes affect Earth's atmosphere. The largest decrease in total solar irradiance (0.34%) to date was measured in October 2003 during a period of extraordinary solar storms. The decrease was due to large, dark sunspots causing cooling in the photosphere. During the same group of storms, the TIM instrument also recorded the first definitive measurement of a TSI flare event – an increase of TSI by 270 ppm [*Woods et al*., 2004].

Short-term (less than a day) reductions in TSI due to the passage of planets in front of the Sun ("transits") have also been measured by high temporal cadence SORCE TIM observations. These observed reductions in TSI range from 0.005% to 0.1% for the transits of Mercury and Venus, respectively [*Kopp*, 2016].

2.2.2 SORCE Contributions to Observations of Spectral Solar Irradiance

The SORCE Spectral Irradiance Monitor (SIM) instrument measures solar spectral irradiance (SSI; units of W m^{-2} nm^{-1}) between 200 and 2400 nm. Between 400 and 2400 nm, the SORCE SIM provides the first ever satellite measurements of solar spectral irradiance. Earlier observations of solar spectral irradiance were concentrated on the

extreme ultraviolet and ultraviolet wavelengths because of their importance to heating of Earth's upper atmosphere and to ozone photochemistry in the middle atmosphere.

The SORCE SIM measurements have shown that the modulation of solar irradiance by the presence of magnetic structures on the surface of the Sun, such as sunspots, faculae, and plage, provide distinct contributions to SSI at different wavelengths (Figure 3). The variability at ultraviolet wavelengths is very different in character from TSI. The variability in SSI at visible wavelengths is similar to the variability in TSI, especially with darkening due to the passage of sunspots across the Sun [*Rottman*, 2006].

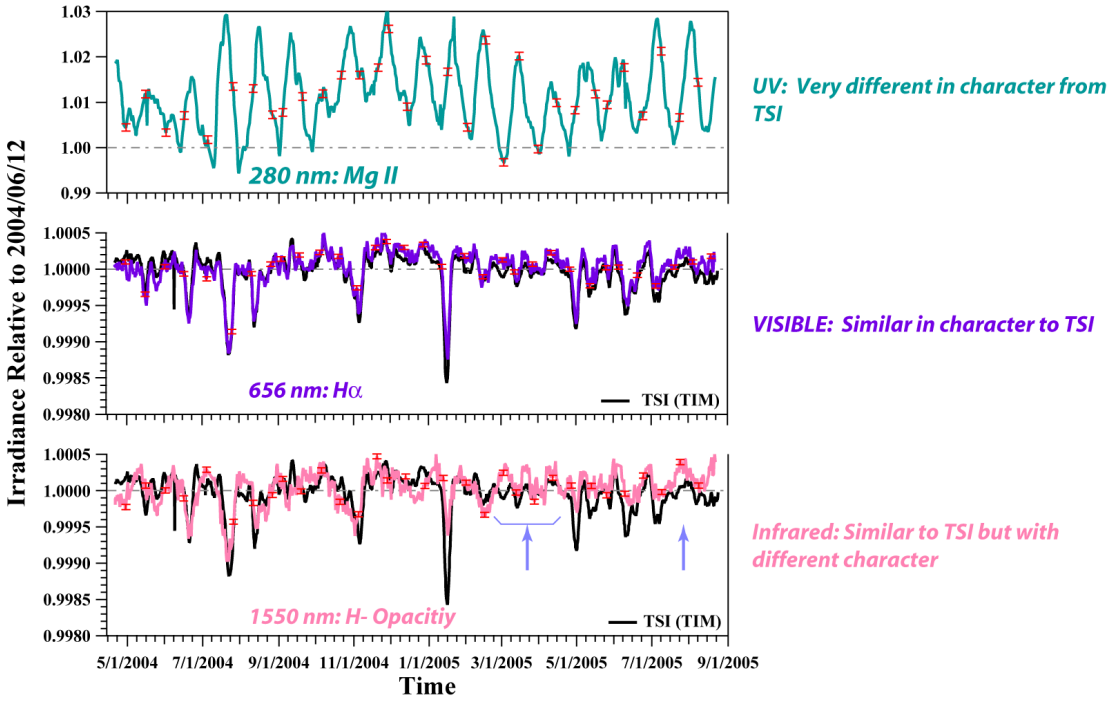

Figure 3: Solar spectral irradiance variability as a function of wavelength: Sunpots, faculae, plage, and the active network provide distinct contributions to SSI at different wavelengths (280 nm, 656 nm, and 1550 nm). Red error bars denote 1-sigma standard deviations.

Some 95% of the Sun's radiation occurs in the visible and near infrared [*Rottman et al.,* 2006; Figure 1]. Since TSI varies at the 0.1% level (Section 2.2.1), it is expected that the visible and near-infrared wavelengths vary comparably (or less) than this as confirmed by SIM measurements (over the 27-day solar rotational cycle) and shown in Figure 3 [*Harder et al*., 2005]. The fact that variability in ultraviolet wavelengths exceeds 0.1% is compatible since energies at these wavelengths comprise only a small fraction of the total.

Figure 4 shows the SIM observations of SSI short term rotational variability (grey curve) as compared to modeled SSI variability by the NRL Solar Spectral Irradiance (NRLSSI) model (red curve), which uses as inputs prior observations of ultraviolet radiation and the rotational modulation of plage and sunspot contrast [*Lean et al.,* 2000]. The fractional difference comparisons (left hand panel) are made over a 2-week period in 2005 where the TSI measured by the SORCE TIM instrument experienced a reduction by 0.15% (lower right plot) due to variability in the Sun's magnetic phenomena. Over 2-week time scales, degradation of instrument optics due to harsh radiation in space is not expected to contribute to the differences between SORCE SIM and modeled spectra seen. These differences include an approximately doubling of variability measured by SIM compared to the NRLSSI model at wavelengths between approximately 240 and 260 nm. At the Magnesium II line near 280 nm, the measured and modeled variability compare very well. The noisy signal measured by SORCE SIM between 310 and 360 nm is due to a bit resolution deficiency in the SORCE instrument that is apparent in the low detected signals at these wavelengths. TSIS SIM will not

experience a bit resolution deficiency because it has been designed to observe a much greater dynamic range in solar variability through the use of a 21-bit analog-to-digital (ADC) converter compared to the SORCE SIM 15-bit ADC converter (Section 3.2.11.1). Lastly, the bump in SIM measured signal around 800 nm followed by a gap in signal around 950 nm is related to the small and highly wavelength and temperature dependent radiant sensitivities of the visible (Silicon) and infrared (InGaAs) photodiode detectors in this wavelength range. TSIS SIM will make special dedicated, daily electrical substitution radiometer (ESR) measurements between 800-1000 nm to reduce measurement uncertainties and monitor for changes in radiant sensitivity over time and over variations in operating temperature.

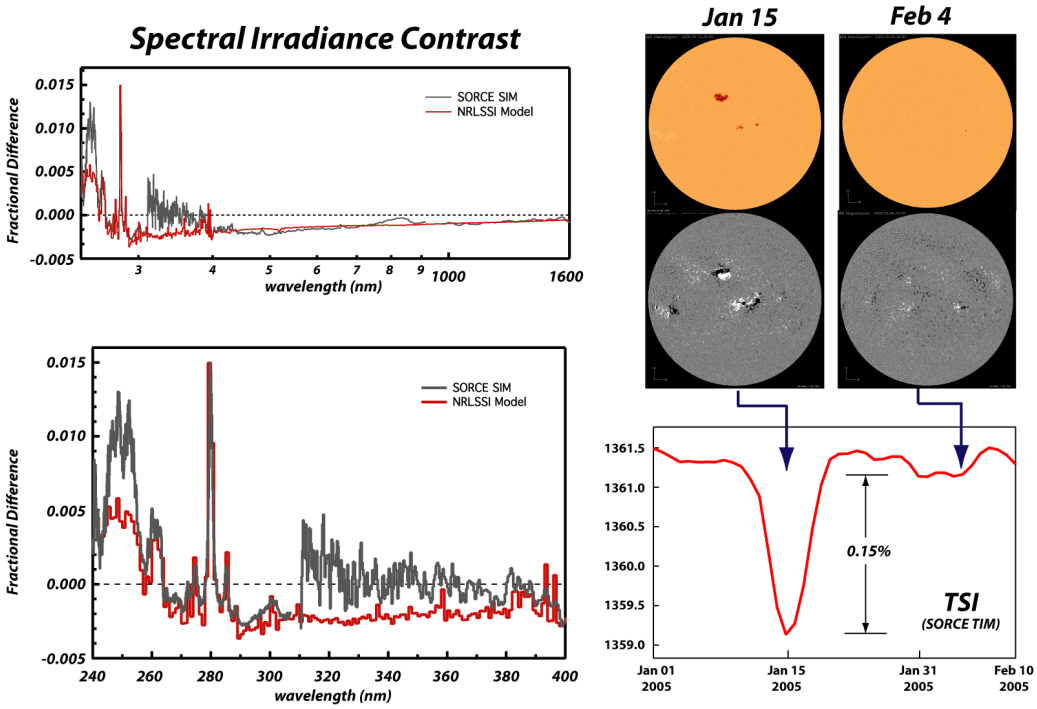

Figure 4: Short term rotational SSI variability: As measured by SIM (gray) and modeled (red) over a 2-week period (01/15/2005 – 02/04/2005). The NRLSSI modeled spectral variability [*Lean et al*., 2000] is based on observations of ultraviolet radiation (120-250 nm) and a model of rotational variability in plage (brightening) and sunspot (darkening) contrast. The comparisons are made during a time where measured TSI experienced a 0.15% reduction due to the magnetic phenomena on the surface of the Sun (right panel), shown as features of solar activity in white light (colored images) and in magnetograms (grey images) at corresponding times.

Comparisons of SORCE SIM measured variability to modeled SSI variability have also been made on 11-year solar cycle time scales. Figure 5 illustrates the difference in spectral irradiance near solar minimum in 2007 to a date in 2004 that occurred in the declining phase after solar maximum for SIM measurements (blue) and as modeled by the NRLSSI model [*Lean et al*., 2000]. The SORCE SIM results suggest that the spectral solar irradiance has greater long-term variability and does not vary in-phase with the total solar irradiance at all wavelengths. These differences depart from modeled expectations. *Harder et al.* [2009] postulate the differing trends in SSI are dependent upon the brightness temperature of the Sun, and therefore different parts of the solar atmosphere.

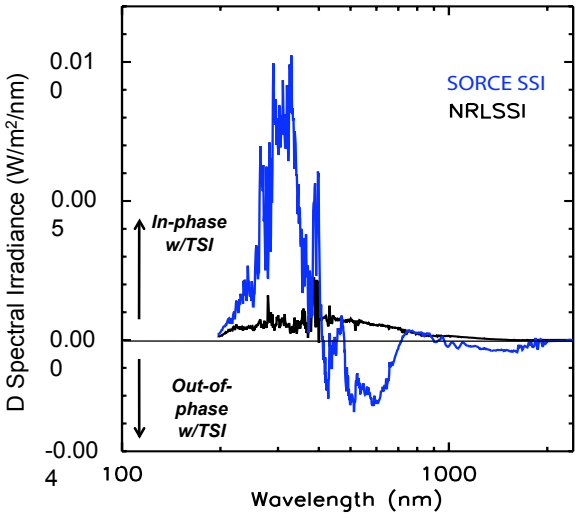

Figure 5: Spectral differences in observed long-term SSI variability: SSI between between 2004 and 2007 by the SORCE SIM instrument (blue) as compared to simulated spectral variability by the NRLSSI model (black [*Lean et al*., 2000]).

The implications of an "out-of-phase" (with TSI) response at ultraviolet (UV) wavelengths are large for middle atmospheric ozone production, as well as solar impacts on climate studies, in general. A study by *Merkel et al*. [2011] shows a model-predicted ozone response dependent upon an out-of-phase variability in the UV is more comparable to observations of ozone in the middle atmosphere made by the Sounding of the Atmosphere using Broadband Emission Radiometry (SABER) instrument. However, the long-term trends where irradiance at visible and near infrared wavelengths increases while the TSI decreases (years 2004-2008) while at the same time the UV irradiance decreased 3-10 times more than expected (from prior observations and model calculations) are unlikely of solar origin [*Lean and Deland*, 2012]. *Lean and Deland* [2012] suggests such variability is a result of unaccounted for drifts in instrument sensitivity. Current analysis is focused on the long-term degradation of the SORCE SIM instrument to separate instrumental from solar effects.

The TSIS SIM instrument will have a number of improvements in long-term stability, measurement precision, and pre-launch calibration over SORCE SIM. These improvements are critically important for climate research and are outlined in Section 2.4.3 and in greater detail in Section 3.2 as well as documents listed in Table 1. The improvements are possible due to the development of the Spectral Radiometer Facility (SRF-SIRCUS, see Section 2.4.2), which ties the radiometric response of the TSIS SIM at the unit and instrument level to a NIST SI-traceable standard. The levels of absolute radiometric accuracy uncertainty achieved reach 0.2% across the measured spectral range. Like the TRF facility (Section 2.4.1) the calibrations are performed at power levels typical of solar irradiance values and under flight-like vacuum conditions. More information about the SRF can be found at http://lasp.colorado.edu/home/scrc/facilities/engineering-division/facilities/spectral-radiometer-facility/ (last accessed 03/27/2017).

2.3 Science and Mission Goals and Objectives

The overall goal of TSIS is the accurate measurement of total and spectral solar irradiance for better understanding of solar forcing variations and their impacts on the Earth climate system. The TSIS observations are the follow on to the LASP-built instruments of the Solar Radiation and Climate Experiment (SORCE) and the TSI Calibration Transfer Experiment (TCTE) continuing the observations of total and spectral irradiance from 2003 through present day, albeit

with higher accuracy, increased precision, and improved stability. The improvements in accuracy, precision, and stability (i.e. the measurement requirements) are driven by the need to:

- improve our understanding of Earth's climate response to solar variability,
- for separating natural from anthropogenic climate forcing effects, and
- for the proper monitoring and interpretation of the variability in spectrally dependent radiative processes induced by changes in Earth's surface and atmosphere.

Observing small signals of long-term global climate change places very specific requirements on satellite observing systems. For solar irradiance, variations of less than 0.1% per decade are typical of the kinds of signals that must be extracted from "noisy" time-series measurements. To measure such signals, improved satellite instrumentation calibration is required along with inter-comparison to measurements made by similar instruments. Both high absolute accuracy and high relative stability are necessary for measuring a climate variable. The high absolute accuracy is vital for understanding the climate processes and changes. The high relative stability is necessary for determining long-term changes or trends. For flight (satellite) instruments, in general, accuracy is more difficult to achieve than stability.

Three approaches can be used for establishing the response of a flight instrument relative to SI units. One approach involves transferring a calibration from a "known" standard, a second approach makes a measure of the flight instrument response against an "irradiance standard", and a third approach characterizes the flight instrument as an "absolute sensor". This final approach has been adopted for TSIS and it involves characterizing each term in the measurement equation and tabulating a list of individual uncertainties and root sum square errors for overall measurement uncertainty.

The TSIS Total Irradiance Monitor (TIM) instrument is expected to be about three times more accurate than the SORCE TIM due to engineering advances in the optical and electrical sensors and to the end-to-end validation of the radiometer at the TSI Radiometer Facility (TRF) at LASP. The improvement in accuracy will allow the TSIS TIM to determine definitively if changes in total solar irradiance (TSI) are of solar origin or instrument artifacts. The original uncertainty and stability of the SORCE TIM instrument were 350 ppm and 10 ppm per year, respectively, and these specifications were met for much of the SORCE mission. However, beginning in November 2012, SORCE TIM time-dependent uncertainties have increased and on-orbit stability has decreased due to instrument aging and changes in spacecraft operation such as instrument power cycling which acts to conserve spacecraft batteries during orbital eclipse periods but increases thermal variations in the instrument. Current SORCE TIM uncertainties are 446 ppm (http://spot.colorado.edu/~koppg/TSI/). Instrument stability levels may no longer be achieving 10 ppm per year [*Kopp*, 2014].

Lessons learned from the first-ever measurements of spectral solar irradiance at wavelengths spanning the visible to the near-infrared (400-2400 nm) made by the SORCE Spectral Irradiance Monitor (SIM) have been incorporated by TSIS SIM to meet the measurement requirements. The specific TSIS SIM capabilities over SORCE SIM include reduced uncertainties in the prism degradation correction to meet long-term stability requirements, improved noise characteristics of the electrical substitution radiometer (ESR) and photodiode detectors to meet the measurement precision requirement, and improved absolute accuracy through pre-launch calibration using the novel Spectral Radiometer Facility (SRF).

The Science Objective of TSIS

1. Measure 4x daily total solar irradiance (TSI) with an absolute accuracy of 100 ppm and a relative accuracy of 10 ppm and to provide calibrated overlap with SORCE TIM, TCTE, and with future missions.
2. Measure 2x daily spectral solar irradiance (SSI) at variable resolution from 200-2400 nm with an absolute accuracy of 0.2% (2000 ppm), a relative accuracy of 0.01% (100 ppm), and with long-term relative stability of 0.05% per year (for wavelengths shortward of 400 nm) and 0.01% per year for wavelengths longward of 400 nm.

3. Validate and understand the reasons for the observed irradiance data in terms of solar variability, and assess how the variable irradiance affects our atmosphere and climate. Use this knowledge to improve estimates of past and future solar behavior and climate response.

The Mission Goals of TSIS

1. Successfully operate and obtain data from the TSIS spacecraft for 5 years (threshold mission duration is 3 years), and process and analyze all engineering data to ensure the health and safety of the spacecraft instruments.
2. Within 24 hours of Level 2 data availability, process all science data with the associated instrument and spacecraft engineering data to derive the Level 3 science data products. Calibrate the data for all TSIS instruments, converting instrument signals to standard geophysical units (W/m^2 or $W/m^2/nm$).
3. Clearly outline the operation of the TSIS instruments, analyze the data, and provide corrections to data as appropriate for changing instrument performance. Provide timely, validated data to the scientific community. Collaborate with users, and modelers of solar irradiance to ensure appropriate and conscientious use of the data, with special emphasis on conveying information on data quality and uncertainty. Conduct data processing in an open and transparent environment.
4. The Level 3 data are daily and four 6-hourly averages for TSI and twice-daily spectra for SSI representing the appropriately weighted mean of the Level 2 orbit-by-orbit measurements. The higher time resolution data are available to meeting secondary science objectives, for example, studying the passage of faculae and sunspots across the solar disk. The Level 3 SIM data is interpolated to a pre-defined wavelength grid at full spectral resolution.
5. Validate the TSIS data against other available simultaneous observations, against previous observations, and against the best-known models of solar radiation.
6. Through the development and operation phase of TSIS, refine and improve our understanding of the instruments and data they return.

2.4 Heritage

The total and spectral (from 250 nm through 2400 nm) instruments on SORCE, the TIM and SIM, are the trailblazers for the solar radiation measurements made by TSIS and they had varying degrees of heritage and algorithm development. At SORCE launch in 2003, the electrical substitution radiometer, the absolute detector for both TIM and SIM instruments, employed large doses of new technology and most data algorithms and instrument operating modes were built, adjusted and refined post-launch. Lessons learned on SORCE and other LASP missions have benefited the design and planned operations of the TSIS instruments. In particular, the TSIS SIM instrument has also undergone rigorous pre-flight instrument calibration and characterizations (like the TIM instrument for the SORCE, Glory, TCTE and TSIS platforms) and the instrument operating modes and data processing routines have been established pre-launch.

The TSIS Total Irradiance Monitor (TIM) instrument is structurally very similar to the TIM instrument on the SORCE satellite. Due to engineering advances in the optical and electrical sensors and to the end-to-end validation of the radiometer at the TSI Radiometer Facility, the TSIS TIM instrument will be roughly 3x more accurate than SORCE TIM. The TSIS TIM instrument is nearly identical to the TIM instrument built for the Glory satellite. Due to a failure of a Taurus XL rocket, the Glory satellite failed to achieve orbit when it was launched March 4, 2011.

The Spectral Irradiance Monitor (SIM) instrument was a new design on the SORCE satellite. Prior to 2003, the only space measurements of solar spectral irradiance were for the spectral range below 400 nm [*Cebula et al*., 1994; *Rottman*, 1998; *Brueckner et al*., 1993]. SORCE SIM measurements have produced the first space-based measurements of solar spectral irradiance in the 400-2400 nm wavelength region. The TSIS SIM instrument has

several modifications from SORCE SIM to reduce uncertainties in prism degradation, improve the noise characteristics of the ESR and to perform NIST-traceable pre-launch calibration.

2.4.1 TSI Radiometry Facility (TRF)

The offsets between the different instrument measurement records contributing to the more than 38-year record of total solar irradiance generally exceed the stated instrument uncertainties (see Figure 2). In 2008, the LASP-built TSI Radiometer Facility (TRF), which was funded through the NASA Glory project, was completed to address comparisons in irradiance, rather than optical power, mode making it the only calibration facility in the world able to character total solar irradiance (TSI) instruments to 0.01% absolute accuracy at solar power levels and under flight-like vacuum conditions. Experiments performed at the TRF have confirmed that erroneous increases in TSI signal occur from uncorrected diffracted and scattered light [*Kopp et al., 2007*].

The TRF is designed to perform irradiance comparisons of TSI instruments to a reference cryogenic radiometer. Its absolute reference is a custom-built cryogenic radiometer built for solar-power levels with an instrument tank designed to accommodate TIM and other TSI instruments to perform all tests in vacuum. The vacuum system is in common with the beam path to reduce optical differences between the comparisons. In addition, the instrument aperture illumination is uniformly generated through beam scanning techniques. As an end result, the TRF:

1. Improves the calibration accuracy of future TSI instruments,
2. Establishes a new ground-based radiometer irradiance reference standard, and
3. Provides a means of comparing existing ground-based TSI instruments against this standard under flight-like operating conditions.

A number of TSI instruments have been characterized at the TRF facility. They include the ground-based witness unit to the TIM that is currently flying on SORCE, the Glory TIM, the TCTE TIM, the PREcision Monitoring Sensor (PREMOS) from the Physikalisch-Meteorologisches Observatorium (PMOD) institute, a ground-based PMO-6 instrument similar to that flying on the Solar and Heliophysics Observatory (SOHO), the Digital Absolute Radiometer (DARA) of PMOD, the Compact Lightweight Absolute Radiometer (CLARA) of PMOD, engineering models of the Active Cavity Radiometer Irradiance Monitor (ACRIM1, ACRIM2, and ACRIM3), the SOVAR from the Royal Meteorological Institute of Belgium (RMIB), and the TSIS TIM instrument.

All TSI instruments except the TIM put their primary precision aperture close to the radiometer cavity, which results in an overfilling of the view-limiting aperture allowing additional light into the instrument and an erroneous increase in measured signal due to uncorrected scatter and diffraction of light from the front and interior sections of the instruments. The required correction has reached 0.51% in some cases.

2.4.2 Spectral Radiometry Facility (SRF)

The Spectral Radiometer Facility (SRF), a LASP facility, is a comprehensive calibration facility providing irradiance calibration of the TSIS SIM ESR and photodiodes and the full SIM over the operation wavelength range of the SIM instrument. The main components are a STOVE thermal vacuum tank, a manipulator for the SIM and ESR subassembly, a vacuum housing for the steering mirror, a NIST cryogenic radiometer, and the NIST Spectral Irradiance and Radiance responsivity Calibrations using Uniform Sources (SIRCUS) lasers. The facility was completed in 2012. Levels of absolute radiometric accuracy uncertainty achieved reach 0.2% across the designed measurement spectrum (210-2400 nm).

The LASP Spectral Radiometer Facility:

1. Performs spectral irradiance calibrations at power levels typical of solar irradiance values and under flight-like vacuum conditions over 210-2400 nm (extendable to > 3000 nm),
2. Allows for quantitative measurements of the spectral response functions,

3. Provides an absolute calibration tied directly to a NIST L-1 Cryogenic radiometer, which in turn is traceable to the NIST Primary Optical Watt Radiometer (POWR),
4. Allows for calibrations of channel to channel boresight alignments, and
5. Allows for calibrations of pointing and FOV mapping effects on the measured signal.

2.4.3 Overview of Design Changes for TSIS SIM

The TSIS SIM is designed for long-term spectral irradiance measurements used for understanding solar variability and its impact on Earth climate. Lessons learned from SORCE SIM and other LASP programs were incorporated into TSIS SIM to meet the measurement requirements set by the variability in solar spectral irradiance. The changes in the measurement requirements needed for long-term stability, measurement precision, and pre-launch calibration required specific capabilities over SORCE SIM that are briefly summarized in this section. Further instrument details are provided in Section 3.2.

Ultimately, the TSIS SIM meets the measurement requirements including 0.2% absolute irradiance accuracy over full (200-2400 nm) spectrum, 0.01% relative measurement precision, and on-orbit capability to correct for long-term drifts and sensitivity changes of less than 0.05% per year. The SIM Design Document (ref. in Table 1) contains in-depth details of the design and heritage of the TSIS SIM instrument.

2.4.3.1 Meeting the Requirement for Long-Term Stability

An ultra-clean optical environment was created to mitigate contamination of the prism, the SIM's lone optical element, due to on-orbit condensation of outgassing organic compounds. To achieve this, the TSIS SIM implemented a modular design with the entrance slit and photodiode detectors isolated in one module, the ESR detector in a second module, and the CCD assembly in a third module. This modular approach necessitated a greater range in prism angle in order to completely scan all wavelengths over the photodiode detectors, while the ESR, being the absolute detector, is placed at the prime dispersive location on the optical plane.

With the greater range in prism angles, changes also needed to be implemented in the CCD encoder, so that green light entering the CCD channel did not image past the CCD encoder, thereby losing track of the wavelength registration. For TSIS SIM, a double spot CCD encoder has been implemented. Both spots are commandable, and measurements across the full wavelength scale are obtained. With the primary scan, measurements at wavelengths from 207 – 2400 nm are obtained with coverage from 200 - 618 nm obtained with the extended scan. Very precise wavelength control is achieved so that small, unknown wavelength shifts will not translate into irradiance changes that could be falsely interpreted as solar variability at the 0.01% level. In order to image two separate image spots from the same entrance slit, the single spherical mirror from SORCE was changed to a double spherical mirror design. A description of an image mask that serves as an aperture stop and makes the system effectively immune to pointing errors is available in the SIM Design Document (ref. in Table 1).

TSIS SIM has 3 channels (A, B, and C) instead of the 2 channels on SORCE SIM. The addition of the 3rd channel reduces uncertainties in long-term degradation tracking (Section 7.2).

2.4.3.2 Meeting the Requirement for Measurement Precision

Firstly, improvements in the ESR thermal design and a larger dynamic range in the analog-to-digital converter (ADC) (along with signal integration) have improved the noise characteristics of the TSIS SIM. An ADC is used to convert the measured voltage into a discrete digital time representation, commonly called a data number, or DN. SORCE SIM had an effective 15-bit bipolar ADC covering -10 to +10 V, resulting in approximately 305 μV/DN resolution. At this resolution, SORCE SIM measurements between approximately 310 nm and 380 nm were "bit-noise" limited (Figure 4), meaning the small signals (40 and 300 mV) at these wavelengths were limited by the ADC resolution.

Instead, a dual slope ADC (Section 3.2.11.1) is utilized for the TSIS SIM. With the 2*10^6 Hz sampling of TSIS SIM (approximately a 21 bit ADC converter) over a range of 0 to 10 V, the improved resolution is now approximately 4 μV/DN. These improvements to the TSIS SIM do achieve greater measurement precision, but at the cost of a longer measurement cadence (SORCE SIM had a 1-second measurement cadence, while TSIS SIM will require 2-seconds per measurement).

Secondly, improvements to the thermal design were made to lessen sensitivity to wavelength encoding shifts that occur on SORCE SIM after a 'cold-soak' when the spacecraft experiences a safe-hold event and resulting loss of power to the instruments and survival heaters. The wavelength encoding shifts have been attributed to a change in the fixed angle of the CCD mirror relative to the prism incidence angle and are compounded by the fact that two separate CCD systems are utilized on each channel for SORCE, which must be independently recalibrated after each safe-hold event. Therefore, for TSIS SIM, all three channels utilize the same common CCD encoder mirror and a single all-aluminum mirror and mirror mount assembly has been developed.

Thirdly, the vertical dimension of the entrance slit has been reduced for TSIS SIM from 7 mm to 6.5 mm. This entails a lengthening of the entrance slit in the cross-dispersion direction and was made to allow more margin and less opportunity for photon loss between light entering the size of the entrance and passing back through the exit slits behind which the detectors reside.

Fourthly, the CCD mirror is now diamond turned out of aluminum making it more tolerant to cold temperatures encountered in the survival mode of the instruments/spacecraft. With this thermal mirror mounting assembly, there is less than a 15-arcsecond shift over the survival range in temperatures. In addition, a diffuser made of fused silica coupled with a green bandpass filter has been placed in front of the CCD entrance to diffuse light across the whole CCD mirror. By use of a mask on front of the CCD mirror, the TSIS SIM is ensured to have a consistent illumination spot on the CCD mirror with spacecraft movement. The end result is a zero subpixel CCD shift (SORCE SIM experienced a CCD shift of up to 106 subpixels), therefore zero servo-changes in prism angle.

Finally, TSIS SIM's prism drive differs from SORCE SIM. SORCE SIM had a suspended voice coil system to rotate the flexure controlling the angular rotation of the prism drive with very fine motion control and low actuation noise. Because of the larger range of prism angles required by TSIS SIM, a TPS drive motor is used, which is combined with a tachometer to reduce jitter motor when the prism angle reaches a commanded position. The TPS drive motor has bearings (unlike SORCE SIM's trefoil flexures), which are exercised regularly to prevent warping of the bearings (Section 3.2.12.4).

2.4.3.3 Pre-launch Calibrations: Providing Absolute Accuracy

TSIS SIM utilizes the same fused silica (Suprasil 3001) as SORCE SIM, however improvements in the glass manufacturing mean the index of refraction is now calibrated to 10 ppm.

Primary improvements in absolute accuracy come from the extensive pre-launch calibration and characterization undertaken for TSIS SIM. Throughout the instrument build, calibration and characterization have followed a measurement equation approach at the unit-level for full validation of end-to-end performance at the instrument-level. SI-traceable pre-launch calibrations to better than 0.2% level are performed at the NIST Spectral Irradiance and Radiance Responsivity Calibrations using Uniform Sources (SIRCUS) facility and traceable to the U.S. standard for optical power, the Primary Optical Watt Radiometer (POWR) (Section 2.4.2).

2.4.4 Data Processing Approach

The TSIS SIM instrument processing has changed from the approach used in SORCE SIM processing. New algorithms for TSIS SIM have evolved based on an instrument calibration approach, as discussed in Section 4.2.2 and Section 5. The processing for TSIS TIM is largely unchanged from the approach of SORCE and Glory TIM

instruments. An overview of the data processing architecture is given in Section 10. More detailed information is provided in the Project Data Management Plan (ref. in Table 1).

3 Instrument Design

3.1 TIM Instrument

The TSIS Total Irradiance Monitor (TIM) measures total solar irradiance (TSI) with the unprecedented precision of the SORCE TIM instrument and 3x better accuracy. The TIM, an electrical substitution, null-balance, solar radiometer, directly faces the Sun during the daylight portion of each orbit to measure irradiance (radiant flux density or incident radiant power per unit area with units W m^{-2}). The high accuracy and low noise measurements (100 ppm combined standard uncertainty with 10 ppm noise level) are achieved through good thermal design, use of phase sensitive detection analysis techniques, and improvements in electronics. Table 2 summarizes the TIM operational parameters.

Table 2: TIM Instrument Properties

Parameter	**Value**
Wavelength Range	Full Solar Spectrum
Absolute Accuracy	100 ppm (1 σ)
Relative Accuracy (drift)	10 ppm per year
Size (Instrument)	11.7 long x 11.4 wide x 6.5 high [in]
Size (electronics)	10.7 long x 8.9 wide x 2.8 high [in]
Mass	9.286 kg instrument, 4.203 kg electronics
Power	20.6 W
Design Lifetime	5 years
Field of View (FOV)	± 2° without vignetting, ± 6° cut-off
Pointing Requirement	± 10 arcmin with ± 100 ppm change
Precision Aperture Size	0.5 cm^2
Shutter Frequency	0.01 Hz
Typical Cone Reflectivity	100 ppm
ESR Temperature	30.8°C

The TIM's absolute detector is an electrical substitution radiometer (ESR). The ESRs are thermally balanced in pairs, one ESR acting as the thermal reference while the other is actively heated electrically to match the reference ESRs temperature. Instrument redundancy and degradation tracking via duty cycling are provided through 3 additional, identical ESRs. The instrument housing (Figure 6) provides thermal stability and acts as a heat sink for the ESRs, which have a well-characterized thermal conductive path to the housing. The design and operation of the TSIS TIM is largely unchanged from the SORCE TIM instrument, detailed in *Kopp and Lawrence* [2005] and *Kopp et al*., [2005a, 2005b].

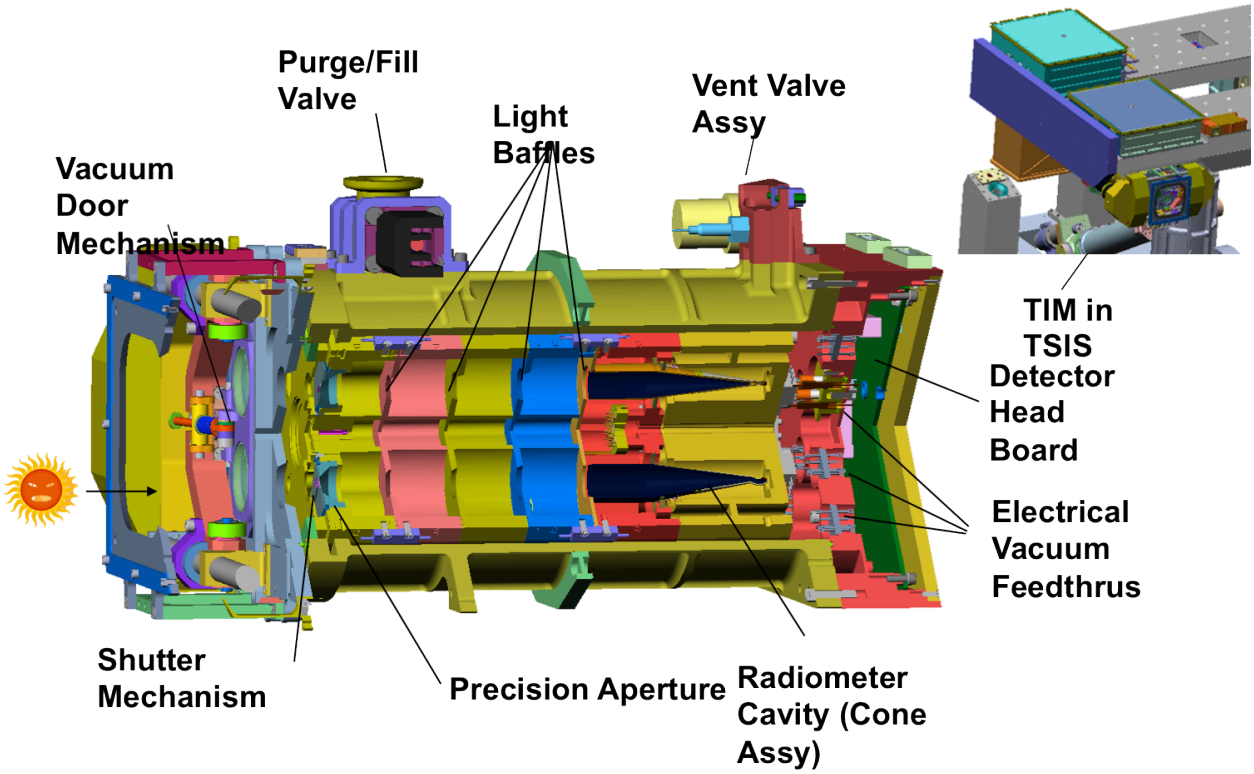

Figure 6: Cutaway of TIM instrument: Shown are two of the four ESRs. Light entering the instrument from the left through precision apertures is absorbed by the ESRs, causing temperature changes used to determine incident power.

A precision aperture, diamond turned to an edge radius < 1 μm determines the area of the solar flux accepted by the TIM. Baffles, located behind the precision aperture, shield the measurement cavity from Earth albedo and other off-axis radiation. Uncertainty in aperture area due to diffracted light is the largest contributor to the TIM's absolute accuracy budget (see Table 3). The apertures share a temperature sensor with 0.1°C absolute accuracy and 0.001°C resolution, so thermal variations in aperture size can be corrected to their ground-calibrated value.

Open/close shutters in front of the precision apertures regulate light input to the cones. Brushless torque motors drive the TIM shutters, one for each cone. The shutter temperature changes are monitored to 0.005°C. The optical labyrinth seals at the edges of the shutter are light tight to 1 ppm. When the shutter is open and the cavity illuminated with sunlight, reduced electrical heater power is needed to maintain the active ESRs temperature. This measured reduction in electrical heater power combined with calibrations of the cavity's absorptance provides a measure of the entering radiant solar power. The area of the precision aperture determines the area over which sunlight is collected and when combined with the incident radiant power yields TSI (W m^{-2}) in ground processing.

Sections 3.1.1-3.1.9 discuss design elements of the TIM instrument including the ESR absorptive cavities, the digital electronics needed to maintain a thermal balance between pairings of ESRs, the shutter which opens to allow incident sunlight to illuminate the ESR cavity, and the electrical heater which reduces power to the active ESR in order to maintain the balanced temperature in cases of incident sunlight. Also discussed is a summary of the TIM observation modes. Table 3 lists the sources of uncertainty for the TIM instrument uncertainty budget. The ground and flight characterizations and calibrations necessary to bring the sensitivity to the desired absolute accuracy are discussed in *Kopp et al*., [2005a] and Sections 5.1 and 5.2.

Table 3: TSIS/TIM instrument uncertainties listed by type and origin: Origin is defined by instrument level, component level, or analysis level. The total root sum square of uncertainties is 85.5 PPM (within 100 PPM measurement requirement). The right-most two columns are results specific to SORCE/TIM as flown [from *Kopp et al*., 2005a].

				SORCE AS FLOWN	
Correction	**Origin**	**Size [PPM]**	**1σ [PPM]**	**Size [PPM]**	**1σ [PPM]**
Distance to Sun, Earth, & S/C	Analysis	33,537	0.1	33,537	0.1
Doppler Velocity	Analysis	57	0.7	57	0.7
Shutter Waveform	Component	100	1.0	100	1.0
Aperture	Component	1,000,000	28	1,000,000	55
- Diffraction	Component	452	46	100	25
Cone Reflectance	Component	182	35	200	54
Non-Equivalence, Z_H/Z_R-1	Instrument	782	43	7	22
Servo Gain	Instrument	2,115	0.0	16,000	0.0
Standard Volt + DAC	Component	1,000,000	15	1,000,000	7
- Pulse Width Linearity	Component	800	3	1000	~186
Standard Ohm + Leads	Component	1,000,000	25	1,000,000	17
Dark Signal	Instrument	1,645	14	2700	10
Pointing	Analysis	100	10	100	~ <50 (see ref.)
Measurement Repeatability (Noise)	Instrument	-	4	-	1.5
Uncertainty due to Sampling	Analysis	-	12	-	-
Total RSS			85.5		~205

3.1.1 Electrical Substitution Radiometer

The TIM ESRs are thermally conductive cavities with high absorptivity across the entire solar spectrum. The high absorptivity ensures nearly all the entering sunlight is collected and converted into thermal energy within the cavity. This thermal energy is quickly transported to thermistors that monitor cavity temperature, so that the servo system maintaining the cavity temperature can respond quickly to changes. Electrical power is applied to the highly absorptive ESR cone to maintain a constant temperature. Periodically a shutter opens over a precision aperture allowing sunlight to fall incident on the inside of a cone. A measured reduction in electrical power now compensates for the increase in absorbed radiant energy. Conversely, when the shutter is closed again and no light is being absorbed by the ESR, the electrical power must once again be supplied to maintain the same ESR temperature. This changing electrical power is "equivalent" to the changing incident radiant power, and thereby provides an accurate measure of the irradiance.

The ESR cones are made from 1 mm thick electro-deposited pure (to 99.99%) silver with high thermal diffusivity. The high absorptivity is due to the diffuse black surfaces in the cone interiors and heat sink, created by an etching of nickel phosphorus (NiP) metal (Figure 8), and not a black specular paint used on other cavity detectors such as ACRIM, for example. The average absorption of the cone is denoted by α. The average cavity reflectances $(1-\alpha)$ are 0.0002 over the solar wavelengths. For determining solar variability, the crucial criteria for the sensor black are knowledge and stability of α rather than absolute blackness.

The four ESRs are separated by internal walls, so the light paths between the precision apertures and corresponding cavities are isolated and independent. Black baffles surrounding each ESR block off-axis glint from the Earth or external spacecraft and instrument components. Changes in cavity reflectance to better than 0.2 ppm sensitivity are monitored on-orbit using silicon photodiodes mounted in the baffle nearest each cavity and pointing into the cavity.

The dominant path to the TIM's heat sink are stainless steel spoked mounts and they are temperature-maintained to a high level of accuracy by high-resolution thermistors used as sensors for an electrical bridge circuit. The silver electrode spinel chip thermistors are soldered to each cone near its support structure and sense relative changes (i.e. the thermistors require high resolution but not high absolute accuracy) from a nominal temperature in order to control the feedback loop for electrical substitution heater power. The thermistors have a –4%/°C Temperature Coefficient of Resistance (TCR). Temperature fluctuations of the heat sink during open and close shutter phases are less than 10^{-6} K and cavity thermal relaxation times through these mounts are approximately 220 seconds. All four ESR cones are cantilevered from a central hub, ensuring that the active and reference cones have the same temperature source (Figure 7). This design provides a large thermal mass with a ~400-second time constant, giving a low-conductivity path for heat dissipation from the cone. Gold coupling on the exterior surfaces of the cavities reduces radiative coupling between the cavities and their surroundings, insure a stable and finite settling time, and to avoid contamination. The temperature control (heaters and thermistors) and the cone mounting are centered to prevent generation of thermal gradients. Empirical model calculations include the time dependence of the temperature changes due to the mounting and due to the incoming solar radiation and estimate the effective instrument thermal background (dark) signal.

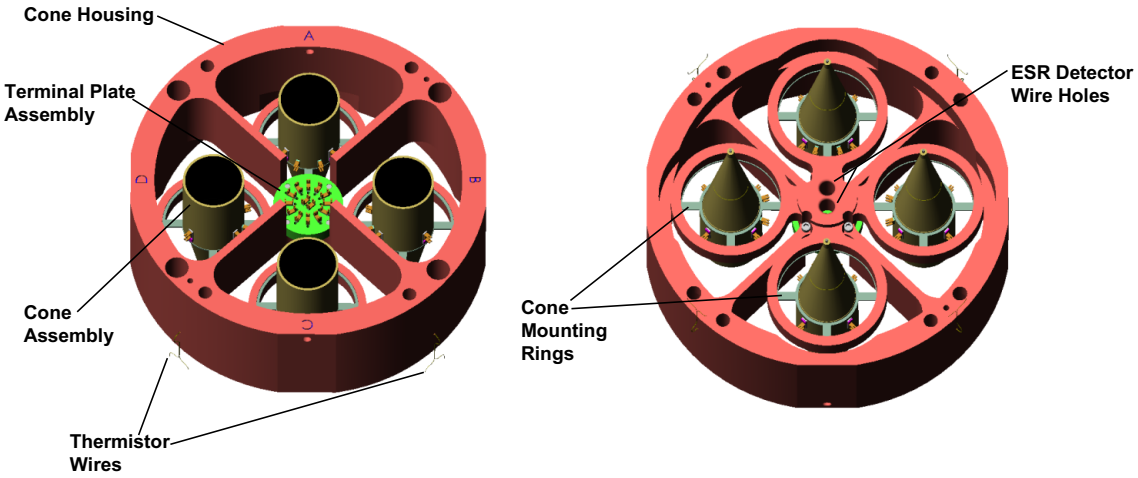

Figure 7: TIM internal cavity mounting. TIM's cavities are cantilevered from a common hub on low-conductivity mounting rings to reduce thermal noise.

During operation, electrical power is applied to the highly-absorptive active ESR cone to maintain a constant temperature. Periodically, a shutter opens over a precision aperture and allows incident sunlight on the inside of the cone. The bridge circuit becomes unbalanced and a measured reduction in electrical power to the cone compensates for the increase in absorbed radiant energy, bringing the circuit back into balance. When the shutter is then closed and the ESR is not absorbing incident sunlight, electrical power must once again be supplied to maintain the nominal ESR temperature. This electrical power is supplied by a wire-wound precision resistor near the tip of each cone. The change in electrical power that gives precisely the same cone temperature as that provided by the incident light is a measure of radiant power incident on the ESR cone.

In the construction of the heater, an attempt is made to match the distribution of heater power and absorbed radiant power. If the electrical power were applied with the same distribution as the absorbed radiation, the electrical and radiant power would be exactly equivalent. The relationship between the distribution of electrical heater power and absorbed radiant power, referred to as the equivalence ratio (see Section 3.1.7), is not unity largely because of delay differences in conducting heat from the rear of the cone to the central thermistors. The non-equivalence effects are reduced by making the walls of the cones thicker, by matching the heater distribution to the radiation distribution (as with the wire-wound resistor), and by increasing the thermal diffusivity of the cone (thus our selection of silver). The differential delays can be characterized by measurements versus shutter frequency. The long-term stability of the replacement equivalence depends on the finesse of the thermal interfaces; so all thermal joints are solid or soldered.

3.1.1.1 NiP Black

The specular paint cavity design has been rejected for TIM because it is unstable and too sensitive to dust. Instead, diffuse NiP black, also called NIP, Ball, and NBS black, is used for the absorptive surfaces of the ESRs. Nickel phosphorous is an ultra-black coating that has a very high radiation absorption capacity due to its morphological structure. This material is described in the U.S. patent by *C. E. Johnson* [1980].

Ni-P black is created by plating surfaces with Nickel Phosphorus (NiP) and etching to produce a metallic, highly conductive, optically stable, absorptive surface as shown in Figure 8. Because this surface is metallic, it is extremely robust to vibration and radiation. Unlike absorptive paints, Ni-P black contains no organic molecules, which are prone to photolysis over time with exposure to solar UV.

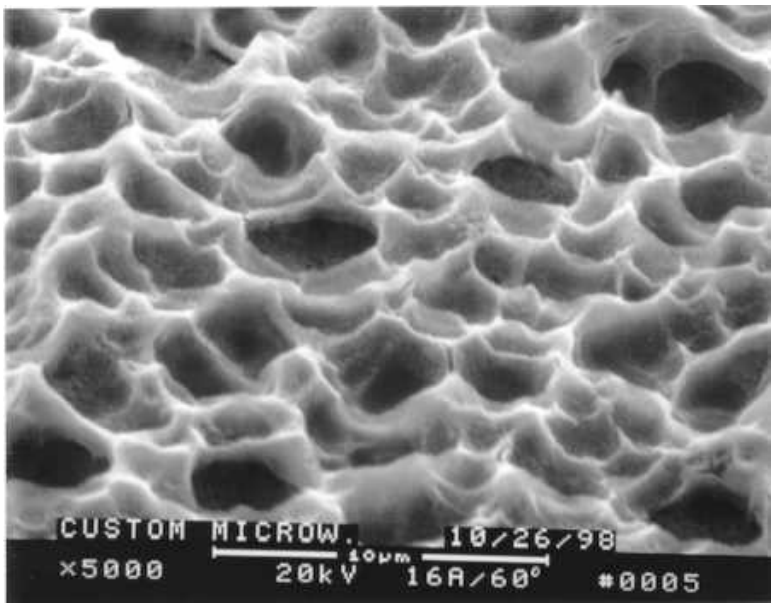

Figure 8: A scanning electron microscope image of a sample of Ni-P black surface: Shown is the rough surface that gives the material its highly absorptive properties. The cavity indentations are nearly as deep as they are wide, providing "light traps" for incident photons.

3.1.2 Standard Resistance

A resistive heater for each ESR cavity is provided by a wound, double strand of polymide-insulated wire. This wire has an accurately known thermal coefficient of resistance, high stability over time, and small, known hysteresis [*Kopp and Lawrence*, 2005]. Applying a known voltage V across the heater leads heats the cavity with the power V^2/R, where each wire's resistance R is approximately 540 Ω. The copper leads to the heater wire are individually calibrated on the ground and are monitored by four different instrument thermistors, which enable on-orbit temperature corrections to the resistance. Total uncertainty in the heater lead resistance is less than 10 ppm. The calibration and characterization of the stable resistance references are discussed in *Kopp et al*., [2005a] and Sections 5.1.3.

3.1.3 Standard Volt

Two Linear Technology LTZ1000 voltage standards (diodes) provide the reference 7.1 V voltages for each ESR pair and have low thermal sensitivity and low drift. The long-term stability [*Spreadbury*, 1991] is better than 3×10^{-6} per year and the radiation stability [Rax, Lee, and Johnston, 1997] of the diodes is documented. A MOSFET switch digitally modulates the voltage applied to the ESR heaters [*Kopp and Lawrence*, 2005]. Therefore, the electrical heater power applied to an ESR from a reference voltage V is thus qV^2/R, where q is the digital signal processor controlled modulation duty cycle and can be varied between 0 and nearly unity. The calibration and characterization of the stable voltage references are discussed in *Kopp et al*., [2005a] and Sections 5.1.3 and 5.2.5.

3.1.4 Precision Apertures

The precision aperture to each cavity is diamond turned and approximately 0.8 cm diameter, allowing around 68mW of sunlight to enter each cavity [*Kopp and Lawrence*, 2005]. The knife-edge aperture is flat and highly reflective with the bevel facing the instrument interior to prevent scattered light into the instrument. Off-axis stray light is reduced using black baffles. The characterization and calibration of the aperture for diffraction and thermal gradients is discussed in *Kopp and Lawrence* [2005], *Kopp et al.* [2005a] and Sections 5.1.2 and 5.2.2.

3.1.5 Shutters

Each ESR has an independent shutter that opens or closes in approximately 10 ms. The shutter open and close times are characterized and accounted for in the post-processing phase sensitive analysis (*Kopp and Lawrence*, 2005, *Kopp et al*., 2005a, and Section 4.3). The interior of each shutter is gold-plated to reduce thermal emission into the instrument's interior and this thermal emission is monitored by an embedded thermistor. The lifetime of the primary cavity's shutter exceeds the TSIS 5-year mission lifetime by a factor of 2.

The transmission is unity when the shutter is open and < 3 ppm when the shutter is closed.

TSIS TIM shutters are an identical design to those on SORCE.

3.1.6 Digital Control Electronics

A 16 MHz Analog Devices digital signal processor (DSP) performs all major instrument functions [*Kopp and Lawrence*, 2005]:

i. maintains thermal balance for the ESRs (Figure 29) and regulates instrument temperature by operating three 100 Hz AC servo bridges and applying pulse-width modulated power to each cavity at 100 Hz via a field programmable gate array,
ii. maintains shutter timing and,
iii. interfaces commands and telemetry with the spacecraft microprocessor.

The total solar irradiance can be predicted to better than 1% during any given week (Sections 2.1 and 2.2). Therefore, the jump in electrical heater replacement power applied by the DSP at each shutter transition can be anticipated in a process called feedforward. The feedforward process allows the servo system to operate at high gain while reducing measurement uncertainty due to loop gain fluctuations. It also prevents servo saturations during shutter transitions and reduces the overshoot that would occur if the servo system only reacted to measured changes. The calibration and characterization of the measurement uncertainty due to loop gain fluctuations are discussed in *Kopp and Lawrence* [2005], *Kopp et al*., [2005a], and Section 5.2.4.

3.1.7 Equivalence Ratio

The change in electrical power (Z_H) that gives precisely the same cone temperature as that provided by the incident sunlight is a measure of absorbed radiant power (Z_R) incident on the ESR cone (Section 3.1.1). The equivalence ratio is defined as the ratio of the two thermal impedances, Z_H / Z_R, which gives the same temperature as an ESR's thermistor. For an ideal ESR, the equivalence ratio would be unity. However, due to delays in thermal propagation of the input electrical and radiant power, this term can differ significantly from unity particularly at higher frequencies.

Due to good thermal design and the near co-location of heater and radiant power inputs at the tip of the cone end of the TIM ESR, this ratio is within a few ppm of unity for signals in-phase with the shutter [*Kopp and Lawrence*, 2005]. An advantage of the phase-sensitive detection method (Section 4.3) is that the equivalence ratio need only be known at the shutter frequency (100-s period), making the potentially large equivalence deviations at higher frequencies irrelevant. This reduces uncertainties in this term and makes the calculation of the equivalence easier. *Kopp and Lawrence* [2005] provides the details of the algorithm used to calculate the TIM's equivalence ratio. The calibration and characterization of the measurement uncertainty due to uncertainty in equivalence are discussed in *Kopp and Lawrence* [2005], *Kopp et al*., [2005a], and Sections 5.1.5.

3.1.8 Diagnostic Instrument Parameters

Various monitors on TIM provide additional corrections and diagnostic measurements.

A central heat sink maintains instrument temperature and stability during the shutter open and shut periods and during sunlit and eclipsed portions of the orbit. Silicon photodiodes are mounted near the front of the heat sink and face backward into the cone interiors (but out of the optical beam) to monitor cone reflection, hence changes in cone absorptivity, to better than 1 ppm accuracy. Various instrument temperatures are monitored by multiple thermistors located on the primary aperture plate, each shutter, and at three locations on the heat sink and are used in estimating the thermal background corrections.

The largest contribution to thermal noise are the temperature gradients caused by asymmetries in the physical mountings of the ESR cones that are monitored by thermistors on opposite sides of the cylindrical housing. The temperature changes of the mounting points of each pair of active and reference cones must be small at the shutter frequency, which is achieved by mounting the active and reference cones at the same point (Figure 7) using physical supports with low thermal mass and short length to keep the parasitic thermal time constants small. The main electronic noise is caused from thermal emission from the warm cone cavity. The shuttering process largely removes this noise and corrections depend on calibration measurements of "dark" (empty space) made during the nighttime portion of each orbit. The thermal noise, along with electronic noise, total less than 1 ppm uncertainty.

3.1.9 TIM Science Operation Modes

Having four identical ESR's in the same housing provides a two-fold advantage: it provides redundancy in case of failure of a unit, and it provides a means of diagnosing degradation by allowing duty cycling between the various channels. The TIM's observation modes are summarized in Table 4. Degradation monitoring is discussed in Section 7.1.

Nominally, one ESR operates continuously and views the Sun for the 'daytime' portion of every orbit while the others' shutters remain closed. This is the 'Normal' Mode where the primary ESR is shuttered at the 100-s period and a feedforward value appropriate for the expected solar irradiance level is used. On the remaining portion of each orbit when the Earth eclipses the Sun, the TIM makes measurements of dark space using the same configuration for sun viewing as above, albeit with a lower feedforward value. These dark measurements are used to correction thermal contributions from the (relatively) warm instrument (see Section 5.2.7).

A servo-gain mode is operated for 6-hours every two weeks. In this mode, the shutters remain closed and the response of each ESR to a square-wave electrical heater transition is measured. The ESR response can change due to non-equilibrium conditions, which the DSP minimizes by applying a feedforward signal that anticipates power changes as the shutter transitions between open and closed. This will be monitored throughout the mission.

Field of view (FOV) maps are performed every 6 months to determine instrument sensitivity to pointing offsets from the sun vector by ± 15°. The calibration is performed over a 5 x 5 grid with 5-arc minute spacing centered on the Sun and changes are monitored over time.

Table 4: TIM observation mode summary

Observation Mode	Frequency	Duration	Target	ESR	Comments
Normal	Every orbit, daylight side	400 s per meas., continuous	Sun	B	Primary data acquisition mode
Dark	Every orbit, eclipse	400 s per meas., continuous	Dark space	B	Characterize thermal background
Degradation A	1%	1 orbit/week	Sun and dark space	A, B	Frequent degradation
Degradation C	0.5%	1 orbit/2 weeks	Sun and dark space	A. C	Infrequent degradation
Degradation D	0.2%	1 orbit/4 weeks	Sun and dark space	B. D	Infrequent degradation
Gain	Bi-weekly	4 orbits	NA	All	Servo calibration
FOV map	Every 6 months	15 orbits	Sun, 5x5 raster, 5' steps	B	Determine relative sensitivity to FOV

3.2 SIM Instrument

The TSIS Spectral Irradiance Monitor (SIM) measures spectral solar irradiance (SSI) incident on a plane surface at the top of the atmosphere that is normal to the Sun two times per day from 200 to 2400 nm at variable (~1- 35 nm) spectral resolution. The integrated irradiance contribution measured by SIM (Figure 9) is approximately 97% of the total solar irradiance measured by the TIM instrument. The SIM is a follow-on to the SORCE SIM instrument with improvements in absolute accuracy (0.2% over the full spectrum), long-term stability (to better than 0.05% per year), and relative precision (0.01%) (see Section 2.4.3). These improvements are key requirements to understanding the contributions from varying spectral irradiance on climate. Long-term relative accuracy is maintained by duty cycling three independent spectrometers and directly measuring the prism transmission for each. Details on planned instrument operation and degradation correction are provided in Sections 3.2.12.3 and 7.2.

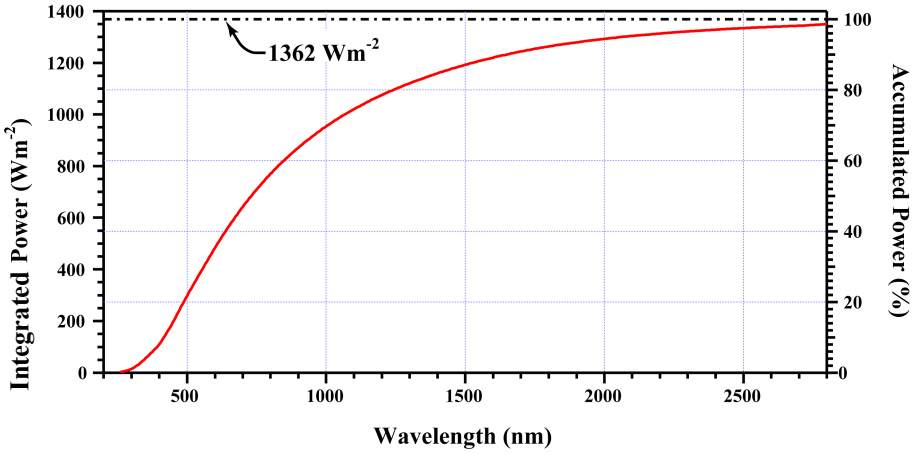

Figure 9: SIM integrated power versus wavelength.

Table 5 lists the TSIS SIM instrument properties and Figure 10 provides an expanded view of the TSIS SIM instrument. The TSIS SIM measurement requirements derived from analysis of the variability in spectral irradiance in the visible and infrared measured by the SORCE SIM instrument and incorporating the needs of the atmospheric and solar physics modeling communities are listed in Table 6. The SIM instrument error budget allocation is provided in Table 28.

Like the TIM, the primary detector for the SIM is an electrical substitution radiometer (ESR), which is essentially a bolometer where optical power is measured through heating instead of a photon to electron conversion. In traditional ESR designs, like TIM, the light collection is performed by a blackened cavity where light that is not absorbed on the first bounce is very likely to hit the cavity wall again resulting in around 99.99% light collection. However, for SIM, a diamond strip with NiP black (Section 3.2.5) on one side is used instead because the light levels are so low (dispersion from prism) and a cavity would have entailed too much thermal mass. To increase collection efficiency, a reflective re-imaging hemisphere of polished aluminum with a Magnesium Fluoride (Mg F2) coating sits on top of the diamond strip. Light not absorbed on the first bounce then reflects off the hemisphere and is for the most part re-imaged back onto the diamond strip.

Table 5: SIM instrument properties

Parameter	Value
Wavelength Range	200-2400 nm
Resolution	0.25-41 nm
Sun Viewing f/#	f/115
Focal length	400 mm
Prism Vertex Angle	34.3°
Front Surface Radius	421.5 mm
Back Surface Radius	441.3 mm (aluminized)
Prism Transmission	65-85% over wavelength range
Exit Slit Sizes	7.5 x 0.3 mm (7.5 x 0.34 mm for UV detector)
Entrance Slit	6.5 x 0.3 mm
Scan Range in Focal Plane	78 mm (78 mm / 60,000 subpixels = 1.3 μm/subpixel)
Shutter Frequency	0.01 – 0.05 Hz
Diffraction Correction	0.51-8.2%

When the shutter is open and the cavity illuminated with sunlight, reduced electrical heater power is needed to maintain the active ESR's temperature. This measured reduction in electrical heater power combined with calibrations of the absorptance of the diamond strip bolometer provides a measure of the entering radiant solar power. By accounting for the area of the exit slit (which defines the entrance aperture for the bolometer) and the prism rotation angle, the area and wavelength over which sunlight is collected is determined and when combined with the incident radiant power yields SSI (W m^{-2} nm^{-1}) in ground processing. Phase sensitive detection (Section 4.3) is used to reduce noise in post-processing.

Discussion of the SIM measurement geometry is provided in Sections 3.2.1- 3.2.4. Design elements of the SIM instrument including the ESR diamond strip bolometer begin in Section 3.2.5 and include the digital electronics needed to maintain a thermal balance between pairings of ESRs and the electrical heater which reduces power to the active ESR in order to maintain the balanced temperature in cases of incident sunlight. Also discussed is the Féry prism and prism drive (Section 3.2.9), the shutter that opens to allow incident sunlight to illuminate the ESR (Section 3.2.7) and the photodetectors used for rapid signal response (Section 3.2.11). A summary of the SIM observation modes is given in Section 3.2.12. Discussions of the SIM measurement uncertainties are provided in Section 5.

Table 6: SIM Measurement Requirements

Parameter	Requirement	Justification
Measurement Range ($Wm^{-2}nm^{-1}$) Spectral (200-2400 nm)	10^{-4} - 10^{1}	Solar Spectrum *Full scale of spectral irradiance magnitude*
Relative Stability (per year) $200 \le \lambda \le 400$ nm $400 \le \lambda \le 2400$ nm	0.05% 0.01%	Interpret Solar Cycle variability *UV variability 0.1%-10%* *Visible-Near IR variability ≤ 0.05%*
Measurement Precision Spectral (200-2400 nm)	0.01%	Measure Short-Term Variability *Sufficient SNR for Vis-NIR spectral variability*
Measurement Uncertainty Spectral (200-2400 nm)	0.2% from absolute	Climate Modeling Input *Earth radiation budget; Processes and Mechanisms*
Reporting Frequency (per day) Spectral (200-2400 nm)	2	Solar Temporal Variability *Sample short-term spectral variations with TSI*
Spectral Resolution (nm) $\lambda \le 280$ nm $280 \text{ nm} \le \lambda \le 400$ nm $\lambda > 400$ nm	 2 5 45	Solar Wavelength Variability *Strongest wavelength dependence of UV variability.* *Broader wavelength dependence of Vis-NIR variability.*

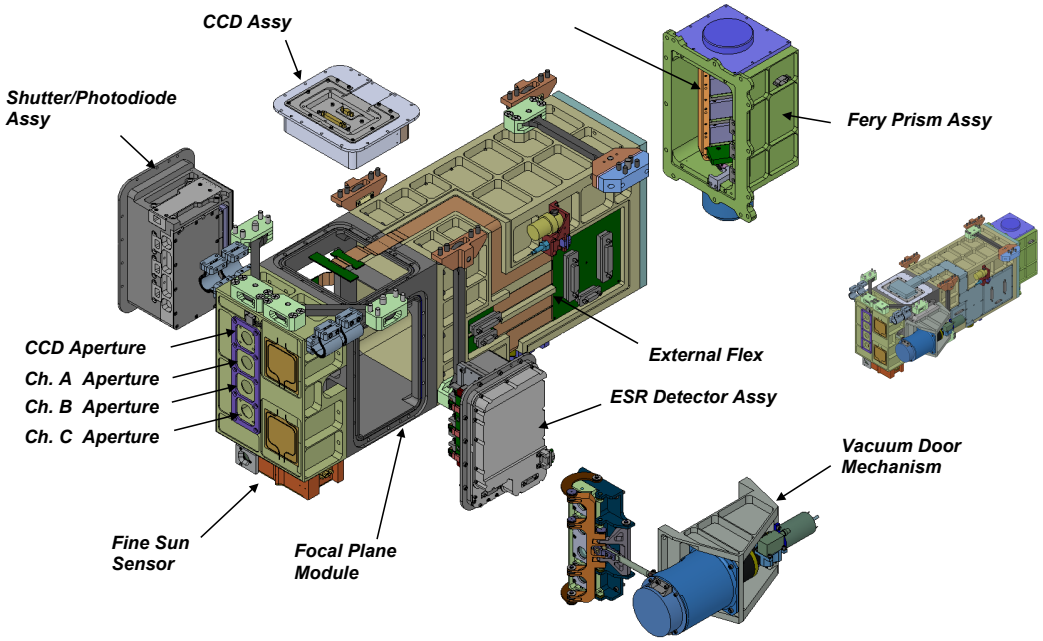

Figure 10: Expanded view of the TSIS SIM.

For normal operation, the opening and closing of a channel's shutter with a 100 second period modulates the sunlight entering the entrance slit as an f/115 beam directed to the Féry prism located 400 mm from the slit. Since the solar spectral irradiance varies dramatically over the SIM spectral range (see Figure 11), precise stability and knowledge of the prism position is required to resolve the solar structure at the SIM resolution. With precise knowledge of the prism rotation angle (obtained through a closed-loop controller that uses a CCD as a focal plane position encoder), the SIM provides an accurate measure of the index of refraction. There is a known and highly precise relationship between the index of refraction and the wavelength of incident light, including accounting for nonlinear temperature dependencies, which ultimately provides the knowledge of spectral solar irradiance to a relative wavelength error of < 150 ppm.

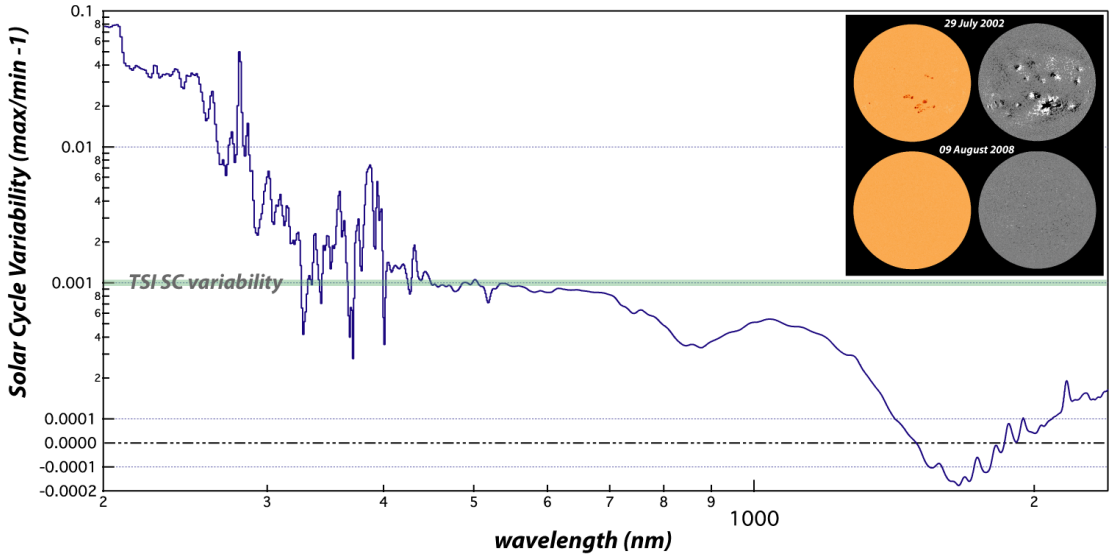

Figure 11: Modeled spectral variability of the rotational modulation of plage and sunspot contrast. Data is based on observation of UV (120-250 nm) and the NRLSSI model [*Lean et al.*, 2000]. The variability in SSI over solar cycle time scales spans 4 orders of magnitude across the SIM measurement range. The horizontal green line represents the level of variability in total solar irradiance over solar cycle time scales. Inset picture shows magnetic features on the Sun near solar maximum conditions (top) compared to quiet background conditions near solar minimum conditions (bottom). The visible features of solar activity are shown in white light (colored images) and grey images show the magnetic activity (magnetograms) that drives the irradiance variability.

3.2.1 Measurement Geometry

The SIM is a dual Féry prism spectrometer [*Féry*, 1910; *Rottman et al*., 1998; *Harder et al*., 2000] and has only the one optical element, a prism of fused silica glass (Suprasil 3001), which is used for spectral dispersion and image quality [*Harder et al*., 2000, 2005a, 2005b] (Figure 12). The prism has a concave front surface and a convex, aluminized rear surface that produces a dispersed and focused spectrum on the same plane as the entrance slit. The four exit slits (ESR detector and ultraviolet, visible, and infrared photodiode detectors) are located along the same focal place as the entrance slit. Detailed discussions of the TSIS SIM geometry, calibration, and measurement algorithms are provided in the SIM Calibration and Measurement Algorithms Documents (ref. in Table 1). An in-depth description of the design of the TSIS SIM, including changes from SORCE SIM are provided in the SIM Design Document (ref. in Table 1).

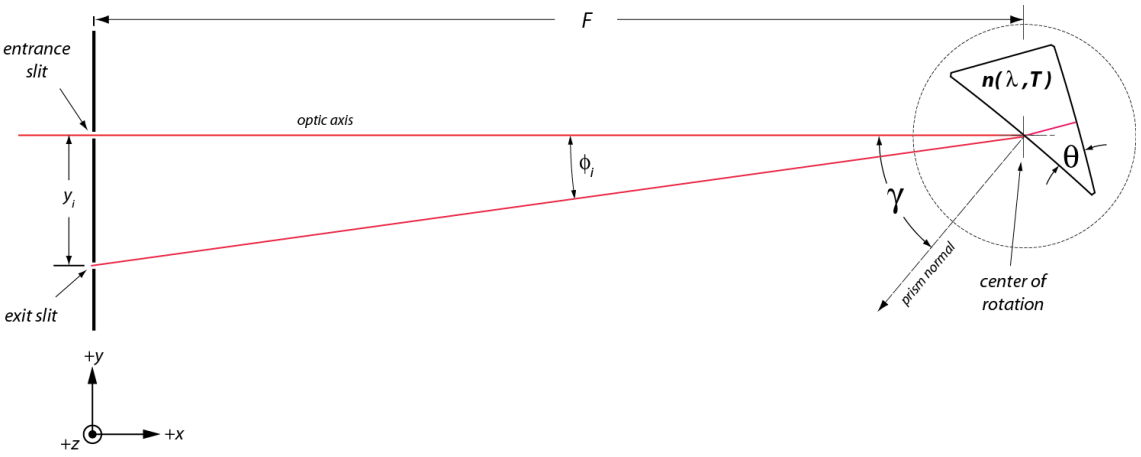

Figure 12: Overview of the SIM geometry in the dispersion plane identifying the critical dimensions: The optic axis of the instrument is defined by the line through the center of the entrance slit and the center of rotation of the prism. Each detector exit slit (y_i) defines a constant deviation angle (refraction angle), ϕ_i. Rotation of the prism changes the incidence angle, γ. There is a unique solution for the index, n, as a function of γ for each detector exit slit. Conversion of index to wavelength is accomplished through the Sellmeier dispersion equation for fused silica.

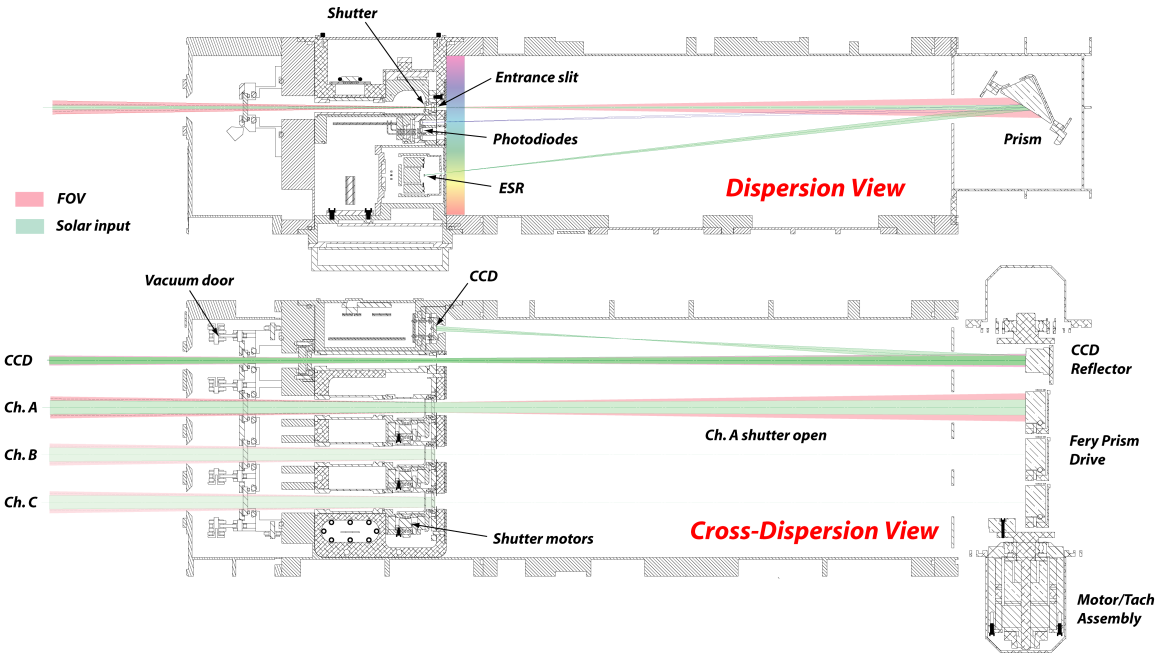

Figure 13: SIM instrument geometry in dispersion and cross-dispersion views.

The basic instrument geometry is a simple dispersion model derived from Snell's law for a plane prism in Littrow configuration. The variables are the prism incidence angle, γ, the deviation angle, ϕ, the refractive index, n, and the prism apex angle, θ, and the focal length, F. We define a *right-handed* coordinate system when referring to positions of the various components; the dispersion axis is the y-axis, cross-dispersion is the z-axis and the optic axis is along the x-axis, with the origin located at the center of the entrance slit. SIM operates as a constant deviation monochrometer, with fixed entrance and exit slits. The separation between entrance slit and exit slit is denoted by the focal plane displacement, y (origin at center of entrance slit). There are 4 exit slit locations for SIM corresponding to each of the detectors: UV diode (y = -10 mm), VIS diode, (y = -15 mm), IR diode (y = -20 mm) and the ESR (y = -45 mm). The positions of these exit slits have been chosen to best optimize the optical imaging performance for each of

the wavelength regions for the specific detectors. For the ESR in particular, that must cover the entire 200-2400 nm range, the exit slit location results in the best focal plane position to minimize optical aberrations across the spectrum.

The TSIS SIM uses 3 prism channels with the same optical layout. All three prisms are mounted on a common rotation yoke. For all channels, very accurate metrology is performed to measure all of the dimensional and angular displacements. The only free parameter is the prism incidence angle, γ, which is required for the solution of the Snell's refraction equation to convert index of refraction to wavelength (Section 3.2.4). Since all of the exit slits are fixed in the focal plane, the final refraction angles, ϕ_i, for each of the exit slits are fixed. If the incidence angle is known, then we can solve for the prism index of refraction, n, for each exit slit deviation angle (external medium index is known accurately since it is either air or vacuum). Once the index has been calculated and temperature corrected for each prism incidence angle, a wavelength can be calculated for each exit slit.

While the changes in index of refraction at the focal plane as a function of incidence angle are very nearly linear over the small angles scanned, the spectral resolution is a very strong function of wavelength and is directly related to the geometry and the optical dispersion of the fused silica prism material. This is the main disadvantage of a refractive system over a diffractive (grating) system where nearly constant resolution can be achieve over large spectral regions. However, for accurate spectral radiometric measurements, the prism design has several distinct advantages over a similar diffractive system. The refractive system is free of overlapping spectral orders that would require filters to remove unwanted out-of-band wavelengths. Furthermore, the spherical surfaces of the prism can be super-polished (typically to surface roughness < 1Å rms) and thus greatly reduces the scattered light.

3.2.2 CCD Geometry

The major challenge is the very precise control of the prism incidence angle to provide very consistent wavelength selection. This is especially critical for accurate radiometric measurements of the solar irradiance spectrum where large gradients in irradiance can occur over very small wavelength intervals (e.g. near Fraunhoffer lines). Ultimately small, unknown wavelength shifts will translate into spectral irradiance changes that could be falsely interpreted as solar variability.

In addition to the 3 solar viewing science channels for SIM, there is an additional solar viewing channel that provides a means for very precise angle control of the Féry prism rotation. This is a non-radiometric channel that maps angular coordinates of the prism rotation axis to linear coordinates at the focal plane. Having the angular control at the focal plane rather than at the axis of rotation minimizes possible errors caused by thermal and mechanical distortions of the instrument case between the focal plane and the prisms. The position of the light image on the linear CCD (located above the entrance slit) provides an angular measurement of the prism.

Due to the different TSIS SIM focal plane locations of the detectors and exit slits compared to SORCE SIM, it was not possible using the SORCE SIM CCD encoder design to cover the full angular range of the prism to achieve 200-2400 nm coverage for the ESR and also a minimum of 200 nm on the UV diode and maximum of 1700 nm on the IR diode. A new reflection system was designed around producing two separate image spots for optical encoding of the deviation angle. These spot images are separated in angle to achieve a different angular range of the prism. Each image spot can be independently commanded in closed loop servo control of the CCD encoder-Féry prism drive and therefore, collectively, can cover the full wavelength range. Additionally, the separation angle of the two image spots was chosen to allow for both overlap of scan ranges as well as ample margin at the extremes of the CCD pixels. This change required that the single spherical mirror from SORCE SIM be replaced with a double spherical mirror design that would simultaneously produce two separate image spots from the same entrance slit. The dual spherical mirror is fixed and coincident with the prism rotation axis. The system designed to achieve this is shown in Figure 14. The figure shows a full overview (in the prism dispersion plane) of the optical path of the reflection mirror and CCD encoder system.

The wavelength selection for each detector in the focal plane is achieved by prism rotation. Rotation produces a change in incidence angle, γ, between the optic axis and the prism first surface normal vector, n_p. We use the CCD pixels as a very precise positional "rule" at the focal plane. The full span is 78 mm with a resolution (d_{pix}) of 0.0013 mm yielding a precision of 16.7 ppm (1/60,000) in focal plane displacement coordinates. This results in an angular resolution of 0.34 arc-seconds.

Further details are available in the TSIS SIM Calibration and Validation Document (ref. in Table 1).

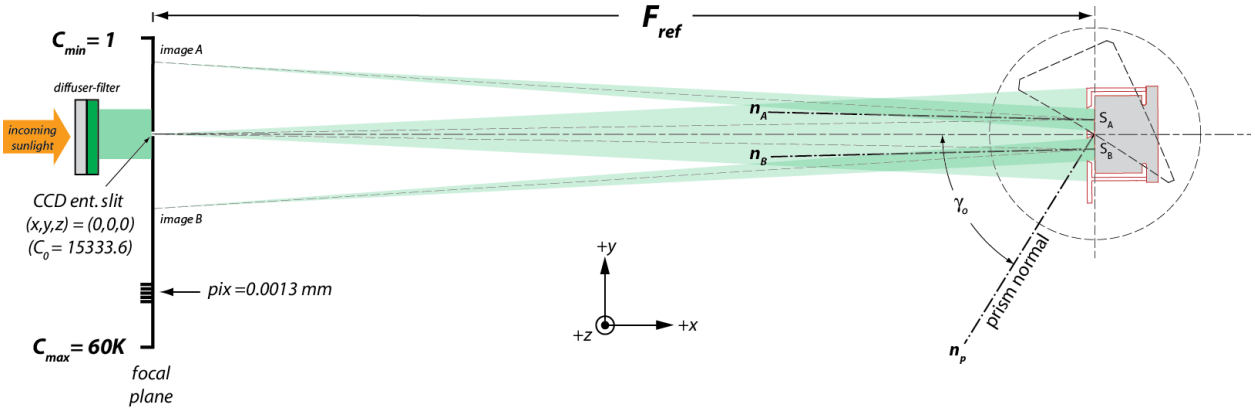

Figure 14: Overview of the SIM CCD angle encoder system: A 12000 element 6.5 µm pitch linear CCD is located at the focal plane above a 4mm x 0.1mm entrance slit. Incoming solar light passes through a quartz directional diffuser-green filter combination. The divergent light (~f/15) overfills a custom diamond turned dual spherical surface aluminum reflection mirror fixed and coincident with the prism rotation axis and the reflected light forms two 0.1 mm wide images (A & B) on the active area of the CCD. A closed-loop servo system allows for precise location control of either A or B across the 12K element CCD (sub-divided in timing to from 60K subpixels with a spacing of 1.3 µm.

3.2.3 Mapping Prism Angle to CCD Subpixel

A one-to-one mapping of prism angular coordinates to CCD subpixel linear coordinates is achieved for each of the image spots through a coordinate transform of the mirror surface normal vectors as a function of shaft rotation angle. The full coordinate mapping reduces to 3D spatial rotations of the surface normals with respect to rotation about the rotation axis. This coordinate transformation is accomplished through the use of *quaternions* (see SIM Design Document ref. in Table 1). Applying the full quaternion calculation to the chief rays for mirror A and B through the 3D geometry of the CCD optical system generates the mapping of prism incidence angle to CCD subpixel. SIM CCD and prism geometry parameters are provided in the TSIS SIM Calibration and Validation Plan (ref. in Table 1).

3.2.4 Mapping CCD Subpixel to Wavelength

For the SIM optical geometry, the fundamental refraction relationship for the chief ray (under vacuum where $n_{ext} = 1$) is given by Equation 3.2.4.1

$$2\theta = \sin^{-1}\left[\frac{\sin(\gamma)}{n_p}\right] + \sin^{-1}\left[\frac{\sin(\gamma - \phi)}{n_p}\right] \qquad (3.2.4.1)$$

where θ is the prism apex angle, γ is the prism incidence angle, ϕ is the fixed deviation angle for a given detector slit and n_p is the index of refraction of the Suprasil 3001 fused silica prism.

This equation can be rearranged to give the relationship of the index of refraction solution for each exit slit location i (i = ESR, UV, Vis, or IR) as a function of prism incidence angle

$$n_i = \frac{1}{sin[2\theta]}\sqrt{sin^2[\gamma] + 2cos[2\theta]sin[\gamma]sin[\gamma-\phi_i] + sin^2[\gamma-\phi_i]} \qquad (3.2.4.2)$$

where, for each detector slit,

$$\phi_i = \tan^{-1}\left(\frac{y_i}{F}\right) \qquad (3.2.4.3)$$

All angles, except for γ, are fixed and invariant in the SIM geometry. Therefore, a one-to-one mapping of prism incidence angle to index of refraction for each detector is achieved and, ultimately, a one-to-one mapping of subpixel to index for each CCD image spot. The index solution is nearly linear with subpixel. Further details can be found in the TSIS SIM Calibration and Validation Plan (ref. in Table 1).

The Sellmeier equation (Equation 3.2.4.4) is an empirical relationship between the refractive index, n, and the wavelength, λ, for a particular transparent medium at a given temperature. For Suprasil 3001 (fused silica) it is given by the following equation, with the Sellmeier dispersion coefficients (at 20°C). The one-to-one mapping from CCD subpixel to wavelength for TSIS SIM is shown in Figure 15. The index of refraction has a temperature dependence and the prism temperature is regulated on orbit to ±2°C (Section 3.2.9.2). We accurately measure, to better than 0.1°C, the temperature of each channels' prism via a thermistor, which is bonded to the base of each prism.

$$n_{20}(\lambda) = \sqrt{1 + \sum_{i=1}^{3}\frac{\lambda^2 K_i}{(\lambda^2 - L_i)}} \qquad (3.2.4.4)$$

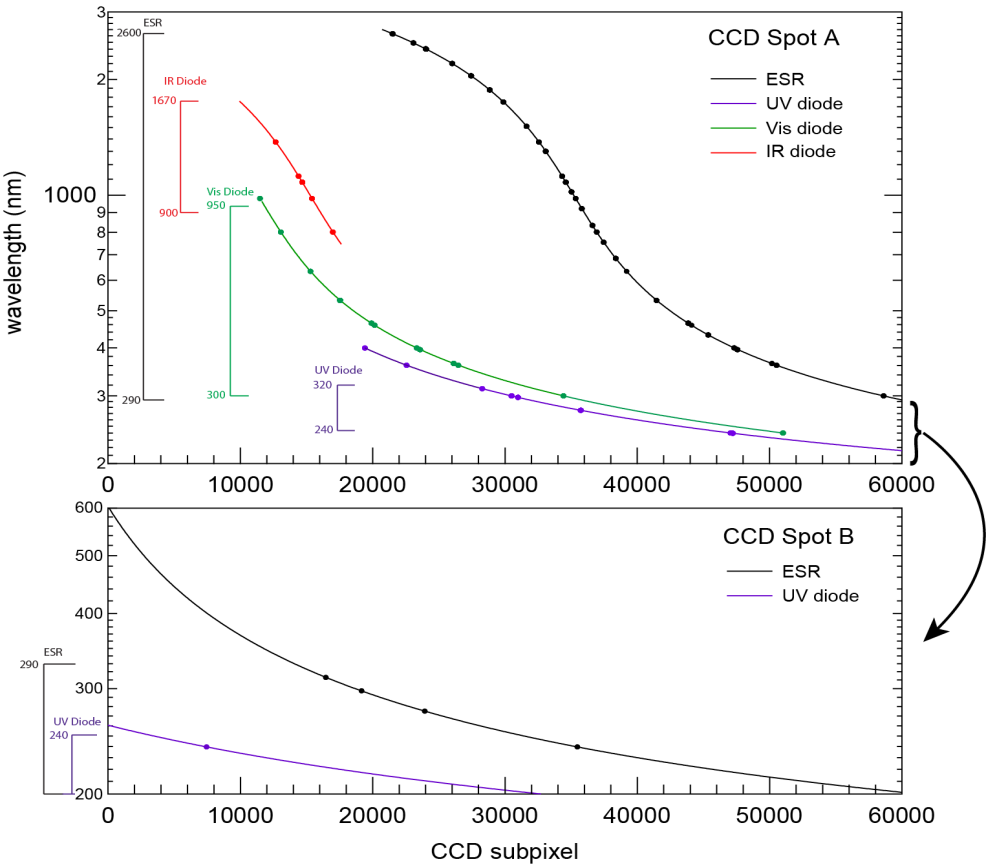

Figure 15: CCD subpixel to wavelength mapping for TSIS SIM: Lines are modeled solutions. Points are calibration data points.

3.2.5 Electrical Substitution Radiometer

The SIM electrical substitution radiometer (ESR) is the on-orbit reference for the measurement of optical power in SIM. Because the ESR is essentially a bolometer, where optical power is measured through heating instead of a photon to electron conversion, the responsivity is very constant as a function of wavelength. Thus we can use the ESR as a detector standard across the entire 200-2400 nm spectral range.

The ESR is designed to collect nearly 100% of the light that passes through the exit slit and measure it as heat. Because the light levels are so low for the SIM ESR, a cavity such as that used for the TIM ESR, would entail too much thermal mass. To minimize the thermal mass a diamond strip was used. Physically, each separate ESR consists of a 1.5x10 mm diamond strip bolometer with NiP black on one side, a picture of which is shown in Figure 16. There are thermistors soldered at the two ends, and a thin film replacement heater on the back. The bolometer is glued to Vespel "toadstools" that are in turn glued to kapton tubes that provide the weak thermal link to the copper heat sink.

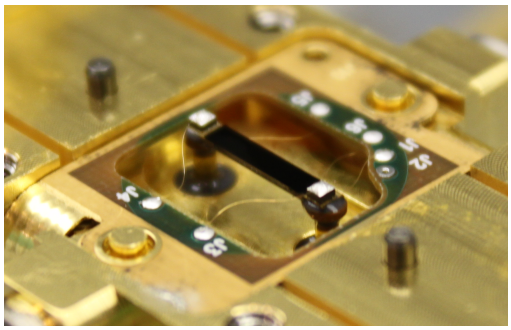

Figure 16: Photograph of a TSIS SIM diamond strip bolometer: The SIM ESR consists of three of these bolometers, one for each channel.

A reflective hemisphere, which reimages light reflected off the NiP back onto the NiP, sits over the bolometer. To increase collection efficiency, light not absorbed on the first bounce then reflects off the hemisphere and is for the most part re-imaged back onto the diamond strip. Additionally, the light is incident onto the NiP surface at an ~6.5° angle. Thus the specular component of the reflected light falls onto the hemisphere, and is not redirected back towards the slit. For the TSIS SIM design, assuming a perfectly reflective hemisphere, 86% of the light not absorbed by the NiP will be reimaged back onto the NiP by the hemisphere. This is a significant improvement over the SORCE SIM design where 44% of the light would be reimaged back onto the NiP.

Finally an "exit slit", with dimensions of 0.3x7.5 mm, defines the entrance aperture for the bolometer. The SIM ESR consists of three of these bolometers, one for each SIM channel.

3.2.5.1 Basic Thermal Design

Knowledge of the thermal design and performance of the ESR is very important since optical power is detected by the measurement of the amount of electrical *substitution* necessary to generate an equivalent change in the measured temperature. The ESR assembly is designed as a series of thermal masses connected by thermal links (Figure 17), where each element is characterized by a thermal heat capacity (Joules/Kelvin) and the connections between elements are characterized by their thermal conductance (Kelvins/Watt). This model oversimplifies the system as each of the thermal links has a non-zero heat capacity, and there are weak heat links between seemingly unconnected elements, such as the Copper block and the mount. Nonetheless, this model provides a useful framework for characterization of the ESR. The calculation of the thermal properties for the SIM ESR are described in Section 5.3.

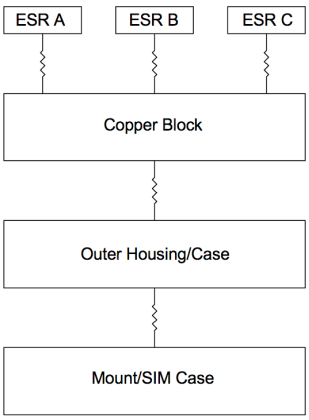

Figure 17: A simplified thermal block diagram of the SIM ESR assembly.

3.2.5.2 Basic Electrical Design

There are two key elements to the ESR electrical design: the bolometer temperature measurement and the bolometer heater control.

3.2.5.2.1 Bolometer Temperature Measurement

The temperature measurement of the ESR is a relative measurement of the temperature *difference* between two bolometers. By measuring the difference, and not the absolute temperature of a single bolometer, common mode effects are canceled out. For instance, if the temperature of the copper block heat sink changes, this induces a temperature change in both bolometers, and so to first-order it will not cause a *difference* signal. Similarly, when both bolometers are looking at the same thermal radiation environment, that environment can change in temperature and it will not induce a difference signal. The only way to induce a difference signal is when the heat load changes on one bolometer, and not the other.

A simplified depiction of the circuit is shown below:

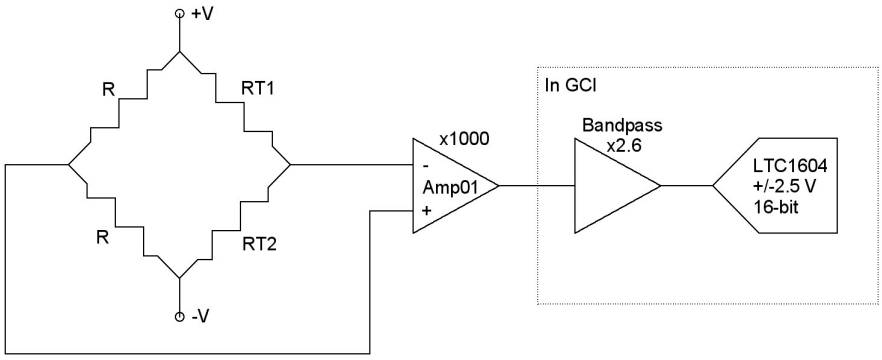

Figure 18: Simplified depiction of SIM ESR electrical design for the bolometer temperature measurement. RT1 and RT2 are the two bolometers. Making up the other arm of the bridge are two precision fixed resistors, R. The applied voltages, +V and –V, are one volt amplitude sine waves; -V is 180° out of phase with respect to +V. The AMP01 is an amplifier, which amplifies the difference between the two arms of the bridge by 1000 times. The signal is passed to a GCI and into an analog-to-digital converter (ADC), where the voltage is sampled by a digital signal processor (DSP). The effective 'gain', or change in digital numbers (DN's) per degree change in one bolometer is 10.8 nK/DN.

In Figure 18, each bolometer thermistors is composed of two 10 kΩ chip thermistors wired in parallel to give approximately 5 kΩ. The chip thermistors were carefully screened so that the resistance at a fixed temperature is very similar for each of the six thermistors that make up the three ESRs. The precision fixed resistors, R, have a resistance of 1 kΩ. The applied voltages, +V and –V, are in fact one-volt amplitude 50 Hz sine waves. The amplitude of the –V sine wave is the negative of +V; alternatively –V is 180° out of phase with respect to +V. The difference between the two arms of the bridge is then amplified by 1000 times by an AMP01 instrumentation amplifier. This voltage then passes along a wire harness to the GCI, where it passes through an amplifying (x2.6) band-pass filter and finally into an ADC. The DSP samples this voltage at 12.8 kHz, and so acquires 256 points over a 50 Hz cycle of the sine wave. Finally, this array of acquired voltages (now in raw data numbers (DN) from the ADC) is multiplied internally in the DSP by a unity amplitude sine wave and summed to get the amplitude of the signal at 50 Hz. If we calculate the change in DNs for a degree change in *one* of the bolometers, we find an effective "gain" of this measurement chain of 91971668 DN/K, or 10.8 nK/DN.

3.2.5.2.2 Bolometer Heater Control

Most of the heater control circuit is the drive electronics; the three elements that are relevant for the ESR are the +7.1 voltage reference (*Vref*), the 100 kΩ resistor, and the bolometer heater, R_H. When power is applied to the ESR, the +7.1 V voltage reference is applied to the series combination the 100 kΩ and ESR heater R_H. Thus, the power applied to R_H is:

$$P = R_H \left(\frac{Vref}{100k\Omega + R_H} \right)^2 \qquad (3.2.5.2.2.1)$$

The ESR heater is approximately 100 kΩ, and the maximum power applied to the ESR is ~126 μW. Reducing heater power is accomplished by using pulse-width modulation. The applied voltage, rather than DC, is a 100 Hz square wave, with varying duty cycle. To apply full power, the duty cycle is 100%. To apply half-power, or about 60 μW, the duty cycle is adjusted to 50%. There are two significant benefits to this technique:

1. The duty cycle can be controlled by adjusting the duty cycle of a TTL signal and controlled digitally. Digital timing control is very accurate and fine adjustments of the duty cycle are very straightforward.
2. Reducing the applied power is linear with respect to duty cycle. This allows the gain of the closed loop system to remain constant with power changes.

With regard to the drive circuit, when the pulse-width-modulator (PWM) is low (0 V), the 2N2222 transistor is not conducting any current, and so +15 V is applied to the gate of the MOSFET. Initially, the gate-source voltage is +15, and so the MOSFET turns on hard. Once current begins flowing, the gate-source voltage drops to ~7.9 V (there is a 7.1 V drop across the resistors following the MOSFET), but this is sufficient voltage to keep the MOSFET open. When the PWM is high (5 V), the 2N2222 transistor is saturated and all of the current from the +15 V flows through the 10 kΩ resistor and through the transistor, leaving the gate of the MOSFET at 0 V. With the MOSFET gate at 0 V there will be no voltage applied to resistors following the MOSFET.
Further details can be found in the TSIS SIM Flight ESR Calibration (ref. in Table 1).

3.2.6 Precision Entrance Slit

The precision entrance slit determines the amount of light entering the instrument, thereby providing the 'per m^2' term in solar spectral irradiance [W m^{-2} nm^{-1}]. The nominal entrance slit dimensions are 6.5 mm in length by 0.3 mm in width. The area of the entrance slit was precisely calibrated at the NIST aperture area measurement facility in Gaithersburg, MD for area calibration. This consists of a high-accuracy 2-axis platform and an inspection microscope through an automated system that measures a series of points along the edge of an aperture. The points are then fit to the aperture geometry (in our case a rectangle) and the uncertainty in the dimensions is found using the Monte Carlo "bootstrap" technique. The convolution of the width of the exit slit with the width of the entrance slit, along with the optical properties of the prism, determines the instrument bandpass (i.e. dispersion) thereby providing the 'per nm' term in solar spectral irradiance.

3.2.7 Shutters

Each channel has an independent shutter that opens or closes in approximately 10 ms, which modulates the incoming light beam. The shutter frequency is selected to minimize ESR detector noise. The shutter open and close times are characterized and accounted for in the post-processing phase sensitive analysis (*Kopp and Lawrence*, 2005, *Kopp et al*., 2005a, and Section 4.3.2). An engineering model SIM shutter mechanism was tested to 3,679,200 cycles. A daily average shutter cycle number was estimated using the daily operational plan (see Section 3.2.12.3, Figure 22), requiring 185 cycles per day, which is equivalent to 67,500 cycles per year. The lifetime of the primary cavity's shutter exceeds the 5-year TSIS mission lifetime.

3.2.8 Equivalence Ratio

As discussed in Section 3.1.7, this ratio will be close to one since the thermal conduction paths are quite similar. By excluding data near a shutter transition, and where the filter gain is high, we lessen sensitivity to this ratio.

3.2.9 Optical Property (Féry Prism)

For normal operation, the opening and closing of a channel's shutter with a 100 second period modulates the sunlight entering the nominally 0.3 x 6.5 mm entrance slit (precision measured at NIST) as a f/115 beam directed to the Féry prism located 400 mm from the slit. The prism has a concave front surface and a convex, aluminized rear surface that produces a dispersed and focused spectrum on the same plane as the entrance slit. The four exit slits (ESR detector and ultraviolet, visible, and infrared photodiode detectors) located along the focal place are nominally 7.5 x 0.3 mm in size, with the exception of the UV slit, which is 7.5 x 0.34 mm in size. These detectors are located at 10 mm (UV diode), 15 mm (Visible diode), 20 mm (IR diode), and 45 mm (ESR) from the entrance slit.

The prism is fabricated from Suprasil 3001 [*Hereaus Amersil, Inc.*]. This fused silica material has a low OH concentration (<1 ppm by mass) that gives it a smooth transmission function in the NIR. It also has outstanding radiation hardness (>10^8 Rad); tests of fused silica on the Long Duration Exposure Facility showed only a slight, washable, degradation [*Harvey et al*. 1992]. The index of refraction of Suprasil 3001 is calculated from the Sellmeier Equation (Section 3.2.4) to ±30 ppm. The index of refraction has a temperature dependence of less than 10 ppm over a broad range in temperature (0-40° C), so the prism temperature will be regulated to ±2°C with 0.04°C knowledge of variations [*Malitson,* 1965].

3.2.9.1 Dispersion

Based on the refractive geometry of the SIM optical configuration, we can make use of the available parameters to obtain the linear reciprocal dispersion (nm/mm) at the focal plane (Equation 3.2.10.1.1) through the use of three factors

$$\frac{d\lambda}{dy} = \left(\frac{d\lambda}{dn}\right)\left(\frac{dn}{d\phi}\right)_{\gamma}\left(\frac{d\phi}{dy}\right) \qquad (3.2.10.1.1)$$

The first term is the first derivative of the inverse Sellmeier (Equation 3.2.10.1.2), or more conveniently we can make use of the relation $dn/d\lambda$ and differentiate the Sellmeier equation with respect to wavelength

$$\left(\frac{d\lambda}{dn}\right) = \left(\frac{dn}{d\lambda}\right)^{-1} = -\frac{n}{\lambda}\left[\sum_{i=1}^{3}\frac{K_i L_i}{(\lambda^2 - L_i)^2}\right]^{-1} \qquad (3.2.10.1.2)$$

$$\left(\frac{d\phi}{dy}\right) = \frac{F}{F^2 + y^2} \qquad (3.2.10.1.3)$$

and the dispersion relationship at constant prism incidence angle is

$$\left(\frac{dn}{d\phi}\right)_{\gamma} = -\frac{\cos[\gamma - \phi]}{\sin[2\theta]}\sqrt{1 - \frac{\sin^2[\gamma]}{n^2}} \qquad (3.2.10.1.4)$$

3.2.9.2 Prism Transmission

Once the prism incidence angle have been determined from subpixel location (Section 3.2.3), the full Fresnel transmission loss expected from entrance slit to each exit slit location can be determined. The full optical transmission loss is the product of the Fresnel transmission loss and the wavelength dependent aluminum reflectivity from the back surface of the prism.

The Fresnel equations (Equation 3.2.10.2.1) yield the reflection and transmission of electromagnetic waves at an interface either parallel (*p*-polarized) or perpendicular (*s*-polarized) to the plane of incidence. For the SIM prism geometry, the first interface ('*in*') is the vacuum-to-glass reflection/refraction and the second ('*out*') is the glass-to-vacuum reflection/refraction after full (nearly normal) reflection off the Aluminum coated back surface. Recall that γ is the prism normal angle and β is the wedge half angle.

$$R_s^{in} = \left[\frac{\sin(\gamma_1 - \beta_1)}{\sin(\gamma_1 + \beta_1)}\right]^2 \;;\; R_s^{out} = \left[\frac{\sin(\beta_2 - \gamma_2)}{\sin(\beta_2 + \gamma_2)}\right]^2$$
$$R_p^{in} = \left[\frac{\tan(\gamma_1 - \beta_1)}{\tan(\gamma_1 + \beta_1)}\right]^2 \;;\; R_p^{out} = \left[\frac{\tan(\beta_2 - \gamma_2)}{\tan(\beta_2 + \gamma_2)}\right]^2 \qquad (3.2.10.2.1)$$

Since the solar incident light is unpolarized (i.e. containing an equal mix of s- and p-polarizations), the reflection coefficient is $R = (R_s + R_p)/2$. The total transmission (Equation 3.2.10.2.2) is therefore $T = 1\text{-}R$ where $R = (R^{in} \times R^{out})$ and can be expressed as,

$$T = \frac{1}{2}\left[\left(1 - \left\{\frac{tan[\gamma_1 - \beta_1]}{tan[\gamma_1 + \beta_1]}\right\}^2\right)\left(1 - \left\{\frac{tan[\beta_2 - \gamma_2]}{tan[\beta_2 + \gamma_2]}\right\}^2\right) + \left(1 - \left\{\frac{sin[\gamma_1 - \beta_1]}{sin[\gamma_1 + \beta_1]}\right\}^2\right)\left(1 - \left\{\frac{sin[\beta_2 - \gamma_2]}{sin[\beta_2 + \gamma_2]}\right\}^2\right)\right] \qquad (3.2.10.2.2)$$

3.2.10 Instrument Profile

After light enters the precision entrance slits, the light is dispersed by the prism and imaged on an exit slit. The selected wavelength (λ_s) and spectral bandpass ($\Delta\lambda$) of the light that is transmitted through the precision-measured exit slits and impinges on the detector is affected by the geometry, orientation, and index of refraction of the prism, and the widths of the entrance and exit slits. The length, width, and area of the ESR exit slits are precisely measured by NIST and in-flight variability due to thermal expansion and contraction will be corrected for.

The absolute instrument profile is measured by illuminating the instrument with a single wavelength and a known irradiance (measured using the NIST cryogenic radiometer). The measurement signal varies with prism angle. The absolute instrument profile proves useful for determining the instrument function area (i.e. the integrated area of profile), absolute sensitivity (given by the absolute height of the profile), wavelength calibration (center location of profile provides wavelength calibration), and scattered light (background level of profile). Sections 5.3.2 and 5.3.7 go into further detail of the wavelength and instrument line shape calibrations.

3.2.11 Photodiode Detectors

The ESR precisely measures spectral irradiance (W m^{-2} nm^{-1}) over the full spectral range (200-2400 nm) at a slow (~ 10 second) cadence due to dwell time. Therefore, the SIM also includes 3 secondary diode detectors which are each capable of a more rapid response time but restricted to a limited spectral range and to lower absolute accuracy. N-on-p silicon diodes are used for the UV (200-315 nm) and visible (310-950 nm) channels, and an indium gallium arsenide (InGaAs) diode is used for the IR channel (900-1695 nm). The photodiodes have a noise floor about 10^5 below that of the ESR, are insensitive to thermal infrared radiation, but are not absolute detectors because they lack the stability and absolute accuracy of the ESR. The photodiodes are therefore calibrated against ESR signals to reduce noise (see Section 7.2). Each photodiode current is read by a low voltage offset, trans-impedance amplifier. The four output signals are multiplexed and read by the ESR Digital Signal Processor (DSP) unit; data are sampled once every 0.01 seconds and are decimated by the DSP by the same multiplier used for the ESR.

3.2.11.1 Dual Slope ADC

A dual slope integrating analog-to-digital converter (ADC) has greatly improved the dynamic range of TSIS SIM photodiode signals. The dual slope method utilized for TSIS SIM has an effective 21 bit (20.93 actual) resolution compared to the effective 15 bit resolution for SORCE SIM, which was affected by "bit-noise" limitations at wavelengths (around 300 nm-380 nm) with small signals.

In a dual slope method, the measured input voltage is computed from accurate knowledge of three measured quantities: T_{fixed}, a fixed duration over which the measured signal is integrated, $T_{measured}$, a accurately measured time over which the capacitor discharged once the input signal is switched to a reference voltage, and V_{ref}, the pre-launch calibrated reference voltage. The cycle from charge through discharge is called the Photodiode Acquisition Rate (PDAR), and is a total time equal to the sum of integration, conversion (i.e. de-integration), and an autozero period. The integration time is commanded (i.e. fixed) and the auto zero time is variable. De-integration times vary upon photodiode properties and measured signal.

3.2.11.1.1 General Background

In operation, the integrator is first zeroed (effectively achieved by shorting the integrating capacitor). At time $t = 0$ the unknown input voltage, V_{in}, is applied to the input resistor R by closing switch SW_1 for a fixed length of time, accurately known by defining a preset number of counts, M, from the precision clock. At the end of the integration period the input voltage is given by Equations 3.2.13.1.1.1.

$$V_x(t_{\text{int}}) = \frac{1}{RC}\int_0^{t_{\text{int}}} V_{in}(t)dt$$

$$V_x(M) = \frac{1}{RC}\sum_i^M V_{in}(i) = \frac{MV_{in}}{RC} \qquad (3.2.13.1.1.1)$$

Immediately after the end of integration, a known reference voltage (of opposite polarity to V_{in}) is connected to the same input resistor R (through the same switch). The time is then accurately measured to completely discharge the capacitor again by measuring the counts, N, form the same precision clock initiated at the start of discharge (switch closure) and terminated at $V_x = 0$.

$$V_x(M+N) = \frac{MV_{in}}{RC} - \frac{NV_{ref}}{RC} = 0 \qquad (3.2.13.1.1.2)$$

Therefore, determination of the unknown input voltage simplifies to Equation 3.2.13.1.1.3.

$$V_{in} = V_{ref}\left(\frac{N}{M}\right) \qquad (3.2.13.1.1.3)$$

The main advantage of the dual-slope integrating ADC technique is that it is insensitive to values of the circuit parameters. In particular, the conversion results are insensitive to errors in the component values; the values of R, C, and T_{clk} all cancel from the final relationship. Furthermore, since the deintegration immediately follows the integration period, the temperature dependence of the values is largely removed from the results.

3.2.11.1.2 Application in TSIS SIM

In TSIS SIM, a dual slope integrating ADC is implemented for each photodiode detector (UV, Vis and IR). Following Equation 3.2.13.1.1.3 above, the input voltage from the photodiode transimpedence amplifier, V_{in}, (at each wavelength position) is computed from accurate knowledge of three measured quantities: The fixed signal integration time, defined by M counts from a precision 2 MHz clock (UV diode:1.5 sec; $M = 3e^6$ cts, Vis/IR diode: 0.5 sec; $M = 1e^6$ cts), the variable de-integration time to discharge to $V = 0$ corresponding to N counts from the same 2 MHz clock, and $-V_{ref}$, the pre-launch 7.1 V calibrated reference voltage.

The slope of the integration period in Figure 19 will be dependent upon the input voltage and the fixed integration time interval and will therefore vary. However, the slope of the deintegration period, which is dependent upon the 7.1 *V* reference voltage will have constant slope although the time interval over which the deintegration occurs will vary. For V_{in} values near 7.1 *V*, the de-integration time will be nearly the same as the integration time. Modeling studies were performed to ensure that peak signals are very near 7.1 *V* for integration times of 0.5 seconds in the visible, near infrared and ultraviolet wavelengths longer than 250 nm. For wavelengths shorter than 260 nm a larger integration time will be commanded (1.5 sec) as measured signals are small (maximum signals less than 1 *V* based on modeling simulations) leading to deintegration times in the 2-60 msec range.

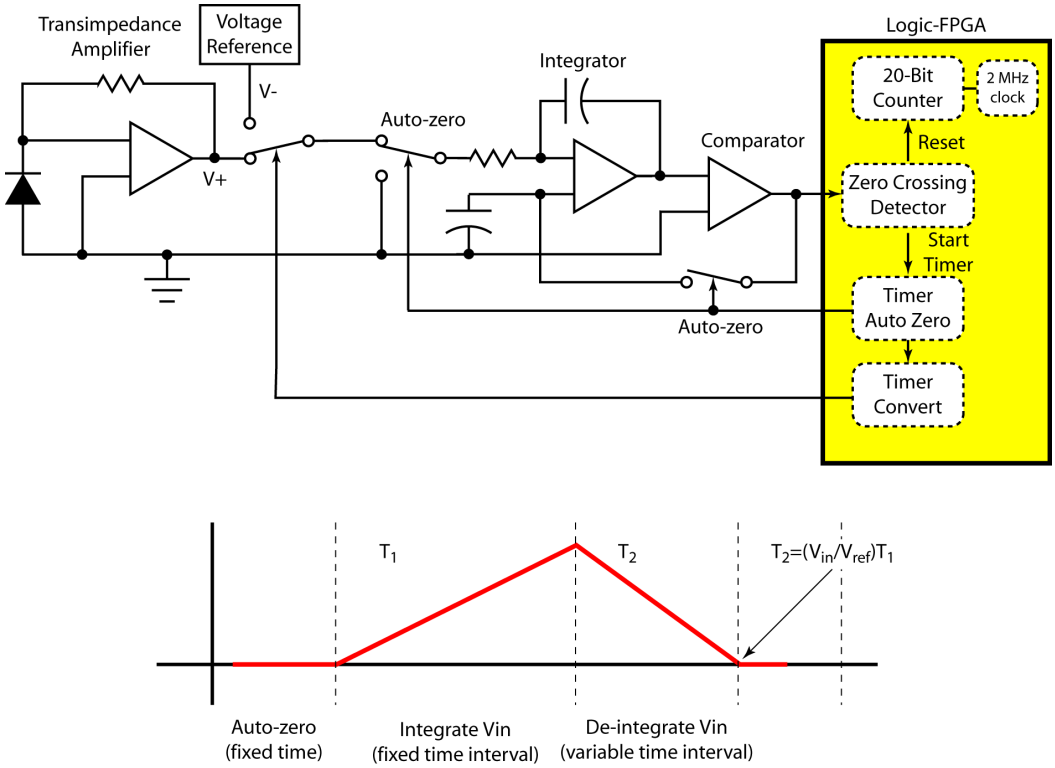

Figure 19: TSIS SIM dual slope ADC concept: An effective 21-bit A/D precision with signal integration improves photometric precision.

3.2.11.2 Photodiode Acquisition Rate (PDAR)

The cycle from charge through discharge is called the Photodiode Acquisition Rate (PDAR), and is a total time equal to the sum of integration, conversion (i.e. de-integration), and an auto-zero period. The integration time is commanded (i.e. fixed) and the auto zero time is variable. Deintegration times vary upon photodiode properties and measured signal. For example, based on a maximum time to integrate a signal of 7 Volts, the IR photodiode will de-integrate in approximately 400 milliseconds (msec), the visible photodiode in 5-400 msec, and the UV photodiode in 10-400 msec. Based on these maximum deintegration times and accounting for an auto-zero period, all PDAR periods will be 2 seconds long.

Figure 20 provides an example of SIM photodiode signal integration during three consecutive PDAR periods. The green lines represent integration periods; the slopes of these green lines are variable depending on measured signal. The blue lines represent the conversion or 'deintegration' periods; while the conversion periods take different amounts of time, they all have the same slope. When the commanded time of integration is met, the circuit switches over to the 7.1 V reference voltage and the conversion period begins. An auto-zero period starts when the signal crosses the 0 V line, and lasts for the remainder of the PDAR cycle (i.e. the auto-zero period will last until the 2 second PDAR

period has been met). Note that the prism angle (CCD pixel) is commanded to change during the conversion period. This ensures that any "jitter" in the measured signal upon that occurs during moving the prism to the next commanded CCD position has settled prior to the start of the next integration period, indicated by pink arrows in Figure 20.

PDAR cycles are always running, whether the shutter is cycling for ESR scans or not. A commanded priority flag determines the priority of the ESR or photodiode detectors in a particular experiment. For example, when the photodiode detectors are priority, the start of the de-integration period is tied to the time of prism movement ensuring that the prism position is stable during integration periods. During ESR priority periods, the timing of prism movement is tied to the shutter open-close cycle. However, since PDAR is always running, the prism position could move during a PDAR integration period when in ESR priority mode and post-processing procedures will filter diode data impacted by prism movement. This filtering is expected to have minimal impact on the concurrent diode data obtained during ESR priority mode as approximately 10-35 PDAR cycles will be obtained per stable prism position, greatly outnumbering the number of PDAR cycles negatively affected by prism movement.

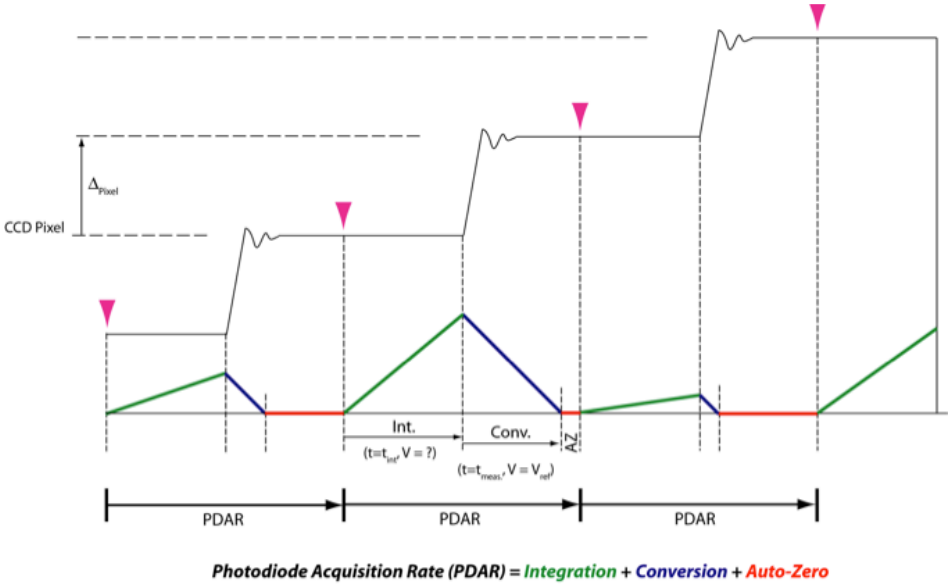

Figure 20: Example of SIM photodiode signal integration in three consecutive PDAR periods.

3.2.12 Science Operation Modes

To aid the interpretation of the daily TSIS SIM operations, we first provide a review of the mapping from CCD subpixel to wavelength and the determination of the subpixel step size.

3.2.12.1 Review of CCD subpixel to wavelength mapping

The necessity for a double spot CCD encoder was introduced in Section 2.4.3.1 and discussed further in Sections 3.2.3 and 3.2.4. The CCD functions as a focal plane position encoder that provides precise knowledge of the prism rotation angle. The accurate measure of the index of refraction measured by the SIM and the knowledge of the prism rotation angle are used in a known and highly precise relationship to determine the wavelength of the incident light. Both CCD spots are commandable, and measurements across the full wavelength scale are obtained, as shown in Figure 21. With the prime "nominal" scan, measurements at wavelengths from 207 – 2400 nm (even as long as 2700 nm) are obtained with coverage from 200 - 618 nm obtained with the extended "UV" scan.

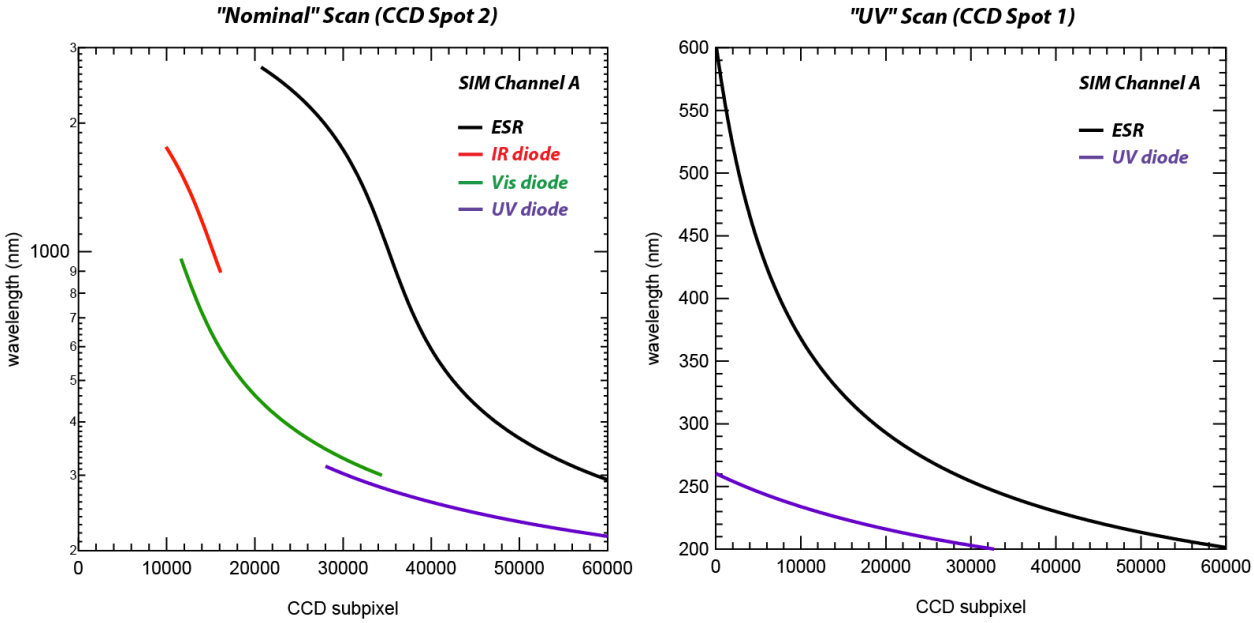

Figure 21: TSIS SIM CCD subpixel to wavelength mapping: The known relation between prism angle and wavelength is shown for all detectors for the "nominal" scan (CCD spot 2), and the "UV" scan (CCD spot 1). Knowledge of this relationship is used for defining the start and stop pixel in SIM operations. This figure represents the dispersion properties of the SIM instrument.

3.2.12.2 Review of Sampling: Choice of subpixel step size

Ideally, the convolution of the instrument exit slit with the entrance slit, which defines the spectral bandpass, or "slit width", of the instrument, will look like a triangle. However, aberrations in the instrument optics, such as coma, cause deviations from this ideal shape. For TSIS SIM, these optical aberrations have been defined and calibrated through laser scans. The slit width is constant in subpixel space (230 subpixels wide for the ESR detector, and visible and infrared photodiodes and 261 subpixels wide for the ultraviolet photodiode, where each subpixel is 1.3 microns in width), but not in wavelength space due to the dispersive properties of the prism.

Per the Nyquist sampling theorem, at least two measurement samples per slit width are required to prevent aliasing, or the inability to distinguish different signals from one another, in the detected signal. For TSIS SIM, the subpixel step size is chosen to provide sufficient sampling across the spectral resolution element and ranges from 4-6 samples per slit width (this sampling applies to photodiode and ESR scans). For example, 6 samples across a 300 micron wide exit slit where each subpixel is 1.3 microns in width is equivalent to approximately 38 CCD subpixel steps. Note that operating at 4 samples in the infrared region (1500 nm - 2400 nm) for TSIS SIM is double the sampling resolution used in SORCE SIM over this wavelength range.

3.2.12.3 Daily Operations

The SIM operations consisting of the activities described below will occur over 16 orbits every day according to the timeline shown in Figure 22. Here, we provide a summary of the daily operations. Further details can be found in the TSIS Insrument Operations Concept document (ref. in Table 1). The total daily solar exposure on the channel A prism will be around 200 minutes. The first 8 orbits of activities will provide full photodiode scans between 200 nm-1695 nm (the UV portion between 200 and 260 nm will be scanned again), and a variable (in spectral range) ESR scan measurement that is performed first on Channel A and then repeated (for the same spectral range) on Channel B on the consecutive orbit. The second 8 orbits of activities will provide another full diode scan, the full range of the ESR IR (1500-2405 nm), and perform ESR gain and dark calibrations. Typically, these calibration scans will be performed daily and used to correct the diode measurements for changes in the radiant sensitivity. However, periodic diagnostic

operations, such as cruciform maps (see Section 3.2.12.4), must also be performed. These periodic diagnostic operations will occur during this second half of the daily activities, with care taken to ensure that these periodic changes in operations do not cause a change in the consistent daily solar exposure on the prism. A summary of the normal SIM operations experiments are provided in Table 7 and the configuration of the instrument during these experiments is provided in

Table 8.

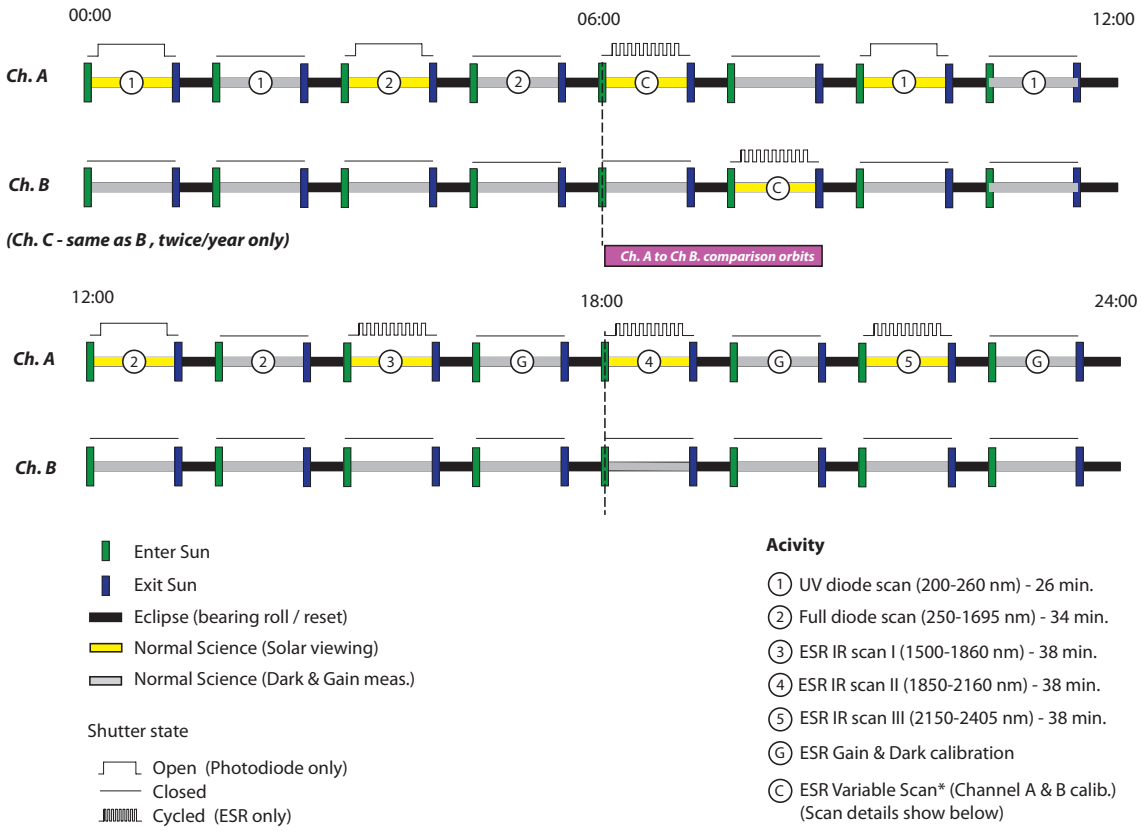

Figure 22: SIM 24 hour timeline of observations and calibrations.

Table 7: Summary of SIM experiments during normal operations.

ESR Mode	Experiment is executed during precision solar tracking. The shutter cycles with a period of 30-200 seconds (selectable depending on wavelength region of interest) and data is read from ESR at 50 Hz. The prism steps through 12 spectral regions across the full spectrum. The prism steps when the shutter is in the closed position. The experiment will be performed with both the primary and the two redundant SIM channels on a well-defined schedule based on the exposure time of the primary channel. Common wavelength regions between the SIM channels will be cycled through during adjacent orbits over the course of several days.
Photodiode Scan	Experiment is executed during precision solar tracking. Data are read from the focal plane photodiode diodes. Prism scans over the selected wavelength range at a selectable step size, step count, and step duration with the shutter in the open position. Prior to the start of the scan, the shutter will be closed to acquire the dark current of the photodiodes. The photodiode scan is repeated on the adjacent orbit with the shutter in the closed position to acquire the full scan dark current measurement.
IR Scan	Experiment is executed during precision solar tracking. Data are read from the ESR (shuttered with a period of 30-100 seconds) at 50 Hz. Prism scans over a subset of wavelengths ranging

	from 1.5 to 2.4 microns. Acquisition of this infrared spectrum will be done on a daily basis and will require 3 orbits to complete.
Standby	This is the standard configuration the instrument will assume when in solar eclipse. Power to the prism drive is turned off.

Table 8 summarizes the daily activities by name, primary detector for that scan, the prism position at the start of the scan and the pixel step size, which defines the difference between two consecutive prism positions. Also provided is the time length of the prism dwell at each prism position, the PDAR (the rate at which photodiode data is taken), the integration time, and shutter position. Subsections 3.2.12.3.1-3.2.12.3.3 provide more detail on the individual daily operations listed in the following Table 8.

Table 8: SIM instrument configuration during nominal daily operations experiments.

	ESR MODE	**Photodiode SCAN**	**IR SCAN**	**STANDBY**
Data Priority	*ESR*	*Photodiodes*	*ESR*	*Photodiodes*
Prism Position	*12 Spectral regions over the spectral range 240-2400nm*	*Scan over full range 200-1695nm*	*Selected wavelengths 1500-2405nm*	*n/a*
Prism Step Count	*variable (determined for wavelength range)*	*754 (UV scan) 985 (UV, Vis, IR)*	*138*	*n/a*
Half Cycle Time (sec)	*15-100 seconds*	*n/a*	*25-100 seconds*	*n/a*
Scan Start	*variable (selected for wavelength)*	*Determined from calibration*	*Determined from calibration*	*n/a*
Prism Step Size	*46*	*38*	*38*	*n/a*
Prism Dwell Time (sec)	*40-200*	*2*	*50-200 seconds*	*n/a*
PDAR	*n/a*	*2*	*n/a*	
Experiment Duration (per orbit)	*~38 min*	*~30 min*	*~38 min*	*eclipse period*
Experiment Frequency	*1 per day*	*4 per day*	*3 per day*	*1 per orbit*
CCD State	*on*	*on*	*on*	*standby*

3.2.12.3.1 UV Diode Scan (200-260 nm)

The UV diode scan covering 200-260 nm will be performed twice per day, roughly twelve hours apart, on orbits 1 & 7. Figure 23 shows a sample spectrum of measured UV diode output voltage for an integration time of 1.5 seconds, and a Photodiode acquisition response (PDAR, see Section 3.2.11.2) of 2 seconds versus subpixel, or wavelength. This figure expands on the summarized information provided in Table 7 and

Table 8. Dark measurements, obtained with the shutter closed at the start and end of the scan, are used to characterize the thermal background of the instrument such as implemented for the SORCE SIM. During

commissioning of the TSIS SIM, while the instrument vacuum door is closed, the dark signal will be monitored throughout the entire orbit for temperature effects, for each photodiode. A total scan time is determined by multiplying the total steps by the PDAR cycle time and adding on the time taking dark measurements.

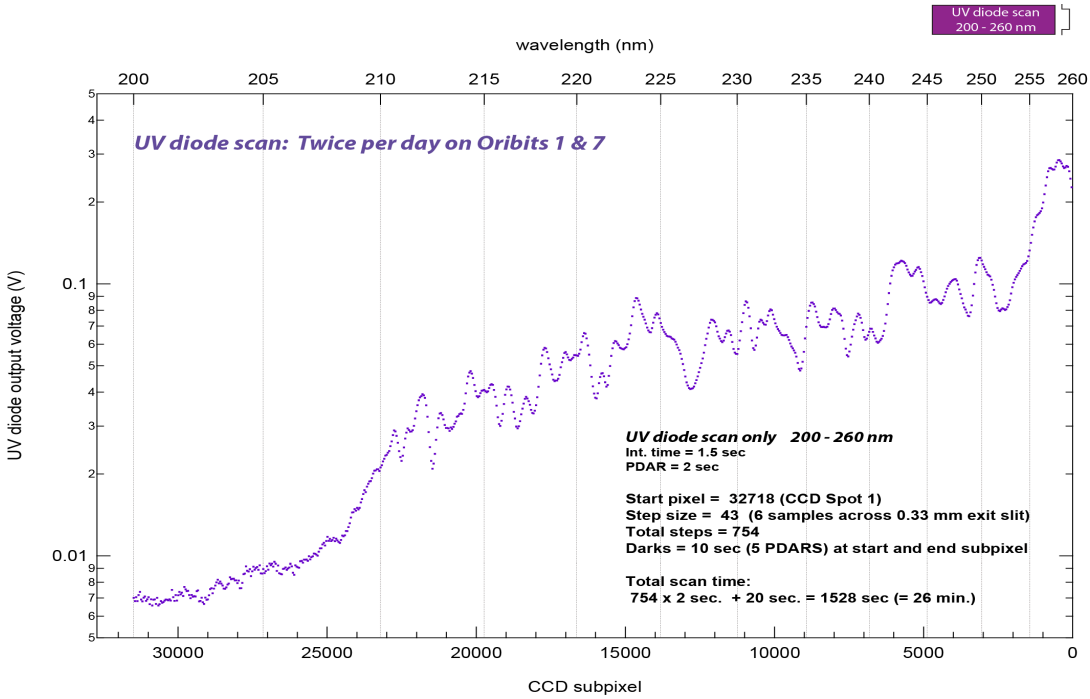

Figure 23: Output voltage versus CCD subpixel (or wavelength) for the SIM UV diode scan.

3.2.12.3.2 Full Diode Scan (250-1695 nm)

The full diode scan covering 250-1695 nm will be performed twice per day, roughly twelve hours apart, on orbits 3 & 9. Figure 24 shows a sample spectrum of measured UV diode output voltage for an integration time of 0.5 seconds, and a Photodiode acquisition response (PDAR, see Section 3.2.11.2) of 2 seconds versus subpixel, or wavelength. This figure expands on the summarized information provided in Table 7 and

Table 8. Note that the peak signals are expected to be around 7-10 Volts. A decreased integration time is achievable because measured voltages are 1-2 orders of magnitude greater at these wavelengths than those measured during the UV diode scan. To prevent saturation of the UV photodiode during measurements taken at visible and near-IR wavelengths, the UV diode integration time is set very short (500 nanoseconds). Note that integration times can be set independently for individual diodes.

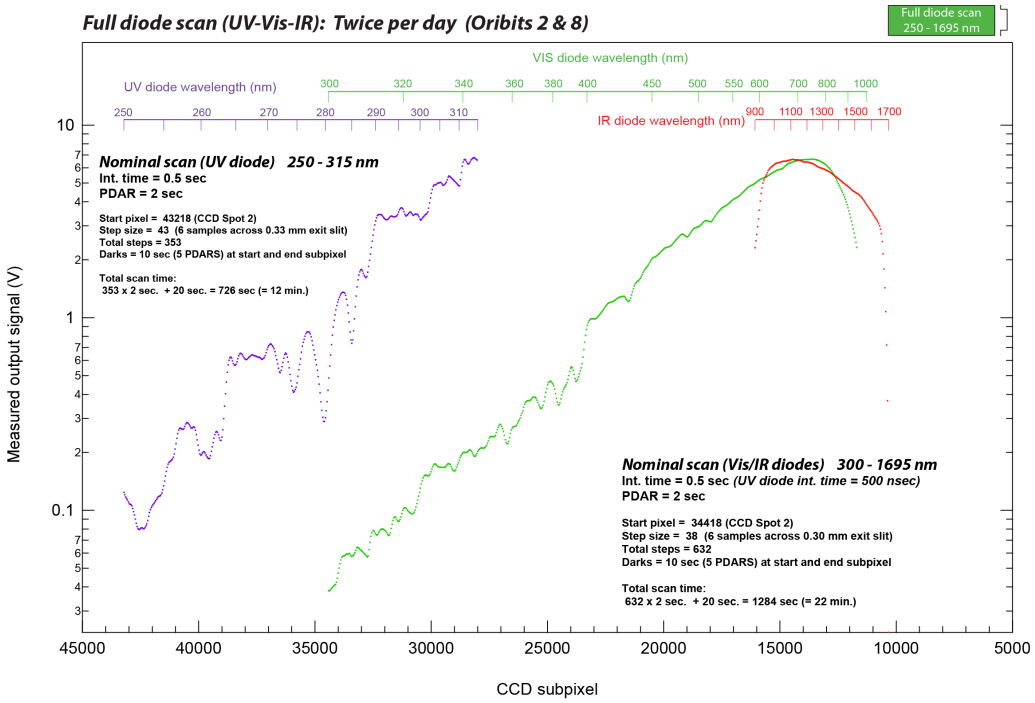

Figure 24: Output voltage versus CCD subpixel (or wavelength) for SIM full diode scan: The UV photodiode is shown in purple, visible photodiode shown in green, and near-IR photodiode shown in red.

3.2.12.3.3 ESR Activity Summary

The ESR (absolute detector) serves two purposes:

1. Measure the near-infrared solar spectral irradiance from 1650 to 2400 nm because there is no photodiode detector measuring for this region,
2. Calibrate the radiant sensitivity (Amp/Watt) of the ultraviolet, visible, and near-infrared photodiodes between 200 and 1650 nm.

3.2.12.3.3.1 ESR Near-Infrared Scan

It takes three full orbits (orbits 11, 13, and 15) to measure from 1500 nm to 2400 nm with the ESR (Figure 25) with a 50% duty cycle on the shutter, a prism dwell time of 50 seconds, and a spectral sampling of 4 samples per exit slit width. A small amount of spectral overlap from orbit to orbit is included.

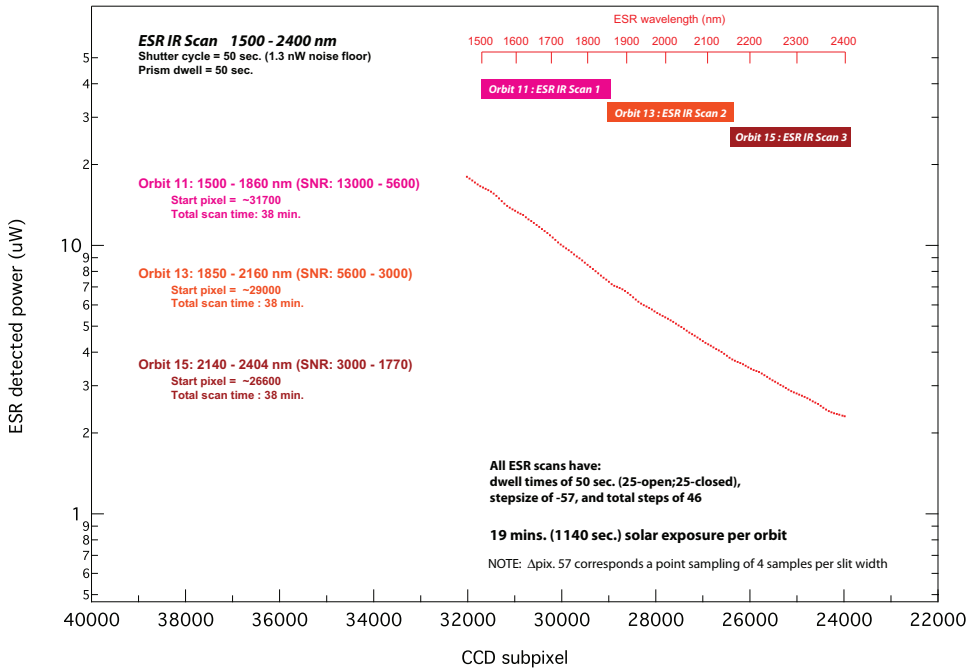

Figure 25: Detected power versus SIM CCD subpixel (or wavelength) for SIM ESR: Shown are the near-infrared scan (1500-2400 nm; red).

3.2.12.3.3.2 ESR Photodiode Calibration (UV through Near-Infrared)

Every day (on orbit 3, see Table 7) inter-channel comparisons between the ESR and photodiodes will be made to calibrate the photodiodes. The inter-channel comparison, for the same spectral range but on SIM channel B occurs on the next consecutive orbit. During these comparisons, ESR measurements are made with the shutter cycling at a 50% duty cycle. Since the degradation in the photodiode responsivity is expected to be a smooth function of wavelength, it is sufficient to calibrate a small (~15) number of distinct wavelength regions instead of the entire spectral range (see Section 7.2).

Figure 26 shows the sample spectrum of measured ESR power versus subpixel, or wavelength for the UV range. Due to the small, detected powers at these wavelengths, the signal-to-noise ratios are around 100 at 240 nm and longer prism dwell times (80-140 seconds) are required to reduce ESR measurement noise. Spectral sampling is 5 per exit slit width.

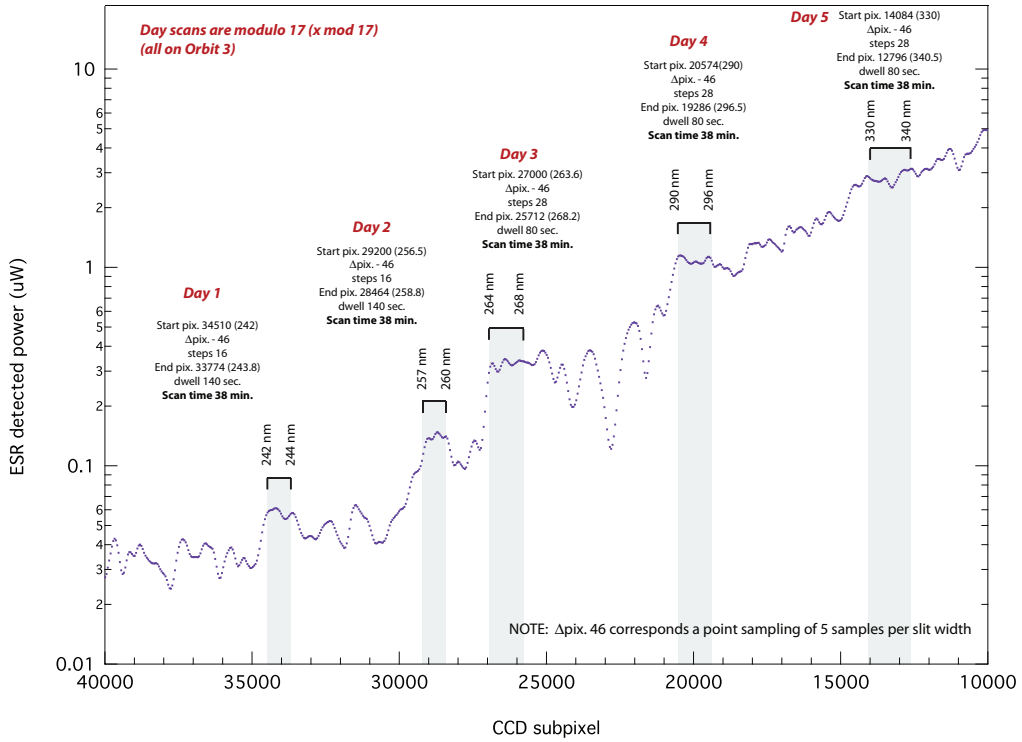

Figure 26: Detected ESR power versus CCD subpixel (or wavelength) in the ultraviolet: The wavelength range of five SIM ESR-photodiode calibration scans performed over five days is indicated.

ESR-photodiode calibrations are also made across the visible to the near-infrared (Figure 27) for 7 overlapping spectral segments. For these scans, the shutter duty cycle is 50%, prism dwell times are 40 seconds, and 5 spectral samples per exit slit width are obtained. The signal-to-noise (SNR) ratios for these spectral bands range from 6500 to 19000. The decreased integration times occur because measured voltages are 1-2 orders of magnitude greater at these wavelengths than those measured during the UV diode scan. To prevent saturation of the UV photodiode during measurements taken at visible and near-IR wavelengths, the UV diode integration time is set very short (500 nanoseconds). Approximately every two weeks, one of the calibrations obtained will span the spectral range 745-1032 nm where the radiant sensitivity of the visible and infrared photodiodes deviate from the line of 100% quantum efficiency leading to greater uncertainty in the photodiode measurements.

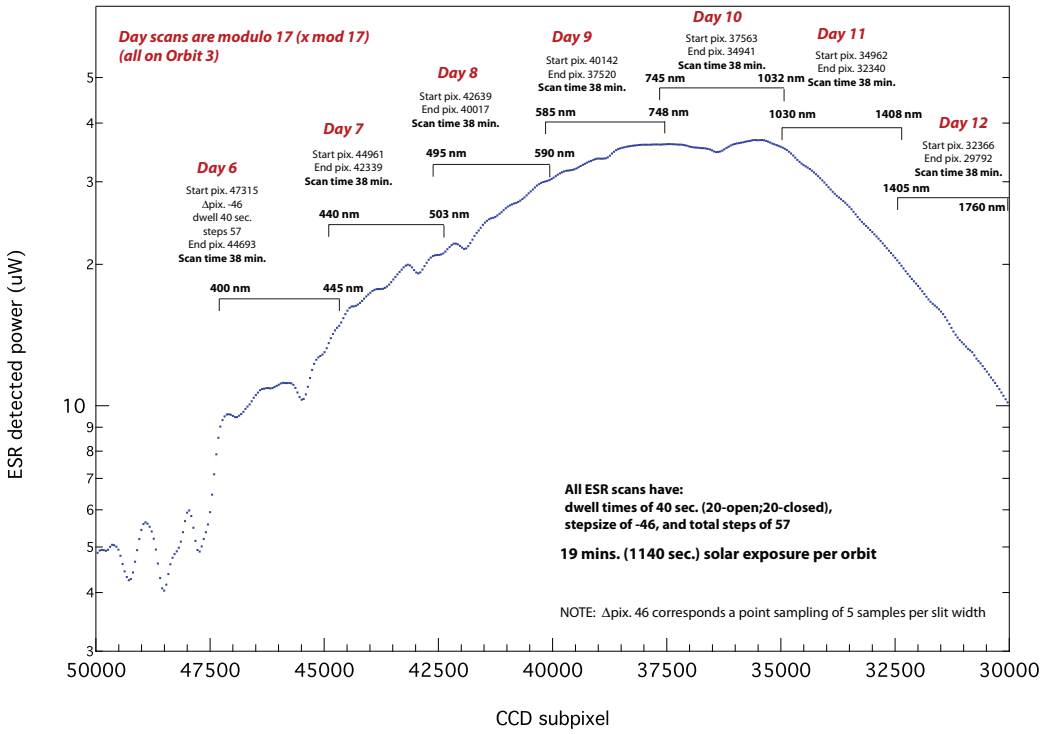

Figure 27: Detected ESR power versus CCD subpixel (or wavelength) in the visible though near-infraed: The wavelength range of seven SIM ESR-photodiode calibration scans performed over seven days is indicated.

3.2.12.4 Diagnostic Operations

Periodic diagnostic operations will be performed. These periodic diagnostic operations establish accurate knowledge of angular offsets between the optical bore sight and the TPS pointing sensors, with care taken to ensure that these periodic changes in operations result in the same daily solar exposure on the prism. These diagnostic operations are summarized in Table 9 with the corresponding instrument configuration described in Table 10. The TSIS Instrument Operations Document (ref. in Table 1) provides more details.

Table 9: Summary of SIM Instrument Calibrations

Solar Alignment	This observation is performed no more than once per month. Typical observation mode will be fixed wavelength with the shutter open. One prism position is selected and remains the same throughout the mission. Additional wavelengths will be selected as appropriate. Typically, not more than one orbit per month is dedicated to solar alignments. Depending on the duration of the sunlight side of the orbit, 2 to 4 maneuvers may be executed. If more then one wavelength is selected, they will be performed in subsequent orbits or maneuvers.
Fixed Wavelength	Experiment is executed during precision solar tracking. The prism is fixed at the desired wavelength position for the duration of the experiment. Data from the ESR and focal plane diodes are sampled during this experiment. Can be performed with either or both primary and redundant SIM channels operating. Usage of this mode will be limited to prevent unnecessary exposure of the prisms.
Servo Gain Calibration	Performed three times per week at night using SIM A, and will be done on a monthly cadence for B and C. Shutter is closed, as this is a non-optical calibration. The experiment is conducted for a period of 10 minutes.
Inter-channel comparison	Measures changes in the performance of the SIM A; the channel used for daily measurements. The three science experiments listed in Table 7 (ESR Mode, Photodiode Scan, IR Scan) will be performed on adjacent orbits for SIM B and (less frequently) SIM C. Timing for the SIM B and SIM C channels is based on the amount of exposure time of the SIM A working channel. Exposure time is tracked in data processing. Tentatively, SIM B will be operated one orbit per day (Orbit 3) scanning common wavelength regions that repeat every 17 days (this includes 5 UV regions and 7 Vis-IR regions, with 3

	IR only scans and 2 photodiode scans). SIM C will be operated same as B with 17 scans over 17 days, but only twice per year (nominally, on the Vernal & Autumnal Equinox - 3/20 & 9/22 - to ensure common 1-AU and FOV conditions). Based on this measurement cadence, SIM A will acquire 196 minutes of solar exposure per day whereas SIM B will be at 19 min per day (~10% exposure duty-cycle). SIM C will only acquire ~650 minutes per year (~10% exposure of SIM B).
CCD Dump	This mode will be conducted once during the early orbit campaign. The frequency for this mode will be determined once in flight. Possibly once every three months. All SIM operations will be halted during this mode.
Image Light/ Image Dark	This mode is used to measure degradation in the CCD channel. The CCD is equipped with a electronic shutter, so accumulation of data from these experiments is used to adjust the integration time to maintain an approximately constant light intensity of light on CCD. Image light is performed during precision solar tracking at three fixed positions along the CCD, Image Dark is performed during eclipse without prism drive positioning.

Table 10: SIM instrument configurations during calibration experiments.

	SOLAR ALIGNMENT	**SERVO GAIN**	**FIXED WAVE-LENGTH**	**CCD DUMPS**	**A/B/C DUTY CYCLE**	**Image Light / Image Dark**
ESR Data Sampling	*on*	*on*	*on*	*off*	*on*	*Off*
Focal Plane Diode Data Sampling	*on*	*on*	*on*	*off*	*on*	*Off*
Shutter Position	*open*	*closed*	*open*	*closed*	*mode dependent*	*closed*
Prism Position	*fixed selectable wavelength operated in open loop mode*	*n/a*	*selectable fixed wavelength*	*n/a*	*mode dependent*	*Img Lght fixed,3 positions img Drk n/a*
Prism Step Size	*0*	*n/a*	*0*	*n/a*	*mode dependent*	*n/a*
Prism Step Count	*n/a*	*n/a*	*n/a*	*selectable*	*mode dependent*	*n/a*
Scan Start	*fixed*	*n/a*	*fixed*	*selectable*	*mode dependent*	*n/a*
Half Cycle Time (sec)	*0*	*50 feedforward value =16000*	*0*	*n/a*	*mode dependent*	*n/a*
Prism Dwell Time (sec)	*65535*	*600*	*65535*	*n/a*	*mode dependent*	*420*
Experiment Duration	*1 solar period*	*30 minute period conducted during eclipse*	*1 solar period*	*during daylight part of orbit*	*2 orbits*	*7 minutes*
Experiment Frequency	*variable*	*3 per week*	*variable*	*1 per month*	*daily B and every 6 months C*	*Img lght 3/week, Img Drk 1/week*

4 Algorithm Description

4.1 Physics of the Problem

The total solar irradiance, E_0, is the radiant flux density at the top of the atmosphere, and is defined mathematically as:

$$E_0 = \frac{P}{A} \tag{4.1.1}$$

where P is the total incident photon power and A is an element of area. The high absorptivity of the TIM ESRs ensures collection of nearly all the entering sunlight across the entire solar spectrum. The SI units of total irradiance are W/m^2.

Likewise, the spectral irradiance, E_λ, is the radiant flux per unit area, but at wavelength λ_S per unit wavelength interval, $\Delta\lambda$; and defined mathematically as:

$$E_\lambda\left(\lambda_s\right) = \frac{P_D\left(\lambda_s\right)}{A\Delta\lambda} \tag{4.1.2}$$

where $P_D(\lambda_S)$ is the element of incident flux within the spectral bandpass ($\Delta\lambda$) and A is an element of area. The SI units of spectral irradiance are W/m^3, although alternate units may also be used (e.g., W/m^2/nm).

Considering the TIM and SIM instrument capabilities given in Table 2 and Table 5, as solar radiation falls on one of the TSIS instruments, the aperture (precision aperture for TIM and precision entrance slit for SIM) defines the area element, A, of Equations 4.1.1 and 4.1.2. For SIM, the element of wavelength, $\Delta\lambda$, is established from the width of the exit slit with appropriate dispersive relationships derived for the prisms. In addition, as the photons encounter the entrance slit and prism there are loss terms for each that must be accounted for— absorptivity efficiency of the ESR and correction for diffraction effects in Equation 4.1.1 and diffraction of light off the entrance slit, prism transmissions, and ESR detector efficiency in Equation 4.1.2. Section 5 provides details of the characterization and calibration of the TIM and SIM instruments.

4.2 Conversion from Instrument Signal to Irradiance

There are two similar, yet distinct algorithms to convert from instrument signal to incident solar radiation – one for TIM and one for SIM. Each algorithm is tailored for the specific optical elements and detectors of that instrument. Yet, each algorithm utilizes a fundamentally similar measurement equation, and common correction terms. Common corrections are described in Section 4.2.3 and include Doppler ($f_{Doppler}$) and solar distance (f_{AU}) corrections used to report irradiances for a non-moving observer at 1 AU from the Sun and field of view corrections (f_{FOV}) to correct for the sensitivity of the instruments to incidence angle.

Equations 4.1.1 and 4.1.2 have three terms, which represent the incident radiant photon power (P), entrance aperture area (A), and spectral bandpass ($\Delta\lambda$) over which the energy is distributed.

4.2.1 TIM Measurement Equation

Equation 4.1.1 has two terms, which represent the incident radiant photon power (P), and precision entrance aperture area (A) over which the incoming radiant energy is distributed. What is not captured in Equation 4.1.1, is the tailoring required for the specific detectors of the TIM instrument, nor the required correction terms, such as Doppler shift and field-of-view corrections, that relate the corrected solar irradiance E_0 to the (Fourier Transformed) Data Numbers ($\boldsymbol{D}$) observed by the instrument [*Kopp and Lawrence*, 2005].

The TIM measurement equation follows from the signal flow diagram shown in Figure 28 [from *Kopp and Lawrence*, 2005]. Scalars represent the input irradiance time series E_0, aperture area A, cavity absorptance α, standard voltage V, standard resistance R, and a time series of output data numbers D. The bold-type terms are complex phasor components

representing the amplitude and phase of sinusoidal variations as a function of frequency for the shutter transmission ***S***, thermal impedances ***Z***, and servo gain ***–G*** within the instrument.

In ground processing, phase-sensitive detection (Section 4.3.1) is used to frequency analyze the times series of output data numbers *D* and smooth them using a boxcar filter at the shutter frequency. This method of ground processing produces the complex phasor ***D*** that gives knowledge of the changes that occur in-phase with the shutter. The shutter fundamental is 0.01 Hz, and the TIM data are output at rates up to 100 Hz, providing a maximum of 10^4 numbers per shutter cycle.

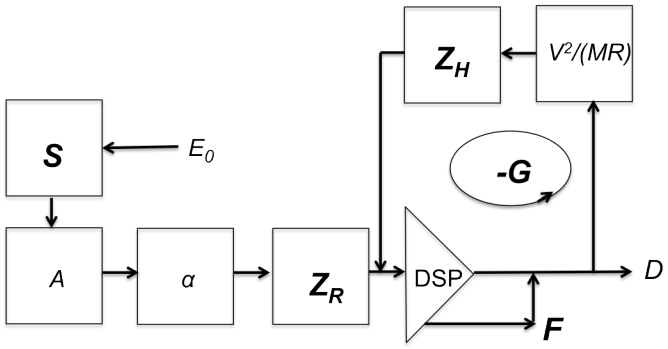

Figure 28: Signal flow diagram for the TIM instrument: Variables in boxes are out/in ratios at some frequency. The servo loop gain is ***–G***. The digital signal processor (DSP) adds a known feedforward signal ***F***. The ratio of thermal impedances Z_H/Z_R is the equivalence ratio. Bold symbols represent complex phasors. Reproduced from *Kopp and Lawrence* [2005].

The equation to convert the phasors ***D*** to measured irradiances [from *Kopp and Lawrence*, 2005] is given in Equation 4.2.1.1.

$$E_{meas} = \frac{V^2}{MR} \cdot \frac{1}{\alpha A f_{corr}} \cdot real\left[-\frac{\boldsymbol{Z_H}}{\boldsymbol{Z_R}} \cdot \frac{1}{\boldsymbol{S}} \cdot \left(\boldsymbol{D} + \frac{\boldsymbol{D-F}}{\boldsymbol{G}} \right) \right] \qquad (4.2.1.1)$$

Variables not already defined include the ratio of thermal impedances, $\boldsymbol{Z_H / Z_R}$, known as the equivalence ratio that accounts for differences in electrical heater replacement power and absorbed radiant power (i.e. the Kelvin/Watt relationship), and the applied feedforward values ***F***. *M* is a fixed scalar value equal to 64000 that converts data numbers, *D,* to duty cycle, $q = D / M$. There are four correction factors combined in f_{corr} that account for the spacecraft's distance to the Sun, Doppler shifts due to spacecraft velocity, pointing effects, and cavity responsivity degradation. The first three correction factors are common to both TIM and SIM and discussed in Section 4.2.3. Expanded discussions of the variables are provided in *Kopp and Lawrence* [2005] and TIM Instrument Design [Section 3.1]. The ground and flight calibrations of all terms is discussed in Section 5. Monitoring and correction for the degradation of the instrument response due to solar exposure is discussed in Section 6.

The instrument's thermal background contributes to the measured signal E_{meas}. Observations from four temperature monitors on the instrument during the orbital eclipse periods are used in an empirical model to estimate the thermal background [*Kopp and Lawrence*, 2005]. The reported TSI value is the difference between the measured signal and the estimate of the thermal background, as shown in equation 4.2.1.2.

$$E_0(t) = E_{meas}(t) - E_{dark\_est}(t) \qquad (4.2.1.2)$$

Combining equations 4.2.1.1 and 4.2.1.2 results in the full TIM measurement equation that converts the phasors $\boldsymbol{D_{Sun}}$ (i.e. the phase-sensitive filtered values from observations of the Sun) and $\boldsymbol{D_{Dark}}$ (i.e. the phase-sensitive filtered values from observations of dark space) to the reported TSI value, E_0. The phase-sensitive transformed feed-forward data numbers commanded for Sun observations $\boldsymbol{F_{Sun}}$ and for dark space $\boldsymbol{F_{Dark}}$, need only be transformed once on the ground. The observational values $\boldsymbol{D_{Sun}}$ and $\boldsymbol{D_{Dark}}$ need to be transformed as a time series. As flown values for

uncertainties of the terms in the measurement equation will ultimately be made available to the TSIS project after in-flight calibration is completed.

$$E_0 = \frac{V^2}{MR} \cdot \frac{1}{\alpha A f_{corr}} \cdot real\left[-\frac{\boldsymbol{Z_H}}{\boldsymbol{Z_R}} \cdot \frac{1}{\boldsymbol{S}} \cdot \left(\boldsymbol{D_{Sun}} - \boldsymbol{D_{Dark}} \right) \cdot \left(1 + \frac{1}{\boldsymbol{G}} \right) + \frac{\left(\boldsymbol{F_{Sun}} - \boldsymbol{F_{Dark}} \right)}{\boldsymbol{G}} \right] \qquad (4.2.1.3)$$

4.2.1.1 Definition of terms

Here, we provide definitions and brief descriptions for the terms in the TIM measurement equation (Equation 4.2.1.3). Sections 5.1 and 5.2 provide detailed information about the characterization and calibration of parameters that fold into these terms.

DAC Calibration Factor - $V^2/(MR)$: The data numbers produced by the servo system are converted by a precision duty-cycle type Digital-to-Analog Converter (DAC) to the replacement power. The changes in the substituted electrical power are proportional to the duty cycle and the V^2/R power, corrected for the lead resistances. V is the value of the precision, buffered, standard voltage. M≡64000 is the full scale (100% duty cycle) count. R is the effective heater resistance at the regulated operating temperature.

Data Numbers – D: Data numbers $\boldsymbol{D}$ in bold are the phase-fundamental-filtered values (Section 4.3) from observations of the Sun ($\boldsymbol{D_{Sun}}$) and from observations of dark space ($\boldsymbol{D_{Dark}}$).

Shutter Waveform Factor – S: A complex phasor that characterizes the non-unity transmission when the shutter transitions from open to closed position.

Entrance Aperture – A: The effective aperture area.

Bolometer Absorptance - α: The cavity absorption is equal to one less the cavity reflection at the center of the pointing field of view and is averaged over the solar spectrum.

Equivalence Ratio - $\boldsymbol{Z_H/Z_R}$: The equivalence ratio is a measure of the change in electrical power that gives precisely the same cone temperature as that provided by the incident sunlight.

Servo Loop Gain – $\boldsymbol{G}$: The servo open-loop gain is the end-to-end complex gain of the control loop at the shutter fundamental.

4.2.2 SIM Measurement Equation

SIM is a solar spectral irradiance radiometer designed to measure the full disk solar spectral irradiance from 200 nm to 2400 nm. The solar spectral irradiance, $E(\lambda)$ has units of W m^{-2} nm^{-1} and is represented by Equation 4.1.2. The incoming solar radiation first passes through a NIST-calibrated aperture (i.e. entrance slit) of area, A (units mm^2) converting the spectral irradiance into spectral power. What is not captured in Equation 4.1.2 are the wavelength (λ) and polarization (p) dependent losses that occur as the solar radiation passes though the full optical path of the prism and eventually onto each detector.

The two primary losses are diffraction, $D(\lambda)$, and prism transmission, $T(\lambda,p)$. To a lesser degree, prism surface scattered light ($< 10^{-5}$), and stray light are also sources of lost light (Table 28).

The wavelength- and polarization-dependent spectral power, P (units of W nm^{-1}), which reaches the focal plane is

$$\frac{P}{\lambda} = E(\lambda)\cdot A\cdot D(\lambda)\cdot T(\lambda,p) \qquad (4.2.2.1)$$

All of the polarization dependence is in the prism transmission due to the Fresnel reflection and transmission coefficients (Section 3.2.9.2 and the SIM Irradiance Algorithms document referenced in Table 1) associated with the incidence angle of the prism. Even though incident solar radiation is unpolarized, the calibration of the prism involves highly polarized lasers and both polarization modes (parallel or perpendicular to the plane of incidence) are tracked during calibration studies. There are diffraction and polarization dependencies in the pointing and field-of-view corrections that are quantified though analysis and verified with calibration.

A given detector collects only a fraction of the incoming spectral power. For a given wavelength, the prism angle is defined such that the chief ray for that wavelength is centered on the exit slit. The transmitted radiation reaching the focal plane will occupy a range of focal-plane subpixels across the full width of the exit slit. This is known as the instrument slit function, and it describes the relative slit intensity per subpixel, $I_s(\lambda,c)$, such that

$$\int I_s(\lambda,c)dc = 1 \qquad (4.2.2.2)$$

where c is the CCD subpixel defining the prism incidence angle. Since there is a one-to-one correspondence between subpixel and prism incidence angle (Section 3.2.3), there is a one-to-one relationship between subpixel and wavelength (Section 3.2.4) due to the wavelength refraction dependence on incidence angle. This pixel-to-wavelength relationship is nonlinear. However, over the narrow width of the exit slit, the dispersion is essentially linear with subpixel (Section 3.2.9.1). Also contained within $I_s(\lambda,c)$ is the wavelength-dependent responsivity of the detector, which for the photodiode detectors is the radiant sensitivity, $R(\lambda,T)$ (units of Amps W^{-1}), and for the ESR bolometer is the spectral absorptance, $\alpha(\lambda)$ (unitless).

The complete spectral profile integral, including all wavelength dependent factors, affecting the spectral transmission and bandpass is then defined as the following, where c_s defines the selected subpixel.

$$\int D(\lambda)\cdot T(\lambda,p)\cdot I_s(\lambda,c_s)d\lambda \qquad (4.2.2.3)$$

The relative spectral response function is indirectly determined by fixing the calibration laser, in wavelength and intensity, and then scanning the subpixels over the non-zero response regions (Sections 5.3.1.7 and 5.3.2). The total power passing through the exit slit requires integrating the spectral power per subpixel across the full width of the exit slit in subpixel coordinates. To accomplish this, an exit slit image mask, $M(c)$, is defined as unity within the subpixel limits of the exit slit and zero outside of the limits. Equation 4.3.2.4 represents the total power (in Watts) collected by the detector.

$$P = \int\int E(\lambda')\cdot A\cdot D(\lambda')\cdot T(\lambda',p)\cdot I_s(\lambda',c')\cdot M(c-c')d\lambda' dc' \qquad (4.2.2.4)$$

We now consider the detector response and gain, G, to optical power and to convert into data numbers ($DN\,W^{-1}$). The gain is a function of many factors including wavelength (λ), polarization (p), temperature (T), pointing (θ,ϕ), field-of-view (β_{FOV}), and in the case of the ESR, the shutter frequency. For a given detector, we separately account for all these contributions to the gain, but for simplification purposes here, we consider the gain as a wavelength and polarization dependent average over external correction factors, namely $G(\lambda,p,T,[\theta,\phi],\beta_{FOV}) = \bar{G}(\lambda,p)$. The measured DN's can then be expressed as

$$DN(c) = \int\int E(\lambda')\cdot A\cdot D(\lambda')\cdot T(\lambda',p)\cdot \overline{G}(\lambda',p)\cdot I_s(\lambda',c')\cdot M(c-c')d\lambda' dc' \qquad (4.2.2.5)$$

The SIM measurement equation can be simplified and ultimately, represented as following:

$$\int E(\lambda')\cdot\sigma(\lambda',c)d\lambda' \approx \frac{DN(c)}{A\cdot D(\lambda(c))\cdot T(\lambda(c),p)\cdot\overline{G}(\lambda(c),p)\int M(c)dc} \qquad (4.2.2.6)$$

4.2.2.1 Definition of Terms

Here, we provide definitions and brief descriptions for the terms in the SIM measurement equation (Equation 4.2.2.6). Sections 5.3 and 5.4 provide detailed information about the characterization and calibration of parameters that fold into these terms.

Entrance Aperture – *A*: The effective entrance aperture area.

Diffraction – *D*: Diffraction at the entrance slit deflects a fraction of the incoming energy outside of the acceptance angle of the prism and will result in a decrease in the full path transmission. This diffraction is dependent on wavelength, detector, and instrument pointing.

Transmission – *T*: The transmission of the prism, which disperses the light beam on to the instrument focal plane, and is the sole dispersive element in TSIS SIM.

Gain – *G*: The servo open-loop gain is the end-to-end complex gain of the control loop at the shutter fundamental.

Exit Slit Mask – *M*: An exit slit mask, defined as unity within the subpixel limits of the exit slit and zero outside of the limits, is used in determining the relative spectral response.

Spectral response function – σ: The resolution of the instrument.

4.2.3 Corrections Common to Both Instruments

4.2.3.1 Solar Distance Correction

The total solar irradiance and the spectral irradiances are to be reported as seen from a distance of one astronomical unit (AU) from the center of the Sun, and at zero line of sight velocity *v* with respect to the Sun. The measured irradiance varies inversely with the square of the distance between the instrument and the center of the Sun. We define an inverse square correction factor f_{AU} to 1 AU:

$$f_{AU} = \left(\frac{R_{AU}}{R_{Sun}}\right)^2 \qquad (4.2.3.1.1)$$

where R_{AU} is one astronomical unit and R_{Sun} is the distance between the instrument and the center of the Sun. The factor f_{AU} appears in the denominator of the measurement equations and varies about ±3.4% annually.

4.2.3.2 Velocity (Doppler) Correction

The line of sight velocity v_{los} toward the Sun is the rate of change in the R_{Sun} distance. There are four effects on the irradiance. The observable effects are first order in the ratio of line of sight velocity to the speed of light, *c*. We define

the first order Doppler parameter. The *relativistic* terms are of order β^2. When we approach the Sun, β is negative and:

a) The incoming photons have more energy by a factor (1-β).

b) The instrument collects photons at a rate larger by a factor (1-β).

c) The wavelength intervals $\Delta\lambda$ of the incoming spectra are decreased by a factor (1-β).

d) The wavelengths λ of each spectral feature are decreased by a factor (1-β).

We define a generic Doppler correction factor

$$f_{Doppler} \equiv (1-\beta) \equiv 1 - \frac{v_{los}}{c} \qquad (4.2.3.2.1)$$

The total solar irradiance as measured by TIM is then corrected by the factors a) and b) to be:

$$E_0 = \frac{E_{Observed}}{f_{Doppler}^2} \qquad (4.2.3.2.2)$$

The spectral irradiances per *wavelength* for SIM are corrected by the factors a-c to be:

$$E_{\lambda 0} = \frac{E_{\lambda Observed}}{f_{Doppler}^3} \qquad (4.2.3.2.3)$$

The spectral irradiances per *wavenumber v* for SIM are corrected by the factors a-c to be:

$$E_{v0} = \frac{E_{vObserved}}{f_{Doppler}} \qquad (4.2.3.2.4)$$

The observations are interpolated and stored into standard (zero velocity) spectral bins λ_0 that are different, by effect d), from the instrument wavelength setting.

$$\lambda_0 = \lambda_{Instrument}\, f_{Doppler} \qquad (4.2.3.2.5)$$

The Earth's distance to the Sun and the velocity of the Earth relative to the Sun are both obtained from the "VSOP87" harmonic series "B solution" in heliocentric spherical coordinates [*Bretagnon & Francou*, 1988] based on the JPL Dynamic Ephemeris integrations "DE200" [*Standish*, 1982 and *Standish*, 1990]. For both position and velocity, the VSOP87 approximations have uncertainties on the order of 10 parts per billion (ppb).

Telemetry from the International Space Station (ISS) Broadcast Ancillary Data (BAD) data feed from the Huntsville Operations Support Center (HOSC) will be used to derive spacecraft position and velocity relative to the Earth. The ground station data are propagated (i.e. gap-filled and smoothed) and form the basis for a TSIS SPICE kernel. The TSIS kernel and the 'SPICE' planetary ephemeris are used to generate a table of spacecraft position and velocity relative to the Earth. The table will contain the 1 AU and Doppler Correction factors in the same format as previous TIM/SIM data. The ISS telemetry will be in the Level 1A telemetry table.

'SPICE' is a NASA ancillary information system that provides the capability to incorporate space geometry in planning and interpreting observations from space-borne instruments (https://naif.jpl.nasa.gov/naif/spiceconcept.html).

4.2.3.3 Field of View Correction

The sensitivity of TSIS TIM depends on the location of the Sun within the instrument field of view (FOV), given by pointing angles θ and ϕ. The field of view factor $f_{FOV}(\theta,\phi)$ included in the overall correction factor, *fcorr,* in the denominator of the measurement equation (Section 4.2) is equal to one on axis, and is used to transfer the on-axis

characterization to the actual solar position within the FOV. Although we characterize the variation of response versus the pointing angles in pre-launch tests, the most accurate data come from the periodic cruciform and raster scans in flight. Since the pointing precision of the TSIS Thermal pointing System is sub-arc minute and the basic noise of TIM is < 1 ppm, we expect that the empirical method will add little uncertainty to the measurements.

For TIM and SIM, the sensitivity to pointing effects is actually in the cavity absorptance (α), equivalence ratio ($\boldsymbol{Z_H/Z_R}$), and the cosine-theta aperture factor. These individual effects are accounted for by the single correction factor $f_{FOV}(\theta,\phi)$. However, as discussed in Section 3.2.12.4, the precision of the TSIS SIM instrument is at a level where changes in cavity absorbtance and equivalence ratio with variations in solar pointing are undetectable from the noise and the SIM will perform nominal daily operations during the periodic raster scans. However, the periodic cruciform scans will monitor and correct for changes in cosine-theta aperture effects in the TSIS SIM data.

4.3 Phase-Sensitive Detection

Phase-sensitive detection is applied in post-processing and is designed to analyze the TIM and SIM ESR signals at a frequency that is least responsive to instrument thermal or electronic noise and lessens sensitivity to high frequency ringing "overshoots". For SORCE, the phase-sensitive detection was identically applied to the TIM and SIM instruments. However, for the TSIS SIM, modifications have been made to lessen the number of shutter open-shut cycles required for determining a background noise subtraction in order to improve the processing speed of the spectral measurements without compromising the accuracy of the data product. The process and differences between the TIM and SIM phase-sensitive detection are described below.

In normal operation mode, the shutter for a TIM and SIM ESR is cycled 50% open and 50% closed with a 100-second period throughout the orbit. We analyze only the variations in electrical replacement heater power that are in-phase with the shutter at this fundamental frequency. This "phase sensitive detection" suppresses the instrument's susceptibility to the radiative thermal background, as well as to time-varying fluctuations in temperatures, thereby facilitating a non-cooled radiometer with high accuracy and low noise.

4.3.1 Phase Sensitive Detection: TIM instrument

Each cavity, with its thermistor, forms a bolometer to detect incoming radiation (see Section 3.1 for TIM instrument design details). An AC, digital, feedback loop controls bolometer heating via the precision wire-wound resistors at the tip of each cone. The electronics consist of the difference temperature sensing bridge, a bridge error amplifier, precision voltage sources, and a DSP-implemented servo loop for actively balancing the bridge, as shown in Figure 29. The thermistor temperature sensors on each of the two bolometers form two legs of the bridge with the opposing load resistors set to 0.76 of the operating resistance of the thermistors. This bridge configuration stabilizes the bias heating power against ambient temperature changes. Any differential bolometer temperature unbalances the bridge and the resulting error signal is amplified, digitized, demodulated, filtered, and then fed back to the cone heater from a 16-bit pulse width modulator digital-to-power converter. Normal operations are feed-forward and will provide a heater power via ground command that anticipates (to <1%) the shutter position, thereby keeping the cone temperature near constant. Comparing the active bolometer cone to the second reference cone, shielded from light, eliminates sensitivity to common mode thermal variations.

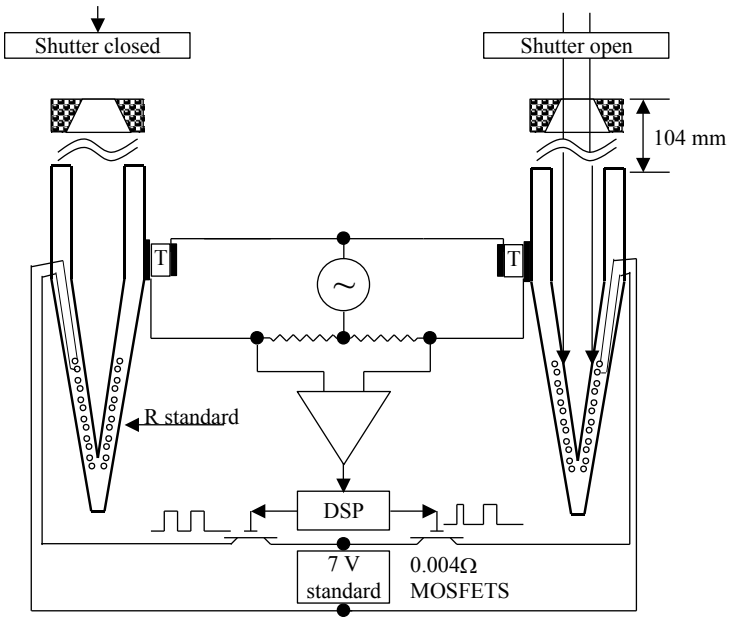

Figure 29: Schematic of the TIM servo system: Thermistors, T, on the cones detect differential temperature changes. The servo system and DSP change the power on one of the cones to keep the temperature constant. The standard voltage is switched through low resistance switches to the standard heater resistances on the cones.

The TIM is a shuttered radiometer with the shutter running with a 0.01 Hz square wave. The output data numbers follow the square wave with changes in the TIM digital-to-power converter's 16-bit unsigned data numbers, DN_I, proportional to changes in the solar irradiance. The cavity temperatures vary only a few mK during a shutter cycle; so system temperature vs. power relations are linear to better than 1 ppm. We thus replace the time dependence of the temperature field and the power flow with a complex Fourier series in harmonics of the shutter fundamental. We then use the in-phase signal at the shutter fundamental to determine the irradiance, requiring characterization of the radiometer to a few ppm at only one frequency and one phase. The advantages of this approach over the traditional time-domain algorithms include:

a) The shutter frequency is selected for minimum system noise.

b) The time convolutions become multiplications of complex numbers, replacing convolutions over time. This allows the instrument to be characterized.

c) We can reject the out-of-phase component, mostly a first-order effect. The in-phase component mostly has effects to second order.

The time series data numbers are subject to a phase sensitive detection on the ground. Phase sensitive detection consists of multiplication of the time varying signal by a local oscillator at the reference frequency, then low pass filtering to remove noise and the harmonics of the reference frequency. The low pass filter that we have chosen is the convolution of four cycle-wide pulses. The incoming time series, DN_I, with N points per cycle, is processed to provide the complex output series $\boldsymbol{DN}_J$ as follows. J is the data index in the complex output series and it runs from 0 to MN-1, where M is the number of cycles and N is the number of points per cycle.

$$\boldsymbol{DN}_J = \frac{2}{N^4} \sum_{M=J-N+1}^{J} \sum_{L=M}^{M+N-1} \sum_{K=L-N+1}^{L} \sum_{I=K}^{K+N-1} e^{i2\pi\, I/N} DN_I \qquad (4.3.1.1)$$

This filter consists of multiplication by the complex sinusoid at the shutter frequency, then low-pass filtering with four repeated box-car running averages. This algorithm, with its normalization, must be applied to all the data numbers

from the replacement heater DAC, and also (as needed) to the shutter waveform. The timing of the center of gravity is left unchanged. The four filters have zero response at the harmonics of the shutter frequency, and the repeat of four is adequate to reject baseline drift. We denote the time series data numbers as DN_I, and the phase-detected data numbers with **bold face** $\boldsymbol{DN_J}$. The transformed data numbers $\boldsymbol{DN_J}$ are highly over-sampled, and can be decimated in the final product.

4.3.2 Phase Sensitive Detection: SIM instrument

The SIM is a dual Féry prism spectrometer. Like the TIM, the primary detector for the SIM is an electrical substitution radiometer (ESR). However, instead of blackened cavity, a diamond strip with NiP black on one side is used because the light levels are so low (dispersion from prism) and a cavity would have entailed too much thermal mass. For normal operation, the channel's shutter is opened and closed with a 100 second period.

The SIM ESR measures the full spectrum of light between 200 and 2400 nm. To perform post-processing phase-sensitive detection in the manner described in Section 4.3.1 for the TIM instrument would require more measurement time than available. The SIM Flight ESR Calibration Document (ref. in Table 1) provides details of quantitative studies on various different smoothing kernel choices, as well as the time period of the data block over which it is applied, was undertaken. Results show that a choice of a Hanning window (a smooth function with the shape of a cosine wave with a 1 added to it so it is always positive) acting over 1.5 shutter cycles (i.e. closed, open, and closed) creates the best solution between maximizing the statistics of the solution while minimizing the time required for each solution. The convolution of the Hanning filter window (Figure 30a) applied to SIM ESR data, shown as an example in Figure 30b for a prism dwell time of 20 seconds, is used to calculate the difference between the DN's measured with and without light present. At the second shutter-closed cycle in the data block, the prism is rotating to the next measurement orientation. This period of shutter-closed data then impacts the phase sensitive calculation for *two* SIM measurements: one at the current prism location and the other at the next prism location as shown in Figure 31. With these specific differences in mind, the computation of the phase-sensitive data number for the SIM instrument is undertaken as described above for the TIM instrument.

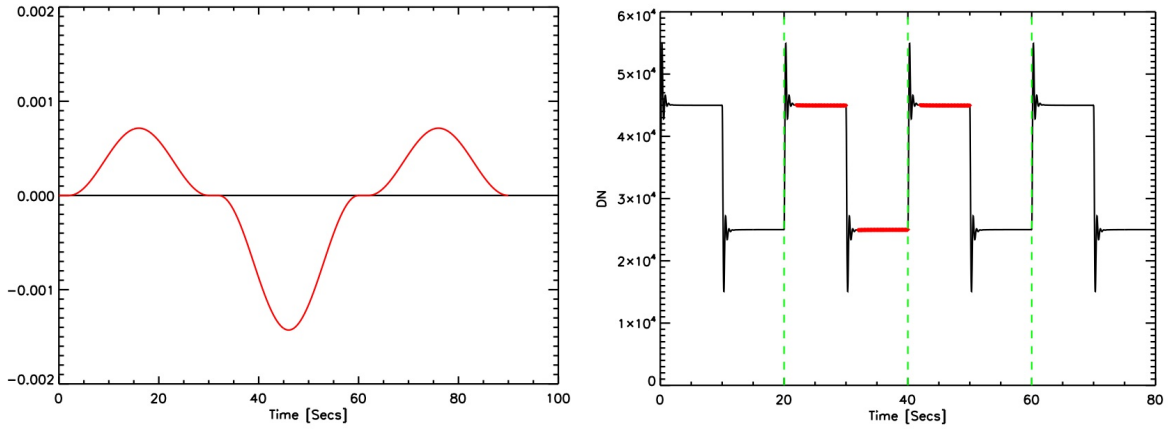

Figure 30: (a) The Hanning window filter function over 1.5 shutter cycles. At transitions, the Hanning window filter function goes to zero and is smooth. (b) Sample ESR DN time series for several shutter cycles where the prism dwell time is 20 seconds and prism steps occur at 20, 40, and 60 seconds (green dashed lines). Areas overplotted in red show the DN's used in data analysis showing that transients following shutter transitions are excluded.

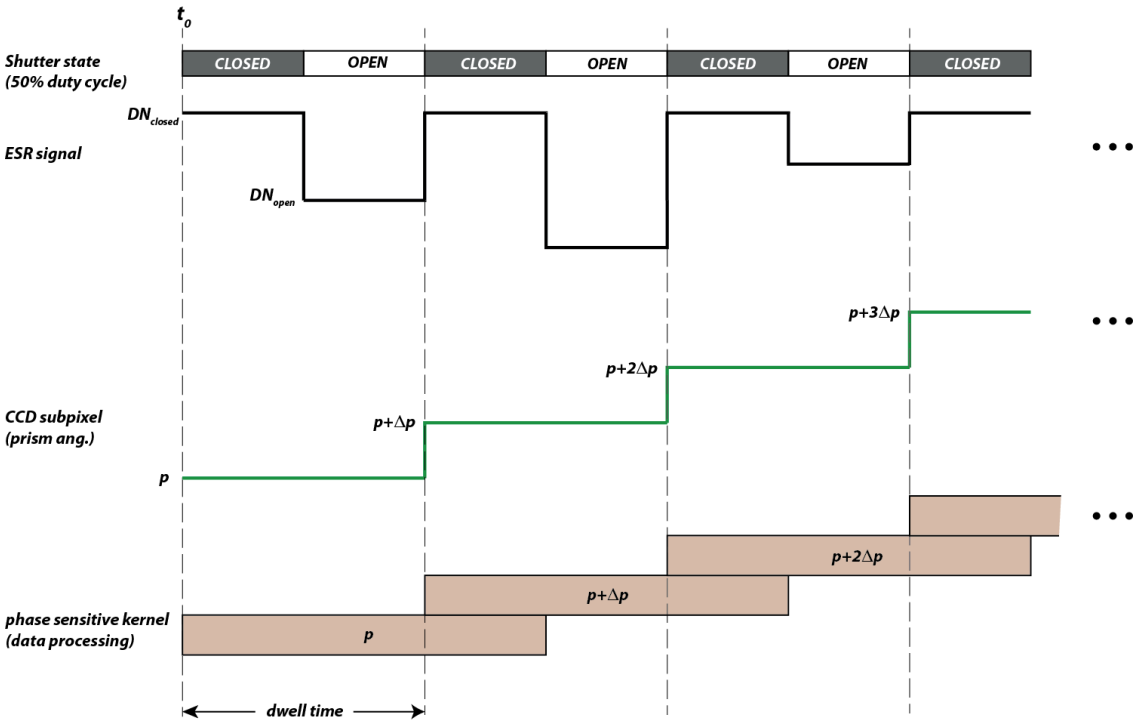

Figure 31: Sample SIM ESR operation and phase sensitive kernel for a 50% duty cycle: When ESR shutter is open, DN's decrease as the balance on the heater is reduced to maintain the same temperature. Each CCD subpixel step requires a full closed and full open shutter state, referred to as the "dwell time". The dwell time is constant, although it may be different for different scan regions to maximize the signal-to-noise ratio for the measured signal. A longer dwell time results in reduced measurement noise.

5 Calibration and Characterization

Characterization is the process used to quantitatively understand the operation of an instrument over a range of operating and viewing conditions that would be experienced by the instrument on-orbit. Characterization involves the measurement of all relevant instrument parameters over this range of instrument and environmental operating conditions.

Calibration is the process through which an instrument is subjected to known, controlled signal inputs and its response is quantitatively defined. For the level of accuracies required in climate monitoring, characterization and calibration are primary instrument requirements.

The extensive characterization and calibration steps undertaken for the TSIS TIM and SIM instruments are detailed in this section. The TSIS ground calibrations include unit level calibrations in the LASP/CU calibration laboratory and system level calibrations occur primarily at LASP/CU TSI Radiometer Facility (TRF) and Spectral Radiometer Facility (SRF), which provide a radiometric tie to the National Institute of Standards and Technology (NIST) radiometer irradiance reference standards. An overview of the TRF and SRF facilities was provided in Sections 2.4.1 and 2.4.2.

A number of critical unit level tests must be performed for the SIM and/or TIM sub-systems:

1. A telecentric metrological camera system is used to compare the entrance slit against a precision grid to obtain an effective slit area at several wavelengths. The effective slit narrowing as a function of λ for SIM has been measured and characterized for pointing, temperature, and wavelength effects.
2. Broadband and laser BDRF (bidirectional reflectance function) studies determine the properties of the nickel phosphorous black.

3. The ESR detector sensitivity will be compared against a trap diode system that serves as a transfer standard to the NIST cryogenic radiometer.
4. The refractive index of the SIM prism material will be experimentally validated prior to launch using the method outlined in the paper of *Tropf and Thomas* [1998].
5. Prism transmission tests will be measured at LASP.
6. Critical electronic components will be compared and tracked against NIST traceable standards, including standard voltage and resistance values.
7. Samples of all critical components will be kept as ground witnesses. As metrological equipment improves the measured standards can be re-evaluated. This is particularly true for the apertures and the components used to produce the standard watt. Protecting and preserving samples of the prism glass will be important to study long-term changes in the material.

The calibrations of the sun sensor and analog monitors are also considered part of the unit level calibrations. The sun sensor will be calibrated by the manufacturer with a precision of 10 arc-seconds and will be verified again during the TSIS instrument-level calibrations. The analog temperature and voltage monitors will be calibrated with a precision better than 0.1 °C and 20 millivolts.

5.1 TIM Ground Calibrations

Meeting the 100 parts per million (ppm) combined standard uncertainty in total solar irradiance (TSI) requires several precision calibrations. The most fundamental of these calibrations are performed on the ground, because they are generally more accurate than possible in flight, and can be ultimately transferred to in-flight instrument. *Kopp et al*. [2005a] provide an in-depth discussion of pre-flight ground calibrations as well as on-orbit flight calibrations.

Table 11 lists the TIM ground calibrations, many of which are described in further detail in Sections 5.1.1 through 5.1.5.

Table 11: TIM Pre-flight Component Calibrations

Quantity	Methods	Standard	Check Method
Shutter waveform	Transmission (time)	Digital scope	Mechanical model
Aperture	CCD camera vs. Ronchi ruling	Laser Interferometer / Ronchi ruling	NIST Aperture, diffraction calc
Cavity Absorption	Laser scans, reflection ratio at several wavelengths	Spectralon, diode linearity	Scatter theory, NIST check on one cone.
Loop Gain	Feed forward Calibration	Ratio measurement	Calc. from model
Equivalence ratio: distributions	Measure distributions with pulsed laser excitation	Ratio measurement	Calc. from model and reflectance meas.
Equivalence ratio, Green function	Calculate from first principles. Parameters from tables	Timing measurements,	Frequency variation. Pointing variation
Standard Volt	Measure at test connector, keep ground witnesses.	HP3458A, Josephson Junction	Fluke 723B, carry to NIST
Standard Resistance	Measure 4-wire at test connector, keep ground witnesses.	HP3458A, Quantum Hall	Tegam SR104
Full Scale count	Electronic counter		Ab initio design check
DAC Linearity	Sample hold, HP3458A	Ratio measurement	
Off axis rejection	Solar simulator + goniometer	Ratio measurement	
Shutter leakage	Solar simulator + silicon diode	Ratio measurement	
Dark signal	LN2 cryo-target	TIM, ratio	Model & theory
Cavity monitor diodes	Solar simulator, collimated	Lab radiometer	
Electrical cross talk	Analyze bridge signals	Volt/ratio measure	

Thermal cross talk	Solar Simulator, un-used pair	Ratio measure	Thermistor gradients
Temperature differences	Housekeeping thermistors	Hart 1521/5611T	NIST trace
Resistor TCRs	HP3458A, table values		

5.1.1 Cavity Absorptance

The cavity reflectance is measured at wavelengths (457, 532, 633, 850, 1064, 1523, 3300 nm) [*Heuerman et al*., 2006] spanning the solar spectrum. Laser scans at these wavelengths are used to map the reflectance of the interior of the cavities [*Kopp et al*., 2005a]. The cavity absorption α is one less the cavity reflection ρ at the center of the pointing field of view and is averaged over the solar spectrum. Except for possible updates from the ground witness program, duty-cycle corrections, or reflectance monitors, this value is assumed constant in time and fixed at the pre-launch calibration value.

Kopp et al. [2005a] provide details and images of the 2-D spatial maps of cavity reflectance, and how they are supplemented by a broad-beam laser calibration at 10.6 μm to extend the cavity reflectance calibrations to the infrared. The pre-launch calibration includes the variation of ρ with pointing offset. Table 12 lists the solar-weighted reflectances for the four TIM cavities. The uncertainties in the reflectances are 14%.

Section 5.2.3 discusses the in flight calibration of changes in cavity absorptance due to pointing effects during cruciform and raster scans of the Sun. The on-orbit sensitivity of cavity absorptance depends on the location of the Sun within the instrument field of view. Section 5.2.6 describes the Field of View (fov) correction for TIM.

Table 12: Solar-weighted reflectances for the four TIM cavities: Absorptance is equal to 1 minus reflectance.

TIM Cavity	Effective Solar-weighted Reflectances (ppm)
Cone A	169
Cone B	139
Cone C	307
Cone D	360

5.1.2 Aperture Area

The diamond-turned aluminum apertures were measured at NIST. Table 13 lists the four TIM aperture areas, each with relative standard uncertainties better than 25 ppm. The following discussion details the calibration and characterization of the apertures for temperature, diffraction, and bulk modulus expansion effects in a space environment.

Table 13: Geometric area of TIM apertures.

TIM Aperture	Geometric Area (cm^2)
Cone A	0.50034
Cone B	0.50028
Cone C	0.50044
Cone D	0.50021

Diffraction is the dominant contributor to the aperture area uncertainty. An energy-weighted average wavelength (947 nm) analysis of the solar spectrum by NIST suggests a 45 ppm uncertainty due to diffraction [*Kopp et al*., 2005a; *Harber et al*., 2006].

The diamond-turned edges are imperfect requiring corrections for scattered and reflected light, which are ~40 ppm based on ground-based calibration that allows for a 2nd order thermal expansion correction for aluminum α_{Al} of the flight aperture. Ground-based calibrations of temperature corrections to aperture area are known to 0.001 ppm/C. Changes in aperture area to pressure changes between the ground calibrations and flight environment are known to better than 1 ppm.

The above calibrations result in a calibrated aperture area for each cone $A_{P,Cal}$ at a specific temperature T_{Cal}. Section 5.2.2 discusses the flight calibration of aperture area required to correct from the calibration temperature to the (regulated and measured on orbit) temperature of the heat sink.

5.1.3 Standard Watt

The standard Watt comes from the stable voltage and resistance references. Sections 3.1.1 and 3.1.2-3.1.3 describe the relationship between the changes in electrical heater power applied to the ESRs that compensate for variations in absorbed radiant power as the ESR shutter cycles open and closed. The electrical power is produced by pulse-width modulating a voltage standard reference through a standard reference resister embedded in each ESR. *Kopp et al*., [2005b] contains in-depth discussion of the temperature dependencies of the voltage and resistor references.

The pre-launch calibration of the stable voltage and resistance references are the dominant way in which on-orbit changes are tracked (i.e. simultaneous TSI measurements from two ESRs, with unique heater resistors and voltage references are compared on-orbit to track changes). Both the voltage and resistor references have temperature dependencies, which have been characterized to < 1ppm/year change in relative voltage and less than 3 ppm change in relative resistance, respectively.

The 7.1 VDC reference voltages are from Linear Technology LTZ1000 Zener diodes. These voltage references are calibrated pre-launch for temperature dependencies, which are fairly linear across a broad temperature range [see *Kopp et al*., 2005b]. The absolute values of the reference voltage are calibrated with an 8.5 digit HP3458A meter.

Likewise, pre-launch absolute calibrations of the effective heater resistances for the four TIM ESRs at the operating temperature are conducted. The measured temperature coefficients of the 39-MWS-800-HML heater wire range from 8-11 ppm/°C and are used for temperature corrections based on four different instrument temperatures [*Kopp et al*., 2005b].

For both voltage and resistor references, it is assumed that changes in the flight standards will track the ground witness units.

5.1.3.1 DAC Calibration Factor $-V^2/(MR)$

A precision duty-cycle type Digital-to-Analog Converter (DAC) converts the data numbers produced by the servo system to the replacement power. The changes in the substituted electrical power are proportional to the duty cycle and the V^2/R power, corrected for the lead resistances.

$$\frac{dP}{dDN} = \frac{V^2}{M\ R'_H} \qquad (5.1.3.1.1)$$

where V is the value of the precision, buffered, standard voltage. The integer $M \equiv 64000$ is the full scale (100% duty cycle) count. R'_H is the effective heater resistance at the regulated operating temperature. R'_H includes lead corrections both inside and outside of the optical head as well as the on-resistance of the MOSFET switch (Figure 31) in the pulse width modulator circuitry.

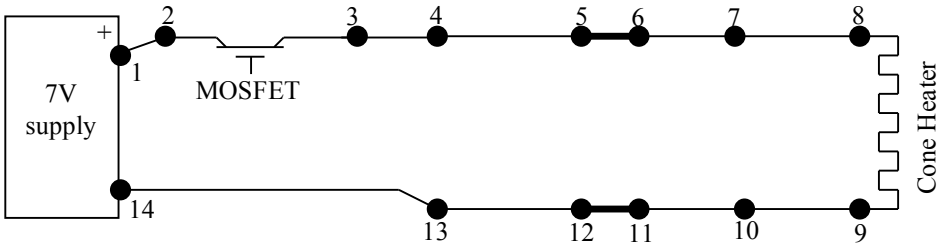

Figure 32: Standard Watt Pulse Width Modulator Hardware: The numbered nodes are measurable points in the circuit. See Table 14 for their usage and the required resistances and voltages.

Table 14: Definitions of Nodes and resistances in the Pulse Width modulator

Nodes	Symbol	Definition
1-2	*R1*	Trace Resistance, power node to MOSFET
2-3	*R2*	MOSFET on resistance plus trace to test point
3-4	*R3*	Trace Resistance, MOSFET to turret
4-5	*R4*	Wire resistance turret to feedthrough
5-6	*R5*	Feedthrough resistance
6-7	*R6*	Vacuum wire resistance, feedthrough to hub
7-8	*R7*	#32 wire resistance, hub to cone terminal
8-9	R_{CONE0}	Resistance, cone heater, at ambient temperature T0
9-10	*R9*	#32 wire resistance, cone terminal to hub
10-11	*R10*	Vac wire resistance, hub to feedthrough
11-12	*R11*	Feedthrough resistance
12-13	*R12*	Wire resistance feedthrough to turret
13-14	*R13*	Trace resistance, turret to star ground
14-1	*V*	7V power supply voltage, test connector
1-4,13-14	T_{PWB}	Temperature of the printed wiring board near the traces.
5-6,11-12	T_{CASE}	Case, or vacuum enclosure temperature
7,10	T_{HUB}	Hub temperature, side thermistor temperature
8,9	T_{CONE}	Operating Cone temperature, regulated to 30°C
All	T_0	Circuit temperature during the resistance measurements
Define	R_{TRACE}	R1+R3+R13
3-14	R_{TEST}	Loop resistance measured from the test connector at T_0
4-5,12-13	R_{JUMP}	R4+R12, jumpers, board to feedthroughs

In a simplified notation, the equivalent heater resistance is:

$$R'_H = \frac{\left(R1 + R2 + R3 + R4 + R5 + R6 + R7 + R_{CONE} + R9 + R10 + R11 + R12 + R12 + R13\right)^2}{R_{CONE} + \left(R7 + R9\right)/2} \quad (5.1.3.1.2)$$

It is understood in Equation 5.1.3.1.2 that each resistance is corrected by temperatures from telemetry as described in Section 5.1.3. It is assumed here that half of the power generated in the #32 wire lead resistances, R7 and R9, flows to the cavity.

5.1.4 Shutter Waveform

The calibration of the shutter waveform factor characterizes the non-unity transmission (< 3 ppm) when the shutter transitions from open to closed position. This effect produces a relative correction of less than 1 ppm in the phase sensitive analysis of the data (see Section 4.3.1).

The shutter waveform factor ***S*** is a complex phasor, computed using the same ground-processing Fourier transform algorithm as used on the data numbers (Section 4.2.1). The real part of this waveform is within one ppm of $2/\pi$ [*Kopp and Lawrence*, 2005]. The deviations from $2/\pi$ depend on the standard deviation σ of the derivative of the shutter rise-time and the timing error Δt in the 50% duty cycle. Equation 5.1.4.1 is the parameterized model of the real part of the shutter waveform.

$$\frac{2}{\pi} \rightarrow \frac{2}{\pi}\left(1 - \frac{\sigma^2\omega^2}{2} - \frac{\Delta t^2\omega^2}{8}\right) \qquad (5.1.4.1)$$

5.1.5 Equivalence Ratio

The equivalence ratio is a measure of the change in electrical power (Z_H) that gives precisely the same cone temperature as that provided by the incident sunlight is a measure of absorbed radiant power (Z_R) incident on the ESR cone (Section 3.1.7), with the theory of nonequivalence described in *Hengstberger* [1989]. In our case, with phase sensitive detection at the shutter frequency, the equivalence ratio is the ratio of two complex thermal impedances. In Figure 28, we see that the thermal impedances $\boldsymbol{Z}_R$ and $\boldsymbol{Z}_H$ are the transfer functions to the thermistor from radiant and heater power, respectively. The symbols $\boldsymbol{Z}_R$ and $\boldsymbol{Z}_H$ in bold face denote the phasor transfer functions at the shutter fundamental frequency. The equivalence ratio is determined by pre-launch characterization where it is calculated from model calculations, with generous uncertainties in the experimentally determined parameters. *Kopp and Lawrence* [2005] provides an in-depth discussion of the TIM equivalence calculation and the uncertainties in the model parameters.

The dominant task is to measure the distributions of absorbed radiation and applied heater power as a function of input distance along the ESR cavity. This is done through measuring the temperature jump at absorption of a pulsed laser beam and through knowledge of the change in the electrical heater distribution with distance along the cone from the wire wound resistor on the external portion of the cone. The temperature measurements are made with a row of micro-thermistors, clamped to the exterior of a test cone.

The equivalence ratio is theoretically determined based on a parameterized model of the heat flow in the radiometer. The parameters of the model are experimentally determined, but their usage in the model is entirely theoretical. The model independently calculates the thermal impedances $\boldsymbol{Z}_R$ and $\boldsymbol{Z}_H$ and then divides the complex number $\boldsymbol{Z}_R$ by the complex number $\boldsymbol{Z}_H$. Using thermal transfer theory, one calculates the thermistor response from a unit power input at a general position $\vec{X}$ on the bolometer cavity. The ratio of temperature response to power input at position $\vec{X}$ is the Green function impedance $Z\left(\vec{X}\right)$. Given the normalized distributions $f_R\left(\vec{X}\right)$ and $f_H\left(\vec{X}\right)$ of absorbed radiation and heater power, we can calculate the equivalence ratio.

$$\frac{Z_R}{Z_H} = \frac{\int f_R\left(\vec{X}\right) Z\left(\vec{X}\right) d^3\vec{X}}{\int f_H\left(\vec{X}\right) Z\left(\vec{X}\right) d^3\vec{X}} \qquad (5.1.5.1)$$

5.2 TIM Flight Calibrations

On-orbit calibrations are frequently not of the precision possible using ground facilities due to the variability in the spacecraft thermal environment and power sources. However, for TIM they are important for measuring the thermal contributions to the instrument signal and for monitoring in-flight gain in the servo system. Instrument degradation, monitored by long-term changes in cavity absorption, is addressed specifically in Section 7.

Table 15 lists the on-orbit re-calibration methods used for TIM. Expanded details on several of these methods are provided in Sections 5.2.1-5.2.7.

Table 15: TIM In-flight Re-Calibrations

Quantity	Methods
Shutter waveform	High speed DN time series. Look for timing changes.
Aperture	Correct for housekeeping temperature. Ground witnesses.
Cavity Absorption	Watch changes in cavity diode monitors.
Equivalence ratio	Second-guess ground witness.
Equivalence ratio * Cavity Absorption	Pointing variation from cruciform scans. Degradation from duty cycle of cavities.
Loop Gain	Use Feed Forward. Calibration with feedforward
Standard Volt	Ground witnesses.
Standard Resistance	Assumed constant. Temperature correct. Ground witnesses.
Off axis rejection	Sunrise, sunset excess irradiance.
Dark signal	Dark space observations. Correct for temperature
Cavity monitor diodes	Get initial signals, watch for changes.
Thermal cross talk	Watch thermistors at fundamental. Watch closed-shutter pair.

5.2.1 Shutter Waveform factor

The TIM is a shuttered radiometer with the shutter running with a 0.01 Hz square wave. Changes in the shutter rise time and timing error will be monitored for in the output data numbers that follow a square wave that is proportional to changes in the solar irradiance. Accounting for any variability in the shutter waveform factor will be accomplished as described in Section 5.1.4 and corrected in the post-processing phase sensitive detection method.

5.2.2 Aperture

Section 5.1.2 discussed the calibrated aperture areas $A_{P,Cal}$ for temperature, diffraction, bulk modulus expansion, scattered and reflected light, and pressure changes in the space environment for a calibration temperature T_{Cal}. Equation 5.2.2.1 provides the flight correction necessary to correct from the calibration temperature to the (regulated and measured) heat sink temperature T_{Sink} from the instrument housekeeping packet. α_{Al} is the thermal expansion coefficient of aluminum.

$$A_P = A_{P,Cal}\left(1 + 2\alpha_{Al}\left[T_{Sink} - T_{Cal}\right]\right) \qquad (5.2.2.1)$$

5.2.3 Cavity Absorption

On-board reflectance-tracking photodiode monitors and duty cycling of the ESRs will be used to monitor for on-orbit degradation of cavity absorption. In the event of no changes, the pre-launch calibration value for cavity absorption (Section 5.1.1) will be assumed fixed and constant in time.

Each cavity has a photodiode monitor to monitor the light reflected from each cavity, and is sensitive to small changes in cavity reflectance. Monitoring these photodiode signals are useful mainly for indicating relative changes in cavity reflectance (1 – cavity absorption). On-orbit, raster and cruciform scans of the Sun will be used to monitor the variation of cavity reflectance (together with variations in equivalence ratio) with pointing changes.

The simultaneous pair-wise inter comparisons of the TIM cavities will be used to monitor for long-term changes in cavity absorption and is discussed in detail in Section 7. *Kopp et al*., [2005b] discuss the duty cycling of ESRs for the degradation monitoring of the SORCE TIM instrument. In the case of SORCE TIM, the primary ESR showed ~ 0.11 ppm/day degradation indicating the robustness of the metal NiP black cavity interior, as opposed to degradation of black paint. The TSIS TIM uses the same NiP black cavity interior.

5.2.4 Loop Gain

The servo open-loop gain $\boldsymbol{G}$ is the end-to-end complex gain of the control loop at the shutter fundamental. The gain of the servo loop affects the measured signal when responding to non-equilibrium conditions. These conditions are largely prevented by applying a feedforward signal that anticipates the power changes as the shutter open and closes [*Kopp et al*., 2005b].

The loop gain is known from circuit analysis and pre-flight calibrations, but will be periodically (at least once per month) re-calibrated in flight. A test amplitude $\boldsymbol{DN_{FTEST}}$ is added to the loop by ground command at the feed forward junction as shown in Figure 28. The fundamental response at the output is $\boldsymbol{DN}_{\mathrm{TEST}}$ and the loop gain is calculated as:

$$\boldsymbol{G} = -1 + \frac{\boldsymbol{DN}_{FTEST}}{\boldsymbol{DN}_{TEST}} \qquad (5.2.4.1)$$

The TSIS TIM loop gain will be calibrated in flight to better than 1 ppm uncertainty.

5.2.5 Standard Volt

It is assumed that the two flight standard voltages will track the ground witnesses (at least six), although we expect a 1-2 ppm change per year in the flight voltages. Section 5.1.3 details the extensive absolute calibrations of the voltages undertaken pre-launch.

5.2.6 Pointing Sensitivity

The sensitivity of TIM depends on the location of Sun within the instrument field of view, given by pointing angles θ and ϕ. The field of view factor $f_{FOV}(\theta,\phi)$ in the denominator of the measurement equation (Section 4.2.1) is equal to one on axis, and is used to transfer the on-axis characterization to the actual solar position within the FOV. Although we determine the variation of response vs. the pointing angles in pre-launch tests, the most accurate data come from the periodic cruciform and raster scans in flight. Since the pointing precision of the SORCE spacecraft is sub-arc minute and the basic noise of TIM is < 1 ppm, we expect that the empirical method will add little uncertainty to the measurements.

The sensitivity to pointing effects is actually in cavity absorption, the equivalence ratio, and the cosine-theta aperture factor. These individual effects are accounted for by the single correction factor $f_{FOV}(\theta,\phi)$ (Section 4.2.3.3).

5.2.7 Dark Signal

The definitive measurements of the dark offset signal due to infrared radiation within TIM are made in flight by observing dark space during the eclipsed portion of each orbit. The correction is discussed in detail in *Kopp et al*., [2005a]. The measured dark signal (roughly -3.15 Wm^{-2} for SORCE TIM; a negative value due to the *loss* of energy from the cavities into space when the shutter is opened) is fitted to four instrument temperatures from different portions of the instrument – the cavity, aperture plate, pre-baffle, and shutter. The temperature fitting provides the highly correlated basis vectors for modeling the observed dark irradiances, which are then used to estimate the background contribution to the solar signal at actual observing times. The dark signal correction was 2700 ppm for SORCE TIM

and 1645 ppm for Glory TIM. Section 4.2.1 describes how the dark signal numbers are converted to irradiances using the TIM measurement equation.

5.3 SIM Ground Calibrations

5.3.1 ESR

The ESR is the absolute detector for the TSIS SIM instrument. Sections 5.3.1.1 - 5.3.1.6 detail the characterization and calibration response of the ESR to thermal, electrical, and noise fluctuations, the ESR efficiency, plus others. Refer to Section 3.2.5 for details on the basic thermal and electrical design of the SIM ESR.

5.3.1.1 Characterization of Thermal Parameters

The thermal properties of the ESR have been approximately calculated by considering the thermal properties of each element. To accomplish this, the mass and volume of the materials comprising the diamond strip, solder, NiP black, and toadstool mounts were measured. The heat capacities per unit mass, or per unit volume, were obtained through and the multiplication of these quantities resulted in a heat capacity (J/K) for each component. The heat capacity of the ESR is the sum of the values for the individual components. These calculated results are shown in Table 16 and compared to the measured heat capacity of the ESR (final row).

Table 16: Calculated heat capacity of individual ESR elements compared with a measured value for the ESR.

Item	Mass [g]	Heat Capacity [J/K]
Diamond Strip	0.0160	0.0081
Thermistors	-	0.0023
Solder	0.0046	0.0009
NiP	0.0063	0.0028
Toadstools	0.0031	0.0035
Total	-	0.0176
Measured	-	0.024

The toadstool mounts on the ESR bolometer are glued via kapton tubes to the copper block heat sink resulting in a thermal link. The estimated thermal conductivity of this link using knowledge of the dimensions and thermal conductivity of the kapton tubes is 33,496 K/W and the measured thermal conductance from the ESR to the copper block is approximately 3700 K/W.

5.3.1.2 Characterization of Electrical Resistances

Precision measurements of all the thermistors and heaters in the ESR were performed after the ESR had been mechanically assembled, but before the electrical boards had been built and installed.

5.3.1.2.1 ESR Thermistor Offsets

There are five thermistors in the TSIS SIM ESR. Three are chip type (for the A, B, and C ESR channels) and two are leaded (for the copper block and outer case). There are small offsets that exist between each thermistor. These offsets need to be characterized in order to bring all thermistors on the ESR assembly into agreement. The beta model, a simplified version of the Steinhart-Hart model, was used to characterize the negative temperature coefficient thermistors. The use of this simplified model was justified by the small temperature-induced error (75 mK) over a temperature range of 15-35° C.

Equation 5.3.1.2.1.1: The beta model used to characterize the ESR chip type thermistors requires knowing the resistance at two temperatures.

$$\frac{1}{T} = \frac{1}{T_0} + \frac{1}{\beta}\ln\left(\frac{R}{R_0}\right) \qquad (5.3.1.2.2.1)$$

The value of β for a given thermistor is essentially a bulk property of the thermistor material and was found to be quite similar from thermistor to thermistor. The value of the measured resistances at the two temperatures, R and R_0, on the other hand, are determined by the amount of thermistor material between the two leads, and therefore dependent on the particular thermistor.

With the β values fixed, each of the other thermistors R_0 was adjusted to minimize the temperature difference from the copper block thermistor. The measurements were performed with the ESR in the STOVE chamber used to provide a constant-temperature "bath". Over a period of 20 hours, the ESR temperatures were stable to 0.1°C and 2-wire resistance measurements, accurate to within 120 ppm, were taken on each thermistor. The final thermistor β and R_0 values are summarized in Table 17.

Table 17: Final measured ESR thermistor β and R_0 values.

Thermistor	R_0 [Ω]	T_0 [°C]	β [1/K]
ESR A	5048.9579	25	3881.7
ESR B	5047.3368	25	3881.7
ESR C	5048.0268	25	3881.7
Copper Block	9965.59	25	3910.92
Outer Case	9964.3681	25	3910.92

5.3.1.2.2 Temperature Dependency of ESR Heater Resistances

In a similar experimental setup to that described in Section 5.3.1.2.1, the dependency of the ESR heater resistances to temperature change was measured. In the STOVE chamber (under vacuum), the ESR was heated up to ~30° C and then allowed to cool down. The measured resistance of the ESR heaters and their temperature coefficients was observed during the cool down period ranging from approximately 29 to 23° C and a linear fit of resistance versus temperature yielded the coefficients shown in Table 18. From this table, the heater resistance (Ω) for ESR A at 30° C, for instance, is then:

$$R_A(30°C) = 101840.04\Omega - 12.136069\frac{\Omega}{K} * 30 = 101475.96\Omega \qquad (5.3.1.2.2.1)$$

Table 18: Measured dependency of ESR heater resistances to temperature change.

Channel	R at T=0° C [Ω]	Temperature Coefficient [Ω/°C]
ESR A	101840.04	-12.136069
ESR B	101511.26	-12.094751
ESR C	100839.25	-11.987703

As an additional check, measured ESR heater resistances were made at two different temperatures and the comparisons of these measured resistances to these expected results differed by 12 - 42 ppm across the three channels. These measurements were made from where the 7.1 Volt reference board connects to the ESR, which required correction for an approximate 9 Ω amount of lead resistance.

The measured resistance of the outer case heater was 25.9315 Ω.

5.3.1.2.3 ESR "top" resistors and 7.1 Volt references

The characterizations described in Sections 5.3.1.2.1 and 5.3.1.2.2 were performed independent of the flight electrical boards. However, other electrical calibrations are dependent on these boards including, the "top" resistor and the 7.1 Volt reference. The measured resistance of the Wilbrecht 100 kΩ "top" foil resistor for each ESR channel is provided in Table 19. The approximate 9 Ω correction to the lead resistance (Section 5.3.1.2.2) is necessary for the actual power calculation. There is a 5 ppm/°C temperature coefficient on the top resistors meaning the temperature can change by ±10 °C while target resistance uncertainties remain within 50 ppm.

Measurements of the 7.1 Volt reference were taken during the build of the flight boards and several times afterward as detailed in Table 20.

Table 19: Measured resistance of Wilbrecht 100 kΩ "top" foil resister.

Channel	Measured Resistance [Ω]
ESR A	100,116.0
ESR B	99,965.3
ESR C	99,958.9

Table 20: Time series measurements of the 7.1 Voltage reference.

Date	Measured Voltage [V]
18 March 2011	7.166016
20-27 May 2011	7.165776
03 August 2011	7.165859

5.3.1.3 Calibration of Thermal Parameters

Section 5.3.1.1 details the thermal characterization of the ESR thermistors and heaters. In this section we present the thermal calibrations of these elements, where the measured response of these elements to a known amount of applied power is determined. Calibrations were also performed with the TSIS SIM ESR prototype (witness ESR). The prototype had a heater on the outer case and the copper block, allowing the calibration of all ESR elements (ESR A, B, C, copper block, and the outer case). More extensive details on ESR thermal calibrations (Sections 5.3.1.1 and 5.3.1.2) can be found in the TSIS SIM Flight ESR Calibration Document (ref. in Table 1).

5.3.1.3.1 Thermal Conductivity of the ESR

The thermal conductivity of the diamond strips through the Kapton tubes to the copper block was calibrated to obtain the heat capacity of the diamond strip assemblies. A known power was applied to the resistive heater and the thermal response measured (Figure 33).

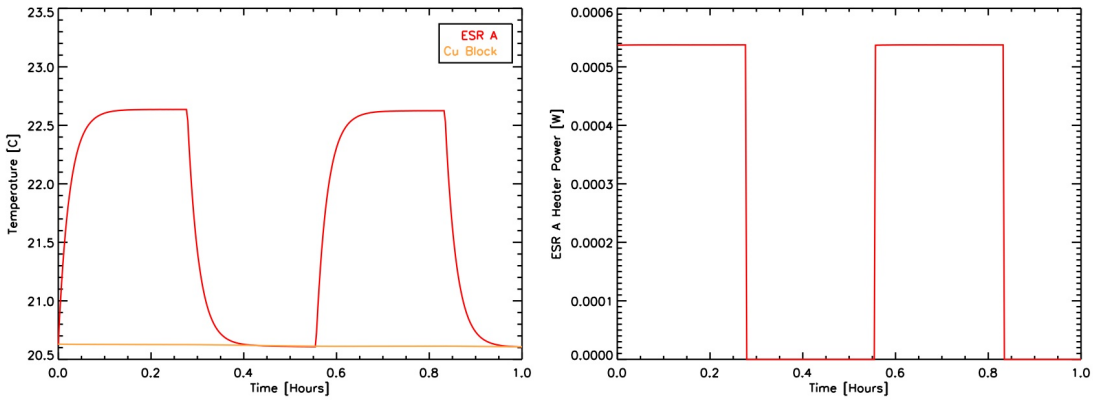

Figure 33: Measured thermal response of SIM A ESR and the copper block to known variations in power.

In a simplified thermal model, the net power flow into an ESR channel (P) is balanced by the heat dissipated by the ESR heater (P_H) plus the thermal conduction of heat (Z) between the copper block and ESR driven by their temperature differences (T_{Cu} and T). The ESR temperature responds to the input net power in a time dependent manner driven by the heat capacity of the ESR channel. Using singular value decomposition and temperature measurements of the ESR (including time dependency) and the copper block, and measurements of the power dissipated by the ESR heater, the heat capacity and thermal conductivity of the ESR are calibrated. These calibrations are performed for the TSIS SIM prototype 1 and 2 units, and the flight unit and summarized in Table 21.

Not addressed in this simplified model but included in calibration efforts are the 1) small artificial temperature offsets that remain despite careful thermistor characterization and, 2) the effects of heater on and off transitions on the several second latency of internal conductivity times within the ESR. Detailed calibrations of the heat capacities and thermal conductivities of the ESRs were also performed in an element-by-element fashion (not shown).

Table 21: Calibrated heat capacities and thermal conductivities of the TSIS SIM ESR units.

	c_P, Heat Capacity [J/K]			**Z_0 to Copper Block [K/W]**		
	ESR A	**ESR B**	**ESR C**	**ESR A**	**ESR B**	**ESR C**
Proto 1	0.0232	0.0234	0.0228	3754.8	3450.1	3534.2
Proto 2	0.0239	0.0249	0.0236	3699.3	3677.0	4141.4
Flight	0.0241	0.0241	0.0251	4223.4	4351.2	4136.4

5.3.1.3.2 Outer Housing and Copper Block Temperatures

The outer case and copper block temperature measurement circuits were calibrated by monitoring the raw data number (DN) values measured by the digital signal processor (DSP) as a function of temperature. These raw DN values were compared to model results of expected DN values based on the actual circuits. The resistance values in the model were adjusted to match the measured results and the model results were then fit to polynomials (Figure 34). The polynomial fits provide the following simple approximations that allow the outer housing and copper block temperatures to be easily calculated from their respective raw DN values reported by the DSP:

$$T_{OC} = 29.6201 - 0.577534 * RDN_{OC} \quad (5.3.1.3.2.1)$$

$$T_{Cu} = 29.9673 + 21.7649 * RDN_{Cu} - 9.02142 * RDN_{Cu}^2 + 5.51460 * RDN_{Cu}^3 \quad (5.3.1.3.2.2)$$

where T_{OC} is the temperature of the outer case, T_{Cu} is the temperature of the copper block, and RDN_{OC} and RDN_{Cu} are the "reduced" raw data numbers from the outer case and copper block, respectively. The "reduced" raw data

number is defined as DN/5373788, which varies between -1 and +1 and serves the purpose of simplifying the polynomial coefficients.

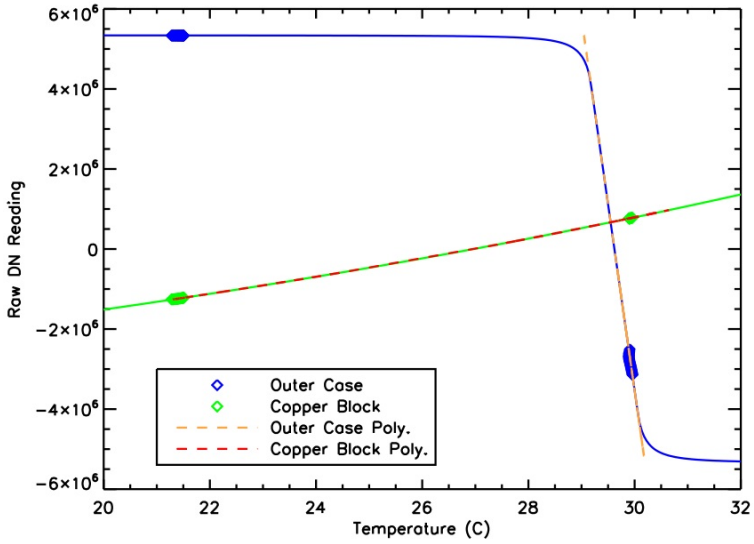

Figure 34: Raw DN values measured by the DSP as a function of temperature of the outer housing and copper block. Measured results (diamonds), model results (solid lines), and polynomial fits (dashed lines) are shown.

5.3.1.4 Calibration of Electrical Noise

Accurate knowledge of the baseline electrical-induced noise of the non-illuminated ESR is important because it provides the minimum detectable signal and the corresponding signal-to-noise value for each wavelength. Electrical noise tests were performed on both prototype ESRs and on the flight ESR through time series measurements of ESR signal in experimental conditions without light or feedforwards applied. A noise power spectrum of the measured time series is computed. Through averaging and high-pass time domain filtering to remove an artificial 1/*f* discontinuity introduced by edge effects in the transformed spectrum, a smoothed power spectrum is calculated.

The smoothed power spectra are converted from DN to power and shown for each of the paired ESR channels (for the prototype and flight ESR) in Figure 35, where for all of these datasets the PID values were: Kp = 1.46, Ki = 0.059, Kd = 0.0, standing for the proportional, integral, and derivate term of the complex transfer function, respectively.

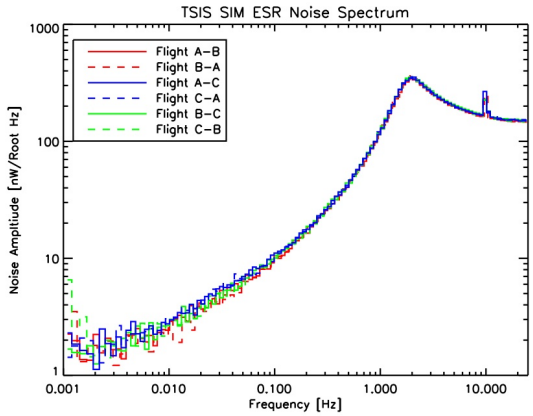

Figure 35: Power spectra for each pairing of the flight ESRs in nW/Root Hz versus frequency. The measured noise for the different pairings is similar.

The ESR noise decreases with increasing dwell time (defined in Figure 31). There is therefore a compromise between spectral interval covered and dwell time per sample. For example, in the visible and near IR measured signals are large (10-40 µW), and the dwell time can be shorter without sacrificing signal-to-noise ratio (SNR). However, in the UV, the ESR measured power will be low (0.1-1 µW), and the scanned spectral regions will therefore be narrower because dwell times will be longer to reduce noise. Figure 36 illustrates the ESR noise floor of the TSIS SIM (red) compared to the SORCE SIM (blue) on a log-log plot. The TSIS SIM ESR noise performance is approximately 5x better than the SORCE SIM.

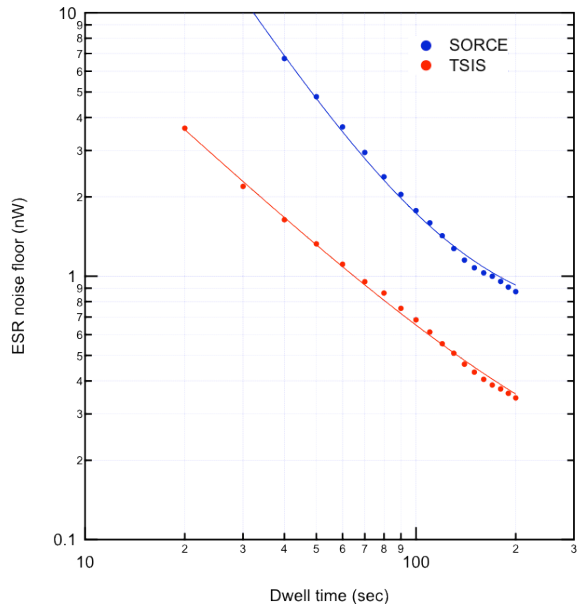

Figure 36: Comparison of ESR noise performance between TSIS (red) and SORCE (blue) SIM instruments. ESR noise is dependent upon dwell time, defined as one complete shutter open cycle and one complete shutter closed cycle.

5.3.1.5 ESR Efficiency

The ESR is the absolute reference for the SIM instrument; this requires that the ESR efficiency (a measure of the efficiency of the light absorption by the bolometer) be known. The efficiency of the ESR is a complicated function that is related to the spectral bidirectional reflectance distribution function (BRDF) that determines the reflectance of the NiP metal as a function of the direction of light illumination and instrument pointing. The illumination of the ESR by incoming light is also dependent upon the spherical hemisphere, which reflects light (with some loss of re-

imaging efficiency) back onto the bolometer strip in a wavelength-dependent manner and diffraction from the entrance slit.

Due to the complexity involved in determining the ESR efficiency, an end-to-end approach to characterizing the ESR efficiency has been adopted. We do this by illuminating an absolute reference modified to closely match the ESR with monochromatic light in the Spectral Radiometer Facility (SRF; Section 2.4.2). The SRF facility allows us to illuminate either the SIM ESR or a primary standard with nearly identical illumination at power levels typical of the Sun and under flight-like vacuum conditions over the 210-2400 nm wavelength range. Figure 37 shows the absolute offset of the ESR with respect to the SRF cryogenic radiometer and Table 22 reports the uncertainty in the absolute offset.

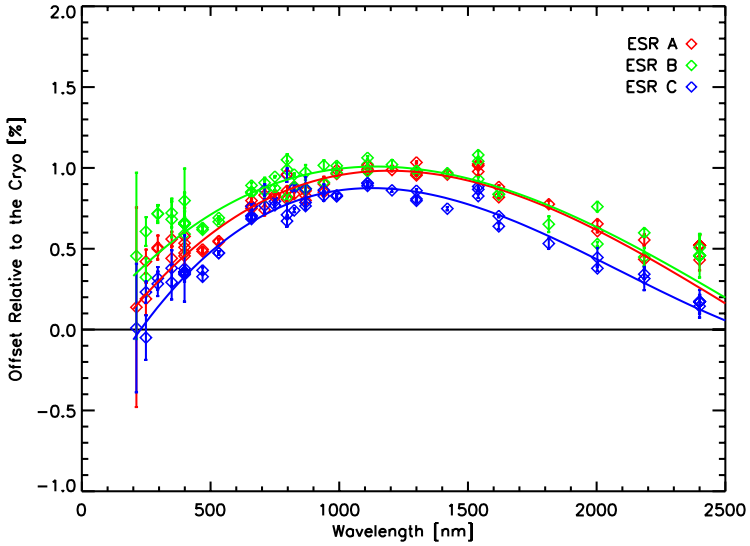

Figure 37: Measured ESR absolute efficiency presented as a percentage offset relative to the SRF cryogenic radiometer. Symbols are the measured points and lines are the fitted curves to the measurements.

Table 22: Uncertainty in the measured ESR absolute efficiency.

Channel	% Fit Unc. (k=1)
ESR A	0.081
ESR B	0.108
ESR C	0.087

5.3.1.6 ESR Loop Gain

The digital signal processor (DSP) acts to thermally balance the active ESR, that has a temperature T_R due to incident sunlight, to the reference ESR, with the temperature T_H, by varying the reference heater power. The servo "open-loop" gain G is the end-to-end complex gain of the control loop at the shutter fundamental shown in Figure 38. It is best calibrated in flight and on the ground with a special program of the DSP that injects a test square wave into the "closed-loop" and observing the response. The result is the ratio of two complex digital numbers. This test signal is the programmable "Feed Forward" signal F, also used to anticipate the change in solar radiation as the shutter is activated. If the feed forward signal is matched to the radiation signal the stability of the control loop gain is improved.

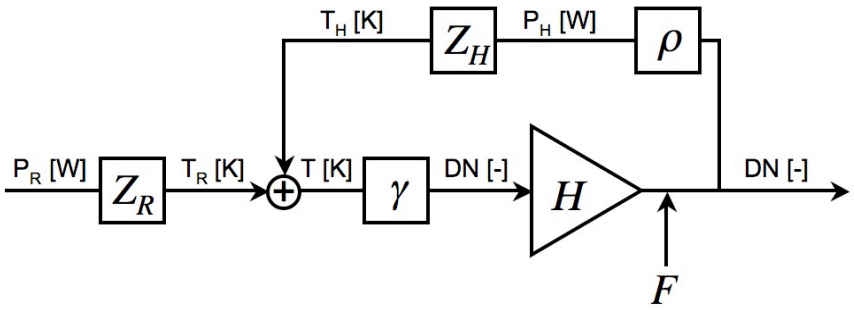

Figure 38: Schematic of the ESR feedback loop.

The blocks in Figure 38 are:

P_R = Optical Power [W]

Z_R = Radiative Thermal Transfer Function [K/W]

ρ = DN to power gain [W/DN]

H = PID Filter [-]

F = Feed-forward [DN]

γ = Temperature to DN gain [DN/K]

Z_H = Electrical Heater Thermal Transfer Function [K/W]

All the blocks except ρ, the DN to power gain, are complex and dependent on frequency. The data number D output from the control loop can be expressed after some algebraic manipulation as:

$$D = \frac{\gamma H T_R + F}{1 - \gamma H Z_H \rho} \tag{5.3.1.6.1}$$

During a gain measurement there is no radiation input and $T_R = 0$, leading to the following expression for the output data number:

$$D = \frac{F}{1 - \gamma H Z_H \rho} \tag{5.3.1.6.2}$$

Further rearrangement of terms introduces the unit-less term, G, called the open loop gain of the ESR servo:

$$G = -\gamma H \rho Z_H = \frac{F}{D} - 1 \tag{5.3.1.6.3}$$

A simplified expression for the input radiative power P_R can then be expressed as:

$$P_R = -\rho \frac{Z_H}{Z_R}\left(\frac{G+1}{G} D - \frac{F}{G}\right) \tag{5.3.1.6.4}$$

which can be simplified if the feedforward is set to zero as:

$$P_R = -\rho \frac{Z_H}{Z_R}\left(1 + \frac{1}{G}\right) D \tag{5.3.1.6.5}$$

ESR loop gain measurements can be monitored for effective thermal input noise. During a noise measurement (F = 0) and we can convert the measured D values to a thermistor temperature noise using:

$$T_R = \frac{D}{\gamma H}\left(1 - \gamma H Z_H \rho\right) \quad (5.3.1.6.6)$$

If we break the feedback loop, we can calculate the temperature measurement noise as:

$$T_R = \frac{D}{\gamma H} \quad (5.3.1.6.7)$$

Sections 5.3.1.6.1 to 5.3.1.6.3 detail the characterizations of the Temperature to DN gain, DN to power gain, and the PID filter terms.

5.3.1.6.1 Calculation of Temperature to DN Gain

The discussion in Section 3.2.5.2 applies to the temperature to DN gain γ of 10.8 nK/DN.

Because of the demodulation, there is an average time delay of half a 50 Hz cycle, or 10 ms, which adds a frequency dependence to the phase of the temperature to DN gain (Figure 39) represented by

$$\gamma = \frac{dDN}{dT} = 91971668e^{-0.01(i\omega)} \text{ DN/K.}$$

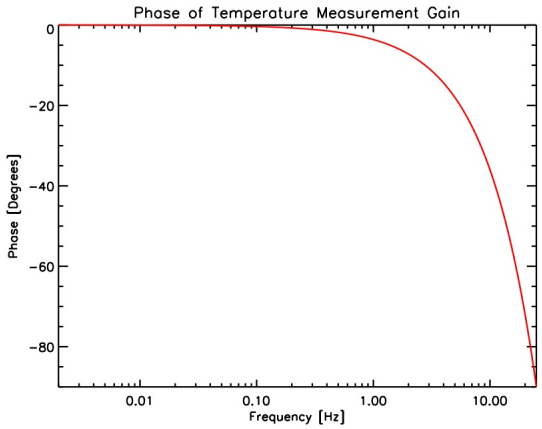

Figure 39: Phase-induced time delay of the temperature to DN gain due to demodulation of the ESR measurement.

5.3.1.6.2 Calculation of DN to Power Gain

In Section 3.2.5.2 the power application circuit of the ESR was discussed. The power applied to the ESR is:

$$P(DN) = RH\left(\frac{Vref}{R_{Top} + RH}\right)^2 \frac{DN}{64000} \quad (5.3.1.6.2.1)$$

where *RH* is the value of the heater resistance, *Vref* is the value of the 7.1 volt reference, R_{Top} is the value of the "top" resistor, and *DN* is the output data number. Dividing the output data number by 64,000 converts it to a duty cycle. An output of 64000 corresponds to a duty cycle of 100%, or 1.0, and an output of 0 corresponds to a duty cycle of 0%, or 0. The power output per DN is the frequency-independent DN to Power gain, ρ, represented by the following equation.

$$\rho = \frac{dP}{dDN} = RH\left(\frac{Vref}{R_{Top} + RH}\right)^2 \frac{1}{64000} \quad (5.3.1.6.2.2)$$

Using characterized and calibrated values of the 7.1 voltage reference, top resistor, and heater resistor from each channel, the applied power per DN for each channel is then:

ESR A: $\rho = 2.0032460$ nW/DN

ESR B: $\rho = 2.0062874$ nW/DN

ESR C: $\rho = 2.0064707$ nW/DN

5.3.1.6.3 Calculation of the PID Filter

The final gain term that we can calculate is the Proportional Integral Differential (PID) filter that acts as the controller of the feedback mechanism. PID filters involve three constant parameters, the proportional gain (K_P), the integral gain (K_I), and the derivative gain (K_D). A weighted sum of these parameters is used in maintaining the control of the feedback. For the control of the DSP, the PID filter can be approximated as:

$$H = K_P + \frac{K_I}{s \cdot \Delta t} + K_D \cdot s \cdot \Delta t \qquad (5.3.1.6.3.1)$$

where $s = i\omega$, and Δt is the discrete time step of the PID loop. For the SIM ESR the PID loop runs at 50 Hz, so Δt = 0.02 seconds. This transfer function is plotted in Figure 40 for typical PID values. Figure 41 shows the stability of the PID filter for specific values of proportional, integral, and derivative gain parameters.

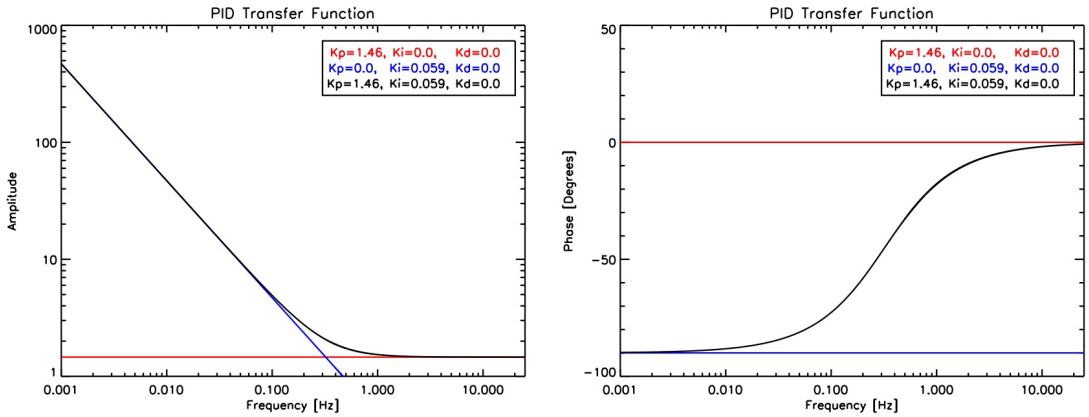

Figure 40: The amplitude (left plot) and phase (right plot) of the PID filter for three typical values of the PID control parameters.

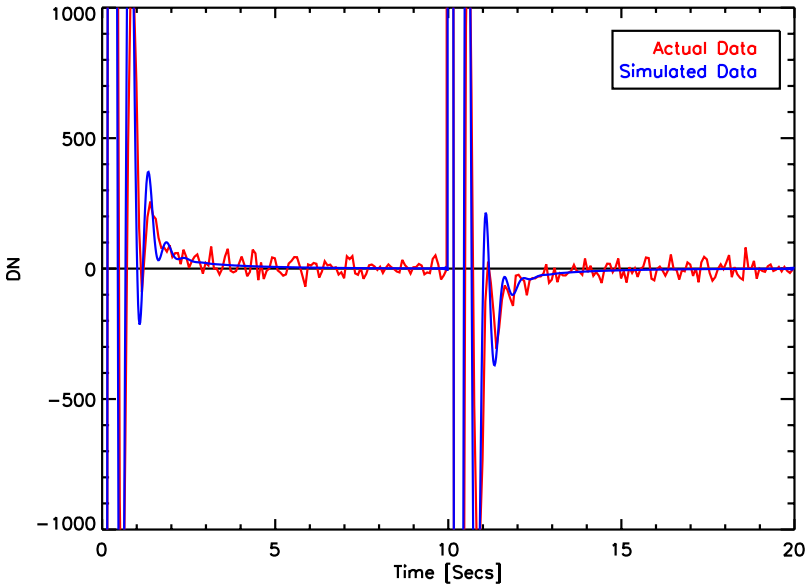

Figure 41: The response of ESR Channel B during a gain measurement with K_p = 1.46, K_I = 0.059, and K_d = 0.0. a shutter cycle time of 20 seconds and a feed forward value of 20,000.

5.3.1.6.4 Characterization of the ESR Loop Gain

We can measure the loop gain when in closed loop operation, meaning the loop gain is measured in the absence of illumination and with feed-forwards applied. The measured loop gain can be used directly, or used in concert with the knowledge of the terms described in Sections 5.3.1.6.1 through 5.3.1.6.3, to calculate the thermal transfer function, Z_H, the last unknown term. To measure the loop gain we apply feed-forwards in the absence of illumination, which simplifies to Equation 5.3.1.6.3 as shown in Section 5.3.1.6.

To obtain a measure for gain and Z_H, we set the PID control parameters K_I=K_D=0, and K_P=0.2, which simplifies the measurement by removing the frequency dependence of the PID filter (Section 5.3.1.6.3). The DSP code is designed to allow the feed-forwards to be applied with a 50% duty cycle and a variable cycle time. We use a typical feed-forward value of 10,000-20,000 and a number of different feed-forward cycle times, for instance 10, 100, and 500 seconds to obtain measurements of the loop gain over a wide range of frequencies. A FFT analysis of the resulting data and the applied feedforward is ultimately used to compute the gain, where F is the FFT of the feed-forward, and D is the FFT of the raw data numbers.

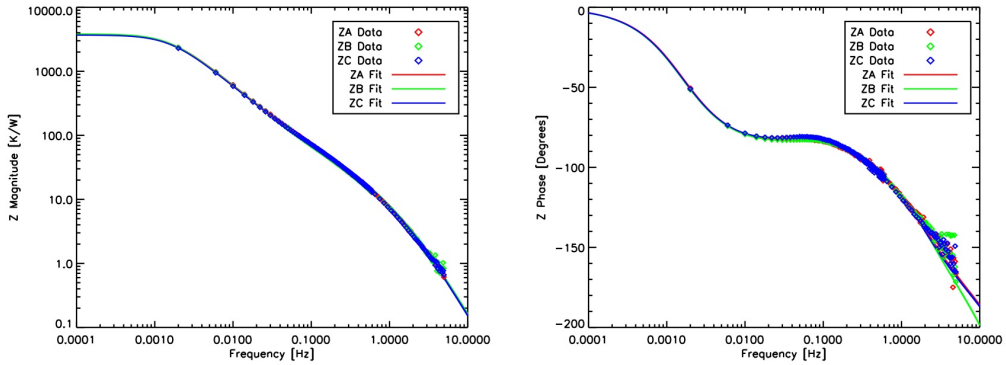

Figure 42: Characterizing the thermal transfer function based on FFT analysis of the ESR gain to various feed forward cycle times.

The amplitude and phase of the thermal transfer function, Z_H, are shown for all three ESR channels in Figure 42. The data is fit to the following function with parameter values tabulated in Table 23.

$$Z_T(s) = p_0 e^{-p_1 s} \frac{(1+p_4 s)}{(1+p_2 s)(1+p_3 s)(1+p_5 s)} \qquad (5.3.1.6.4.1)$$

Table 23: Functional fit values for the ESR thermal transfer function.

	p_0	p_1	p_2	p_3	p_4	p_5
ESR A	3753.1	0.00476	97.38	1.572	2.135	0.0818
ESR B	3824.2	0.00832	101.06	1.443	1.971	0.0791
ESR C	3690.2	0.00459	99.72	1.613	2.321	0.0867

The values in Table 23 have a physical interpretation. The first term, p_0, is the DC thermal conductivity of the bolometer to the copper block, and is 12-14% larger than what was measured during thermal testing. This difference is due to the few low frequency data points that were taken during the gain measurement where this parameter is dominant. The parameter, p_1, represents an extra 4-8 ms time delay in the feedback loop, in addition to the 10 ms from the sine wave demodulation in the DSP. The parameter, p_2, is the thermal time constant for the bolometer. The thermal time constant was also measured during the thermal testing, with results 4% larger than those obtained during the characterization of the ESR loop gain. The parameter, p_3, corresponds to a second thermal conduction time constant, which is likely time for the heat from the heater to reach the thermistor. The parameter, p_5, corresponds to a thermal time constant of unknown origin in the system. The single zero, p_4, is needed to get a good fit in the functional form of the equation, but its physical meaning is unclear.

5.3.1.7 ESR Irradiance Traceability

The measurement equation approach has allowed for the complete quantification of measurement results by detailed characterization and calibration of the individual contributions. To validate this and establish the total system uncertainty compliance, we perform a direct comparison to an L-1 Standards & Technology, Inc. cryogenic radiometer, a detector-based primary standard (radiometric scale traceable to the NIST Primary Optical Watt Radiometer) (Section 2.4.2). As an example of the process, we show here the results of the 532 nm laser validation of one the SIM ESR channel irradiance measurements to that of the direct measurement obtained by the cyrogenic radiometer in the Spectral Radiometer Facility (SRF). While the example is limited to one wavelength, one polarization, one field angle, and one SIM channel, the full calibration involved completing this measurement over many wavelengths covering the full range, both polarizations, multiple field angles, and all three SIM channels.

Figure 43 shows a plot of the L-1 Industries cryogenic radiometer signal covering a 10 minute measurement interval of a frequency and intensity stabilized 532 nm illuminating laser. The laser overfills a NIST calibrated entrance aperture to allow, after diffraction and cavity optical corrections, the irradiance (Wm-2).

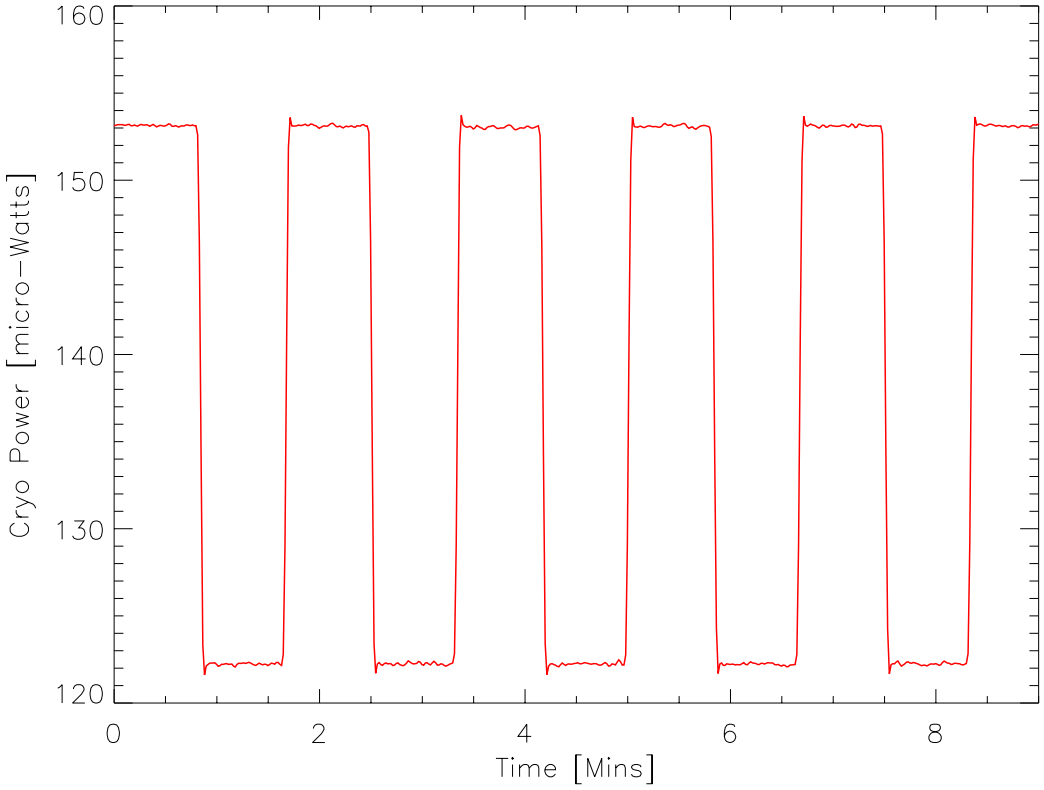

Figure 43: Directly measured 532 nm laser power with the L-1 (SI-traceable) cryogenic radiometer. For this measurement the laser was both frequency and intensity stabilized (<0.05% rms variability) and overfilled the precision entrance aperture (NIST calibrated, s < 100 ppm unc.) located directly in front of the cavity. The laser is shuttered at 50% duty cycle with a 100 second period (50 sec. open-50 sec. closed). The measured power is 30.882 ± 0.034 µW (k=1). After accounting for the slit areas and both diffraction and cavity absorptance corrections, the measured irradiance is 15.958 ± 0.017 Wm-2 (k=1).

Immediately following this irradiance calibration measurement, the laser is directed into a given SIM channel, overfilling the entrance aperture in an identical optical configuration (i.e. no changes in uniformity, f/#, spatial uniformity, or polarization).

To compare the SIM measured irradiance of this monochromatic laser with that measured by the cryogenic radiometer requires scanning the full SIM spectral passband centered at the laser wavelength (see TSIS SIM Calibration and Validation document, ref. in Table 1). Figure 44 shows the raw signal (in DN) recorded by the ESR detector during a full prism scan of the 532 nm illuminating laser. Each step in the spectrum results from an open-closed shutter cycle at each sub-pixel step. Therefore, in sub-pixel coordinates we scan the full spectral profile at this calibration wavelength. We convert this raw measurement into the laser irradiance based on the known conversion and gain factors for 532 nm. Additionally, by explicitly incorporating the sub-pixel to wavelength conversion (essentially the prism angle to dispersion relationship for each detector; Section 3.2.4) we can validate the solar spectral irradiance measurement equation (Equation 4.2.2.6).

Section 5.3.1.5 presents the final results of the ESR absolute efficiency measurements and their uncertainties. Further details can be found in the TSIS SIM Calibration and Validation Plan and the SIM Flight ESR Calibration Documents (ref. in Table 1).

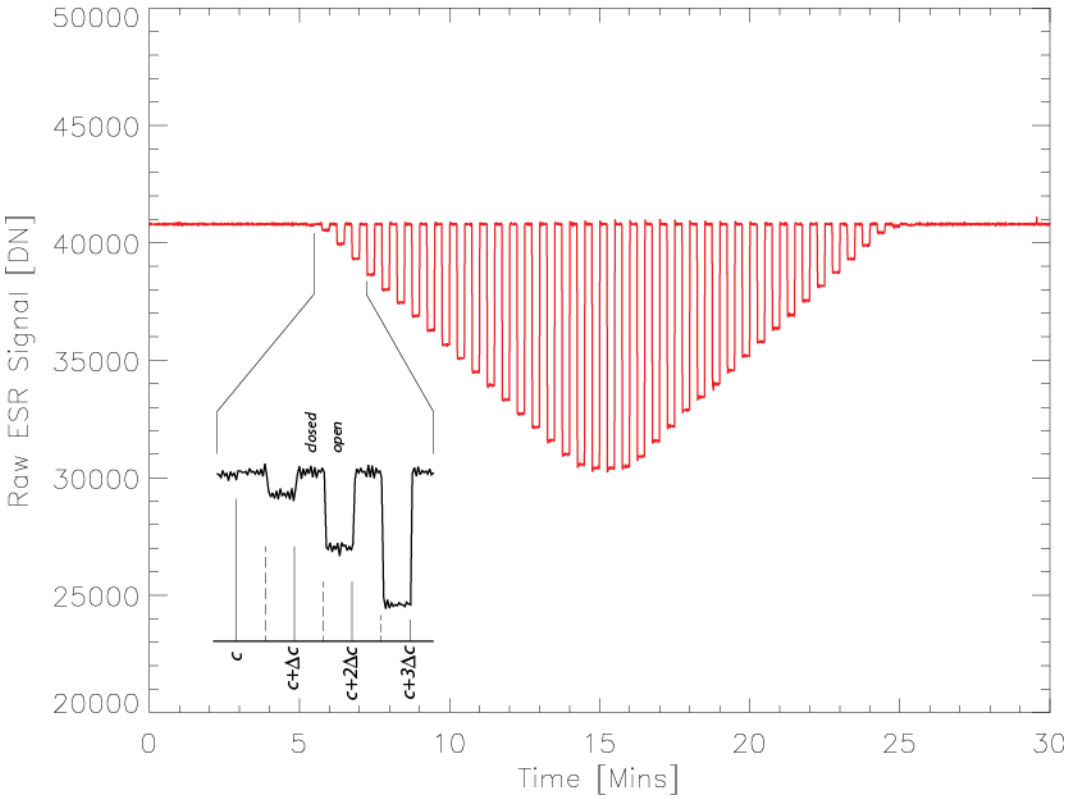

Figure 44: SIM ESR scan. For this scan, SIM is illuminated with the same 532 nm laser calibrated by the cryogenic radiometer. To cover the full spectral response, the prism angle is scanned across the sub-pixel range where there is signal on the ESR. The inset shows the sub-pixel steps (Dc=12) as a function of shutter cycle; each sub-pixel position includes an open and closed shutter state. The optical signal appears as a decrease in DN's from the initial power balance due to pulse wave modulation (PWM) power decrease to match optical power increase on bolometer to maintain balance.

5.3.2 Instrument Line Shape

Validating the solar spectral irradiance measurement equation in the approach described in Section 5.3.1.7 requires generating the SIM spectral line shape at 532 nm. This is shown in Figure 45 where the data from Figure 44 has been converted to power (in W) as a function of SIM wavelength. As mention earlier, ideally this function can be measured directly by fixing the sub-pixel at given value and scanning the laser over all wavelengths within the exit slit passband. By intensity stabilizing a fixed wavelength laser, we can convert from index of refraction coordinates (through the angle defined by the sub-pixel) to dispersion coordinates (in wavelength). Here, the laser spectral linewidth is narrow (< 1 nm), so the spectral shape of this curve is due solely to the instrument. We call this curve the instrument line shape (ILS).

The full ILS analysis accounts for the true laser linewidth in a deconvolution algorithm to remove any influence of the finite laser bandwidth across the full SIM passband. The specific shape of this curve is determined by the specific parameters and aberrations of the SIM optics. The spectral centroid of the ILS is compared against the actual laser wavelength, and so provides a check of the wavelength scale of the instrument. The total area of the ILS

can be directly compared to the irradiance measured by the cryogenic radiometer; this is how we verify the radiometric scale of the instrument. This was done for the data in Figure 45, however since we are illuminating with a monochromatic laser, all conversion and gain factors are held constant at their 532 nm values. Performing this integration of the spectral profile yields a value for the irradiance of the laser (Wm-2) that can be compared directly with the value measured by the cryogenic radiometer. For this example at 532 nm, the SIM measured irradiance agrees with the cryogenic radiometer measured irradiance to within 700 ppm.

In total, line shapes for 46 band central wavelengths were generated across the SIM spectral range. The central wavelengths and ILS for these are summarized in Figure 46. See the TSIS SIM Calibration and Validation plan contain (ref. in Table 1) for further details.

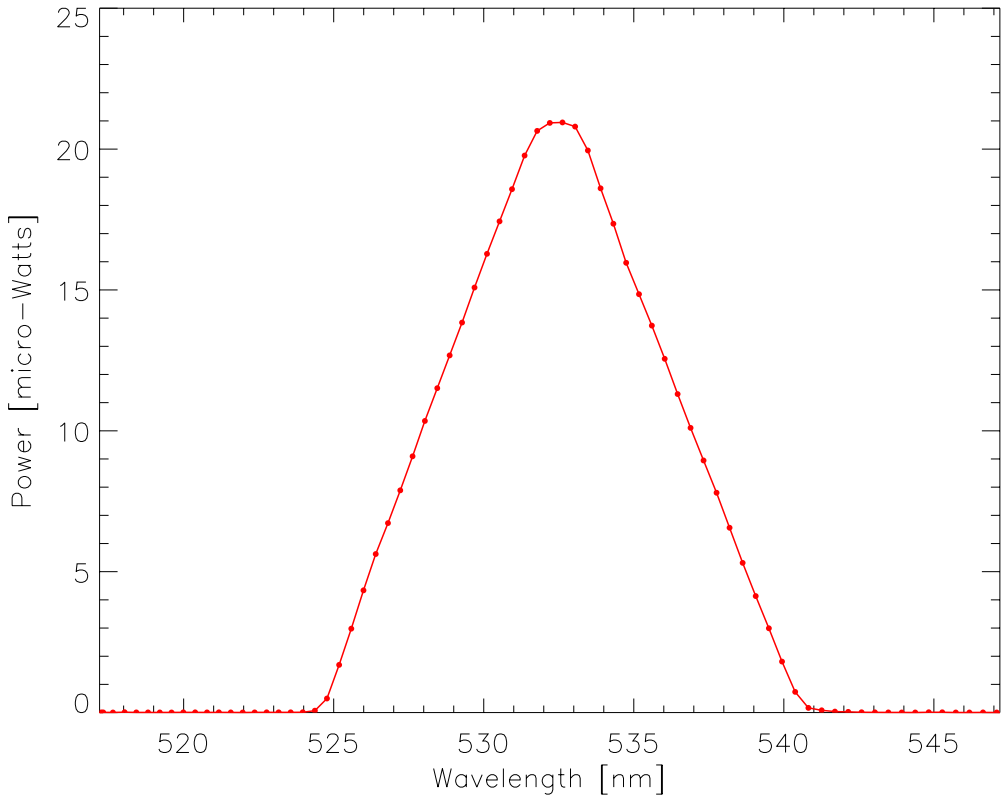

Figure 45: The result of the conversion of the raw DN vs. sub-pixel data using the SIM measurement equation (Equation 4.2.2.6). The conversion results in the spectral power as a function of wavelength (Wnm^{-1}), the spectral response function, for SIM at 532 nm. Integrating this spectrum with wavelength allows for a direct power comparison (W) with the cryogenic radiometer. For this measurement, SIM yields an irradiance of 15.969 ± 0.024 Wm-2 (k=1) (~700 ppm higher than the cryogenic radiometer value of 15.958 Wm-2, validating the measurement equation at the 0.1% level.)

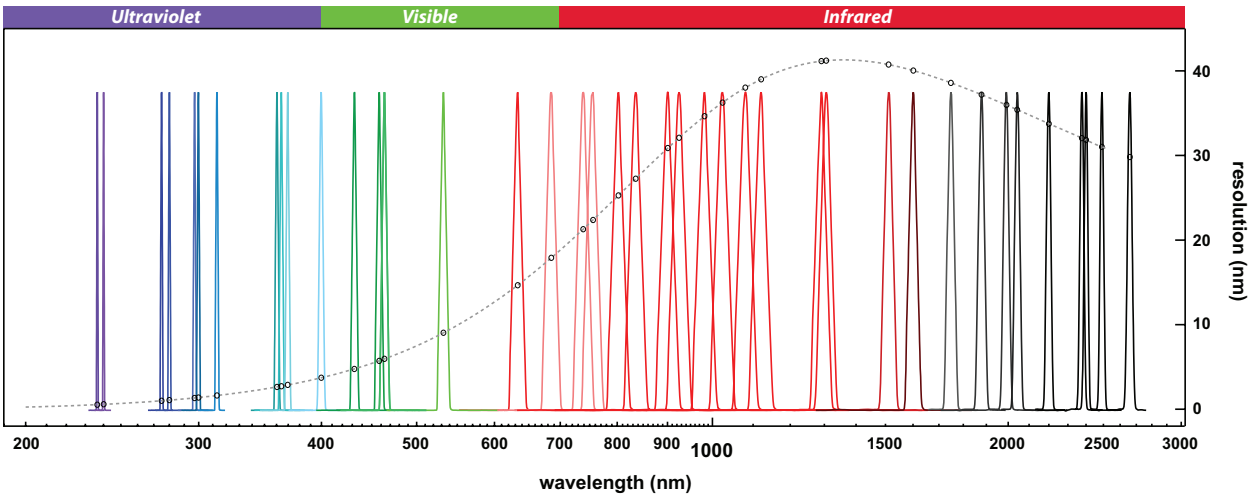

Figure 46: A summary of the locations and instrument line shapes for the 46 different measured spectral response functions across the SIM spectral range. The dashed grey curve is the results from the dispersion model and the measurements are at band centers (open circles).

5.3.3 Entrance Slits

Accurate measurements of the entrance slit areas are needed to determine the radiant flux into the instrument, and accurate measurements of the entrance and exit slit widths are needed to determine the instrument bandpass and diffraction correction (Section 5.3.5). The measurements of the entrance slits (nominally 6.5 mm in length by 0.3 mm in width) and the ESR exit slits for each channel (nominally 7.5 mm in length by 0.3 mm in width), calibrated at NIST, have 1-sigma errors on the order of 10^{-5} mm (Table 24).

The thermal expansion coefficient (CTE) of the SIM slit and of brass metal has been measured at LASP to part per million (ppm) levels over a broad range in temperatures (-160 °C to -40 °C and to even lower values for the brass). A 3rd order polynomial fit to the brass CTE was allowed to float in offset only during a least squares fitting algorithm to the CTE measurements of the SIM slit. The standard deviation of the fit is added in quadrature to an estimated error in temperature of 1.1 °C to determine an overall error.

Appropriate thermal corrections in slit area and width are applied to the flight data in post-processing based on temperature measurements monitored in-flight with a thermistor bonded nearby.

Table 24: TSIS SIM entrance aperture measurements and uncertainties.

Slit	SN	Length	Width	Area	Uncertainties		
					NIST (k=2)	NIST (k=1)	LASP (k=1)
		[mm]	[mm]	[mm^2]	[mm^2]	[ppm]	[ppm]
SIM A	38	6.50132	0.29904	1.94442	1.47E-03	378	162
SIM B	39	6.49822	0.29924	1.94431	1.30E-03	334	154
SIM C	42	6.50051	0.29653	1.92742	1.49E-03	387	94

5.3.4 Prism

5.3.4.1 Transmission

Figure 47 shows the results of the full spectrum transmission measurements for both laser polarizations and the corresponding derived second surface Aluminum reflectivity. The aluminum reflectivity is determined from the removal of the Fresnel reflection contributions to the p-polarized transmission measurements (p-polarized data is used since the reflections are much smaller than for the s-polarized data). Because the of the prism refraction

geometry, the internal reflection off of the silica-aluminum interface is nearly normal and therefore is polarization independent. The second surface aluminum reflectivity can then be compared to a calculation based on real and complex refractive index data for the fused silica-Aluminum interface and shows excellent agreement to the derived reflectivity (Figure 22, right). Since we do not explicitly account for the surface scattering and the bulk absorption losses in the reflectivity derivation, the agreement shows that these contributions are indeed negligible in the overall fit (as expected from super-polished, high purity Suprasil 3001).

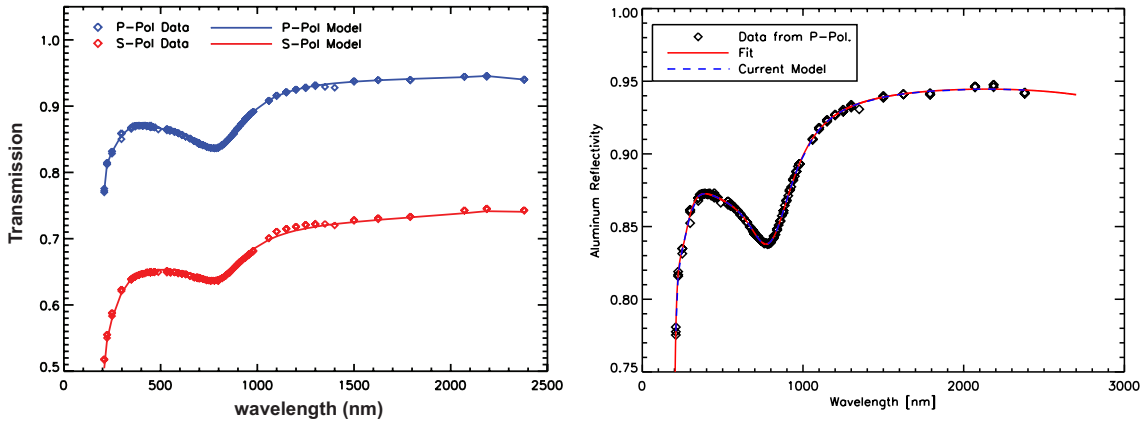

Figure 47: Results of polarization dependent prism transmission measurements for s- and p-polarized laser light. Figure on right shows the derived second-surface aluminum reflectivity derived from the p-polarized transmission data and removal of the calculated Fresnel reflection contributions.

The final ESR transmission values for all TSIS SIM prisms are shown in Figure 48. These values were calculated based on the clear aperture mapping data (using the central 6 x 6 grid points, i.e. excluding outside perimeter points in the map). The plot shows the average and the standard deviation of the average (over 36 points) of the polarization average transmission. All data was collected in air and therefore requires slight conversion corrections for application to vacuum, predominantly affects the Fresnel reflection contributions since the external medium index is not unity (as in vacuum). For this we use the *Edlen* [1953] published air index data. Also note that several points in the near infrared have been excluded due to the potential for slight interferences with atmospheric water absorption variability over the course of the measurements.

Based on the unit level measurement geometry for the prism transmission at the ESR detector location, the relative standard uncertainties range in value from 600 ppm in the UV and near IR with values ≤ 100 ppm throughout the visible. These are evaluated as a standard deviation of the average of measurements of I/I_o ratios of the 6 x 6 grid pattern The result is then polarization averaged and the separate polarization standard deviation values propagated to generate a standard deviation of the average (bottom plot, Figure 48). See the TSIS SIM Calibration and Validation plan contain (ref. in Table 1) for further details.

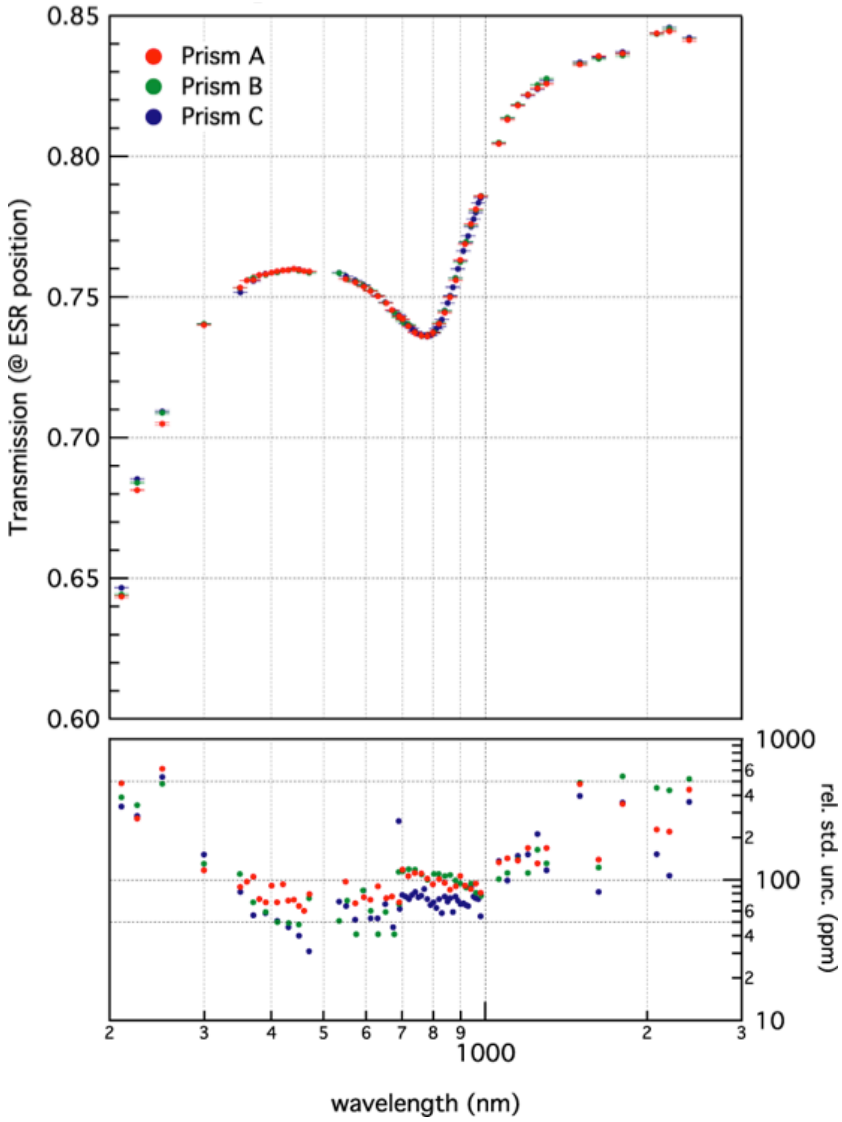

Figure 48: Results of prism transmission measurements for all 3 channels across the spectral range of the SIM instrument (top) and the relative standard deviation (in ppm) of the measurements (bottom).

5.3.5 Diffraction

The dominant source of diffraction loss is from the physical size of the aperture and it has two sources. First, light is lost as it comes into the prism due to diffraction from the aperture plate. This loss has a linear dependency with wavelength increasesing from 0.5% (in the UV) to 6.4% at the longest near-IR wavelength (~ 2400 nm). The second source of light loss occurs as light exits the prism and clips the edge of the aperture. This second source add approximately 2% more diffraction loss. The total diffraction loss over the full spectral range is shown in Figure 48.

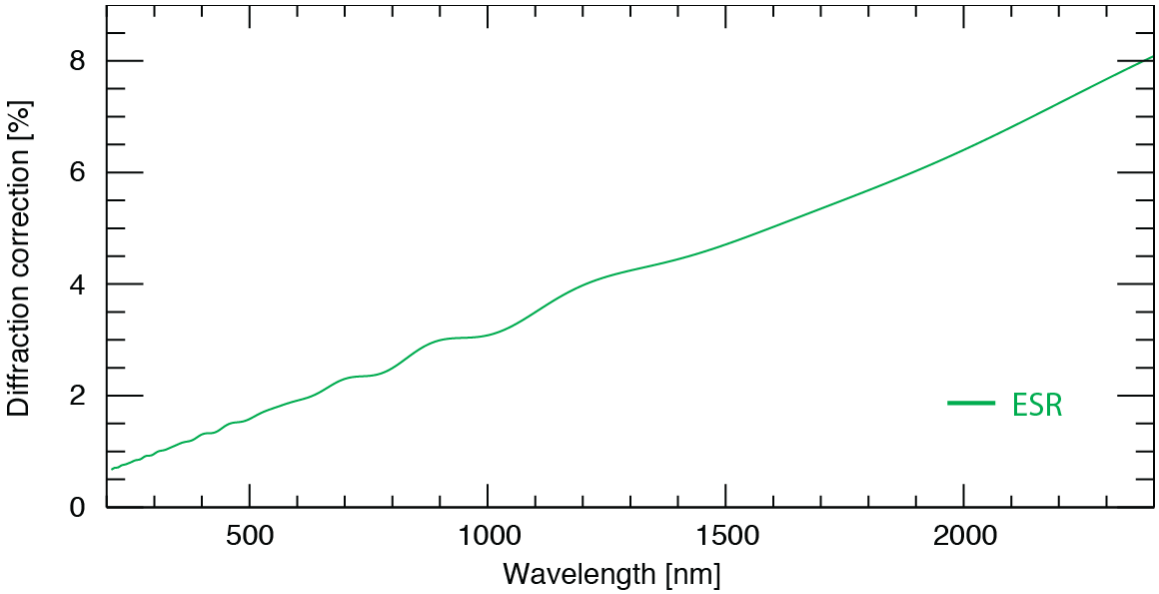

Figure 49: TSIS SIM diffraction loss (in %) over the full spectral range.

5.3.6 ESR to Photodiode Calibration

The same spectral scans (see Sections 5.3.1.7 to 5.3.2) are completed for all the photodiode channels to generate similar spectral response profiles that can be used to verify the calibration of the diode measured irradiance with the ESR. In contrast to the ESR scans, the photodiode spectral scans require much less time to complete since we do not have to cycle the shutter and the signal integration at each pixel step is typically around a second. This affords the opportunity to generate many spectral profiles to quantify the wavelength scale and off-axis performance. Figure 50 shows the 532 nm laser spectral profile measured with the Visible photodiode after conversion and gain factors have been applied. Note here that the signal intensity is in photocurrent (μA). The data number (DN) conversion for the photodiode detectors is accomplished through the dual-slope voltage determination (Section 3.2.11.1) based on the 7.1V reference. The measured voltage is then converted to a photocurrent through the specific photodiode transimpedence amplifier current-to-voltage conversion (namely, the precision feedback resistor, R_f). To convert the measured photocurrent to power (in W) requires accurate knowledge of the photodiode spectral radiant sensitivity, $R(\lambda, T)$, as a function of wavelength and temperature (units: Amps W^{-1}). The photodiode radiant sensitivity is a strong function of wavelength and temperature and requires extensive calibration to maintain accurate correction values. On-orbit, the radiant sensitivity is subject to further changes due to the constant exposure to protons and other damaging radiation.

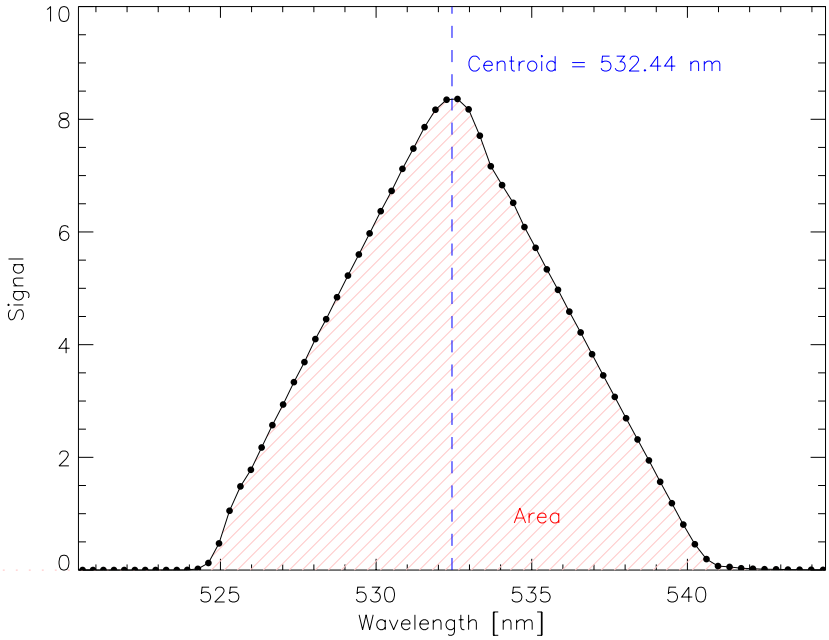

Figure 50: The SIM instrument line shape (ILS) measured at 532 nm for the visible photodiode detector. For this measurement, the same intensity stabilized laser that was measured with the ESR (Section 5.3.1.7) is used to quantify the spectral response function for the visible diode. For the photodiodes, the DN's are converted into a photocurrent (μA shown here). The direct comparison of the integral of this response function (in Amperes) with the ESR response function (in Watts) allows for accurate determination of the radiant sensitivity (in Amp W^{-1}) of the detector at this wavelength. The radiant sensitivity, among other factors, is contained within the photodiode gain factor, G. The temperature dependence of gain, $\overline{G}(\lambda,p,T)$, can also be uniquely quantified by response measurements at various diode temperatures over the operational range.

Both in pre-launch calibration activities and during on-orbit calibration, the photodiode radiant sensitivities are determined by direct comparisons with the ESR measured irradiances and are used to correct the gain factor $\overline{G}_{PD}(\lambda,p,T)$ in the photodiode measurement equation. For example, the integral of this 532 nm visible photodiode spectrum is now compared directly to the ESR measured irradiance, namely

$$I_0 = \frac{\int DN_{ESR}(c)dc}{AD_{ESR}(\lambda_0)T_{ESR}(\lambda_0,p)\overline{G}_{ESR}(\lambda_0,p)\int M_{ESR}(c)dc} = \frac{\int DN_{PD}(c')dc'}{AD_{PD}(\lambda_0)T_{PD}(\lambda_0,p)\overline{G}_{PD}(\lambda_0,p)\int M_{PD}(c')dc'} \qquad (5.3.6.1)$$

Therefore,

$$\overline{G}_{PD}(\lambda_0,p) = \frac{1}{\overline{G}_{ESR}(\lambda_0,p)}\left[\left(\frac{D_{ESR}(\lambda_0,p)}{D_{PD}(\lambda_0,p)}\right)\left(\frac{T_{ESR}(\lambda_0,p)}{T_{PD}(\lambda_0,p)}\right)\left(\frac{\int M_{ESR}(c)dc}{\int M_{PD}(c')dc'}\right)\left(\frac{\int DN_{PD}(c')dc'}{\int DN_{ESR}(c)dc}\right)\right] \qquad (5.3.6.2)$$

Note here, that even though we are dealing with the same wavelength, λ_0, in the ESR to photodiode comparison, the diffraction and transmission values are different because the differences in optical and refractive geometries between the ESR and photodiode detectors. For example, at 532 nm, the prism incidence angle is different (i.e. different sub-pixel for λ_0; $c \neq c'$) for measuring this wavelength on the ESR and measuring the same wavelength on the visible photodiode, therefore the Fresnel reflection-transmission coefficients are different and produce different overall transmission values for a given polarization.

5.3.7 Sub-pixel to Wavelength Calibration

The resulting mapping of CCD subpixel to wavelength scale for all channels for direct laser calibrations in LASP SRF using the SIRCUS laser systems results in a combined standard deviation (239 – 2400 nm) of 2 subpixels rms error, well within the requirement of ±5 subpixel error to meet the <0.1% wavelength scale fit uncertainty. The result shows 5 separate calibration campaigns spanning 3 years and includes multiple off-axis pointing angles between ±20 arc-min in the dispersion direction. Figure 15 shows the final subpixel to wavelength relationship over the useable spectral regions for each detector: ESR (full 200-2400 nm); UV diode (200-320 nm); Vis diode (300 – 950 nm); IR diode (900-1670 nm). The solid points in the figure are the SRF measured data and the solid lines are the spectral dispersion model derivations that resulted in the minimization of the subpixel scale errors. Further details are provided in the TSIS SIM Calibration and Validation Plan (ref. in Table 1).

5.3.8 Cruciform (Pointing) Mapping

Ground calibrations of the alignment of the Fine Sun Sensor (FSS) with the instrument bore sight have been performed using a heliostat under vacuum conditions. The FSS is progressively pointed off the center of the Sun in the heliostat set up in 5 arc minute increments, in both the cross-dispersion and dispersion directions, while the photodiode signal is monitored. The point at which the sunlight falls off the photodiode detectors and the signal goes to zero is recorded with respect to FSS angle. Periodic on-orbit cruciform mapping (3.2.12.4) will be performed to monitor, and correct for, changes in the alignment of the FSS and the instrument bore sight.

5.4 SIM Flight Calibrations

5.4.1 Prism Degradation

Discussed in Section 7.2.

5.4.2 ESR Servo Loop Gain

The servo open-loop gain, *G,* is the end-to-end complex gain of the control loop at the shutter fundamental. The loop gain is known from circuit analysis and pre-flight calibrations, but will be periodically recalibrated in flight. A test amplitude, *F,* is added to the loop by ground command at the feed forward junction as shown in Figure 38. The fundamental response at the output is *D* and the loop gain is calculated as (see discussion in Section 5.3.1.6.4):

$$\boldsymbol{G} = -\gamma H \rho Z_H = \frac{F}{D} - 1 \qquad (5.4.2.1)$$

6 Uncertainty Estimates

All calculations, which involve physical quantities with uncertainties, will incorporate the correct propagation of those uncertainties into the calculated results, on the assumption that the measurement uncertainties are independent. Moreover, the assumption of independence of measurement uncertainties will be subject to validation by separate and on-going statistical analyses, as a component of the quality assurance plan (Section 8.4 below).

6.1 TIM

Since TIM is a primary radiometer, its uncertainty in measuring the Total Solar Irradiance (TSI) is estimated as the root sum square of the individual uncertainties of the components of the measurement Equation 4.3.1.3. We will consistently quote "relative standard uncertainties" in ppm (10^{-6}). "Relative" refers to fractional uncertainty, standard means standard deviation, σ, and uncertainty means the lack of knowledge of the parameters and hence of the determined irradiance. The uncertainty budget for the design of TIM is presented in Table 25.

Table 25: TIM Uncertainty Budget Goals		
	Size of the effect, PPM	Uncertainty, PPM
Inverse Square	+33116,-33764,188 orbit	5
Doppler	43	5
Shutter Waveform	100	10
Aperture	1,000,000	60
Optical Absorber	100	20
Equivalence ratio, Z_H/Z_R	100, AC	60
Servo Gain	3000	10
Standard Volt + DAC	2,000,000 (V^2)	10
Standard Ohm + Leads	1,000,000	10
Dark Signal	1800	10
Total RSS		**90**

For a squared factor such a V^2, the relative uncertainty in the irradiance is $2\delta V/V$. For the equivalence ratio and other factors, one must propagate the uncertainties in the parameters of each model. Table 26 summarizes in some detail the propagation of parameter and measurement uncertainties to the final uncertainty in the irradiance.

In the characterization of TIM, the equivalence ratio is the only quantity that comes from theory rather than experiment. Section 3.1.7 describes the theory of the overlap integrals need to calculate the ratio and Section 5.1.5 describes the ground calibrations of some of the parameters. To calculate the uncertainty in the ratio, one propagates uncertainties in the parameters of the model through the equation defined in Section 5.1.5; and some early examples of such calculations are shown in Figure 51.

Table 26: Propagation of Uncertainties for TIM: Absolute Uncertainties in ppm					
Ephemeris Correction	Value	Uncertainty	Units	Net ppm	Notes & Comments
1 AU, delta R, inverse square	33,537	75	ppm	0.1	published 3 sigma
velocity: Doppler	57	0.1	ppm	0.7	published 3 sigma
δEphemeris				**0.7**	
Shutter waveform, Y					
Shutter frequency	0.01	0	Hz		
Rise time	7	1	msec	0.0023	
Delay	9.8	2	msec	0.1579	
Timing Jitter and drift	0	2	msec	0.00	
Leakage fraction		1	ppm	1	goal
Digital Timing error		1	μsec	0.00	
δShutter				**1.01**	
Aperture, Ap					
Area	50.03495	6.61e-4	mm^2		*from NIST area measurements (example

					given for aperture A)
Stage position reading		4.36e-4	mm^2		
Edge location of imaging		1.05e-4	mm^2		
Thermal		2.01e-4	mm^2		
Geometry		2.12e-4	mm^2		
δ Aperture Area				23	
Edge Scatter			ppm	16.8	* Harber et al., 2006
Pressure changes for vacuum operations			ppm	<1	
δAperture				**28.4**	
Diffraction	452		ppm	46	* Harber et al., 2006 and using a NIST-assigned uncertainty of 10% of value.
δDiffraction				**46**	
Cavity Optical Absorption, α	999818		ppm		
Cavity Optical Reflection, 1-α	182		ppm		* average of TSIS/TIM reflectance measurements weighted by the solar spectrum
Glory/TIM Flight Cavity Reflectance Measurements					* reported values are for 532 nm (Glory/TIM)
Laser stability		5.45	%		
Laser polarization orientation		3.43	%		
Cone centering		7.74			
Orientation of cone - tip/tilt		5.78			
Orientation of cone - azimuthal		5.44			
Diode linearity		1	%		
Detector position – perpendicular		2.78	%		
Detector position – distance to cone		3.22	%		
Detector rotation - azimuthal		0.03	%		
Detector rotation - vertical		2.05	%		
Stray light		0.88	%		
Baffle position		0.01	%		
Chopper Speed		0.01	%		
Photodiode Noise		0	%		
Beam position in chopper		0.55	%		
Operator		0.11	%		
Repeatability		3.64	%		
δCavity Reflectance Measurements		14.2	%		
Average over solar spectrum		10	%	6	
δAbsorption				**35**	
Equivalence Ratio, Z_R/Z_H	782		ppm	43	*from empirical fit of flight data
δEquivalence Ratio				**43**	
Standard Volt					
Voltage	7.1		V		
HP3458A + Fluke + NIST		8	ppm	8	
~20 year stability against witness		5	ppm	5	
Thermocouple voltages	1	1	μV	0.28	

Coupling, stray electronic		10	ppm	10	
δStandard Volt				**14**	
Pulse Width Linearity	800	3	ppm	3	
δPulse Width Linearity				**3**	
Standard Ohm (heater)	520		Ω		
HP 3458A + Tegam SR104		10	ppm	10	
Coupling, stray electronic		15	ppm	15	
Lead resistances	0.062	0.01	Ω	19.23	Resolution is 1 mΩ
Lead Temp. transfer from calibration		2	K	1.62	
TCR of leads	0.68		%/K		
TCR of heater	15	3	ppm/K		
Heater Temp., thermistor aging	30	0.5	deg C	1.50	Cone is regulated
Aging against witnesses		5	ppm	5	Estimate
δStandard Ohm				**26.4**	
Dark Signal Correction	1645	14	ppm	14	*lab measurements relative to cryogenic target
δDark Signal				**14**	
Open Loop Servo Gain G	2115		ppm	**<1**	
Pointing corrections	100		ppm	**10**	
Measurement Noise				**4**	
Sampling Uncertainty			ppm	**12**	analysis
Total Uncertainty				**85.8**	**ppm, 1 σ**

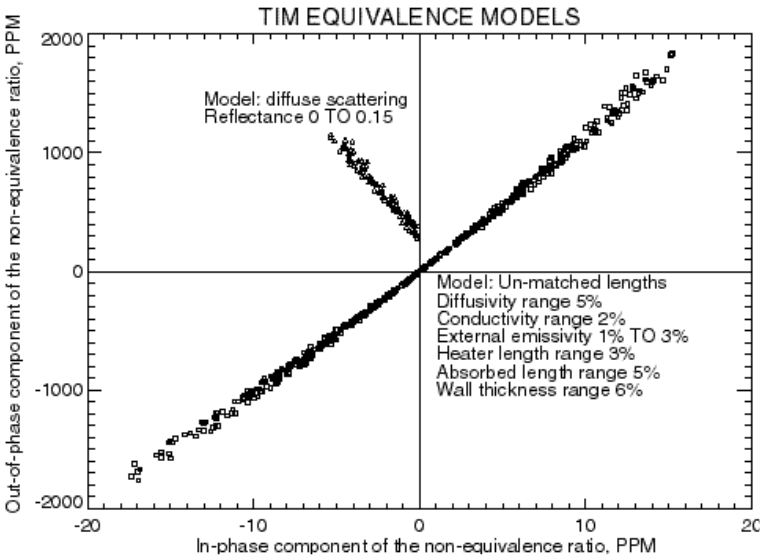

Figure 51: Typical Monte Carlo Study of the Equivalence Ratio

6.2 SIM

The accuracy for determining solar spectral irradiance with the SIM instrument follows from the uncertainty in the individual terms of the SIM measurement equation, for which the Data Number version was derived in Section 4.2.2. In this section, we provide the formula for propagating error through the measurement equation, and ultimately present a table of the SIM uncertainty budget based on the calibrations discussed in Section 5.

Table 27 lists the symbols, their definitions, and units used in the error propagation equations for the ESR, photodiodes, and correction factors.

Table 27: Symbols, definitions, and units used in the SIM error propagation equations.

Symbol	Interpretation	Units
P_{PD}	Optical power measured by the SIM photodiode detectors	Watt
V_7	Dual-Slope ADC reference voltage (de-integration V)	Volts
M	Fixed integration counts – 0.5 sec (1e6) or 1.5 sec (3e6)	unitless
N_{signal}	Measured counts for V_7 de-integration with shutter open signal+dark)	unitless
N_{dark}	Measured counts for V_7 de-integration with shutter closed (dark only)	unitless
R_f	Feedback resistance of the photodiode transimpedance amplifiers	ohms
λ_s	The set point wavelength (nm)	nm
t	Time since launch	Days
T	Temperature (measured component by component)	°C
E_{ESR}	The spectral irradiance as measured by the SIM ESR	W $m^{-2}nm^{-1}$
M	Full scale PWM data numbers (64000)	unitless
V_7	Voltage of LTZ1000 voltage reference	volts
R_H	Resistance of the ESR heater	ohms
R_s	Resistance of the ESR series resistor (includes leads)	ohms
$\tilde{Z}_H$	Electrical heater thermal transfer function	Kelvin/Watt
$\tilde{Z}_R$	Radiative thermal transfer function	Kelvin/Watt
$\tilde{G}(t)$	Open loop gain on the ESR servo loop	unitless
$\vec{\tilde{p}} \cdot \vec{D}$	Fundamental frequency component of the measured data numbers	unitless
$\vec{\tilde{p}} \cdot \vec{Q}$	Fundamental frequency component of the shutter waveform	unitless
A_{slit}	Area of the spectrometer entrance slit	m^2
$\alpha(\lambda)$	Absorbance of the bolometer (total)	Unitless
$T(\lambda)$	Preflight transmission of the prism	unitless
$\Phi(\lambda)$	Diffraction correction (full optical path)	unitless
$S(\lambda_s, \lambda)$	Instrument profile function at the set wavelength as a function of wavelength	nm
$\kappa(\lambda)$	Wavelength dependent degradation attenuation factor for prism transmission	unitless
$C(t)$	Time dependent effective column thickness of absorbing material	unitless
f_{1AU}	Solar distance correction factor (sun-spacecraft)	unitless
$f_{Doppler}$	Doppler attenuation factor correcting for spacecraft velocity	unitless
f_{FOV}	Field-of-view correction factor (pointing)	unitless
f_{Deg}	Degradation correction factor	unitless

The measured ESR power at the fundamental shutter frequency is represented by Equation 6.2.1.

$$\tilde{P}_{ESR} = \frac{1}{M} \frac{V_7^2 R_H}{(R_H + R_S)^2} \left\{ \frac{1 + \tilde{G}}{\tilde{G}} \frac{\tilde{Z}_H}{\tilde{Z}_R} \right\} \frac{\vec{\tilde{p}} \cdot \vec{D}}{\vec{\tilde{p}} \cdot \vec{Q}} \qquad (6.2.1)$$

Converting ESR power to irradiance is represented by Equation 6.2.2, where the components of the correction factor, f_{cor}, are defined in Equation 6.2.3.

$$E_{ESR}(\lambda_s,t) = \frac{\tilde{P}_{ESR}}{A_{slit}\int \alpha(\lambda)\Phi(\lambda)T(\lambda)S(\lambda_s,\lambda)d\lambda} \cdot \left(\frac{1}{f_{corr}}\right) \tag{6.2.2}$$

$$\frac{1}{f_{corr}} = \left(\frac{1}{f_{1AU}} \cdot \frac{1}{f_{doppler}} \cdot \frac{1}{f_{FOV}} \cdot \frac{1}{f_{Deg}}\right) \tag{6.2.3}$$

Error propagation equations for ESR irradiance and correction factors are provided in Equation 6.2.4 and Equation 6.2.5, respectively. Independence for the various terms is assumed.

$$\sigma_E^2 = E^2 \cdot \left[\frac{\sigma_P^2}{P^2} \cdot \frac{\sigma_A^2}{A^2} \cdot \frac{\sigma_\alpha^2}{\alpha^2} \cdot \frac{\sigma_\Phi^2}{\Phi^2} \cdot \frac{\sigma_T^2}{T^2} \cdot \frac{\sigma_S^2}{S^2}\right] \tag{6.2.4}$$

$$\sigma_{f_{corr}}^2 = f_{corr}^2 \cdot \left[\frac{\sigma_{f_{1AU}}^2}{f_{1AU}^2} \cdot \frac{\sigma_{f_{doppler}}^2}{f_{doppler}^2} \cdot \frac{\sigma_{f_{FOV}}^2}{f_{FOV}^2} \cdot \frac{\sigma_{f_{Deg}}^2}{f_{Deg}^2}\right] \tag{6.2.5}$$

The measured photodiode power is represented by Equation 6.2.6.

$$P_{PD} = \frac{V_7}{M} \cdot \left[\frac{N_{signal} - N_{dark}}{R_f}\right] \tag{6.2.6}$$

Converting photodiode power to irradiance is represented by Equation 6.2.7, where the components of the correction factor, f'_{corr}, are different from the correction factors in the ESR measurement equation due to different degradation and FOV correction factors.

$$E_{PD}(\lambda_s,t) = \frac{P_{PD}(t)}{A_{slit}\int R(\lambda)\Phi(\lambda)T(\lambda)S(\lambda_s,\lambda)d\lambda} \cdot \left(\frac{1}{f'_{corr}}\right) \tag{6.2.7}$$

The error propagation of the photodiode irradiance and correction factors would be accomplished in a similar manner to the ESR (see Equations 6.2.4 and 6.2.5).

The SIM measurement uncertainty budget allocation is summarized in Table 28. This table shows the correction. the magnitude of the effect, and uncertainty that remains after the correction is made. Unlike TIM, for SIM we apply a maximum uncertainty allowable at either the component or instrument level contribution to the measurement equation. Figure 52 shows the absolute irradiance calibration obtained from an instrument-level full wavelength validation of the SIM by the NIST-traceable cryogenic radiometer is within 0.2% across the spectral range of the instrument.

Table 28: SIM instrument error budget allocation listed by type and origin: Origin is defined by instrument level, component level, or analysis level. The total root sum square of allocated uncertainties is 2000 PPM (0.2%).

Correction	**Origin**	**Size [PPM]**	**1σ [PPM]**
Distance to Sun, Earth, & S/C	Analysis	33,537	0.1
Doppler Velocity	Analysis	43	1
Pointing	Analysis	0	100
Shutter Waveform	Component	100	1
Aperture (slit area)	Component	1,000,000	200
- Diffraction (UV-IR)	Component	5,000 – 62,000	500
Prism Transmittance (IR-UV)	Component	230,000-450,000	1,000
ESR Efficiency	Component	1,000,000	1,000
Standard Volt + DAC	Component	1,000,000	50
- Pulse Width Linearity	Component	0	50

Standard Ohm + Leads	Component	1,000,000	50
Non-Equivalence, Z_H/Z_R-1	Instrument	2,000	100
Instrument Function Area	Instrument	1,000,000	1,000
Wavelength	Instrument	1,000,000	750
Servo Gain	Instrument	2,000	100
Dark Signal	Instrument	0	100
Scattered Light	Instrument	0	200
Noise	Instrument	-	100
Total RSS			2000

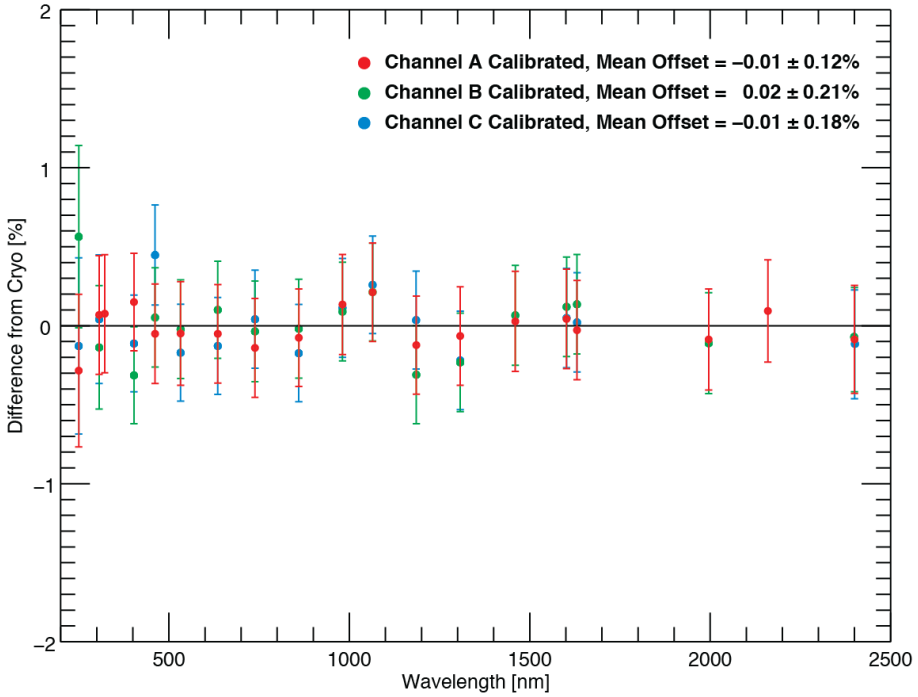

Figure 52: SIM instrument-level full wavelength SIM to cryo-validation result.

7 Degradation Correction

The sensitivities of all instruments on TSIS are assumed to degrade as the mission progresses. There is a general assumption, but no guarantee, that the degradation will be small and that the sensitivity will monotonically decrease with time. There is also a basic assumption that a primary cause of the decreased sensitivity is related to the exposure to the harsh radiation environment from the Sun, although other changes that are strictly time-dependent, or aging effects, must also be considered. Changes in the instrument that may increase sensitivity cannot be ruled out, and the degradation analysis does not preclude this condition. That is, the analysis is open to the possibility that aging effects improve sensitivity, or that radiation and exposure may in fact "scrub" surfaces and improve their throughput.

The science team, and in particular the instrument scientists, will examine all relevant information, including extensive pre-launch characterizations and in-flight calibrations to derive appropriate degradation corrections. There will not be a preordained algorithm for determining degradation with time. Experience on previous missions including SORCE indicates that this process will take on the order to three to four months, but will then be an on-going process throughout the mission.

The technique used to understand instrument degradation for the TSIS TIM and SIM instruments is to have completely independent instrument channels, to use each channel with a varying duty cycle, and then to compare their observations of the Sun. The degradation in the instruments is assumed to be primarily dependent on the exposure of the optics and detectors to solar radiation. If the exposure times are dramatically different, say one to one hundred, the ratio of the measurements will change with time. With the assumption that exposure-dependent degradation will proceed proportionally faster for the normal channel, an exposure-dependent model of degradation is developed.

Unraveling details in the time-dependent degradation is a challenging problem, and will require refinements throughout the mission. The TSIS science team, particularly the TIM, and SIM instrument scientists, will devote considerable effort toward these analyses. A proposed model for monitoring and correcting each TSIS SIM observation for degradation is presented in Section 7.2. This parameterization assumes some degradation with age and with use (exposure to the Sun), and would apply, for instance, to materials and coatings used on the optics. It also allows for rapid, exponential degradations during initial use, such as might be expected as surface contaminants polymerize. Our experience with SORCE SIM resulted in instrument design changes to reduce sources of contamination and by selecting materials (e.g., NiP) less sensitive to deterioration. The model for monitoring and correcting each TSIS TIM observation for degradation is unchanged from SORCE TIM and presented in Section 3.1.9.

We are aware that any correction parameterization that we use initially may need evaluation and modification during the mission. Major solar storms may affect the accuracy of the electronics or the detectors. Unexpected thermal changes may cause offsets needed in the analysis of certain data. Infrequent corrections such as these, which may take the form of discontinuous changes rather than parameterized functions, may be deemed necessary by comparing redundant ESRs.

7.1 TIM Duty Cycling and Degradation Monitoring

On one orbit per week (a 1% duty cycle), the primary and secondary ESR's are used simultaneously to measure TSI. The secondary ESR has a lower rate of solar exposure and provides a stable monitor for correcting long-term variations in the primary ESR. The third ESR is used for one orbit every two weeks (0.5% duty cycle) and the fourth ESR for one orbit every 4 weeks (0.2% duty cycle) to similarly monitor long-term variations in the more frequently used ESRs. These modes are known as 'Degradation' modes and degradation that scales with exposure to sunlight will primarily affect the primary ESR. We expect these corrections to be small for TIM for the following reasons:

i. *NiP Black is robust.* As described in Section 3.1.1, this absorptive surface is caused by etching into the ESR cone interior surface, making the resulting surface mechanically robust.

ii. *Phase sensitive detection reduces sensitivity to long-term drifts* (Section 4.3.1). TIM analyzes only for changes in electrical power supplied to each ESR at and in phase with the shutter frequency. This reduces the instrument's sensitivity to long-term thermal drifts and degradations even before comparison to redundant ESRs.

iii. *The flight electrical standards are stable to a few ppm*.

7.2 SIM Duty Cycling and Degradation Monitoring

The long-term stability requirement for TSIS SIM is met through post-processing correction of on-orbit degradation in the instrument optics. There is an exposure time and wavelength dependent component to the degradation of optical transmission from damaging hard-radiation in space and this degradation is independently evaluated by periodic ESR measurements between the different channels.

Figure 22 shows a 24-hr timeline of nominal TSIS SIM operations. Table 10 describes the SIM instrument configuration during Channel A, B, and C comparison experiments. Tentatively, SIM B will be operated one orbit per day scanning a common wavelength region to SIM A that repeats every 17 days. SIM C will be operated same

as B with 17 scans over 17 days, but only twice per year (nominally, on the Vernal & Autumnal Equinox - 3/20 & 9/22 - to ensure common 1-AU and FOV conditions). Based on this measurement cadence, SIM A will acquire 196 minutes of solar exposure per day whereas SIM B will be at 19 min per day (~10% exposure duty-cycle). SIM C will only acquire ~650 minutes per year (~10% exposure of SIM B). The A-to-B comparisons will be used to determine the degradation correction.

For computing the degradation correction, it is assumed that a ratio of the integrated Channel A irradiance, I_A, over a wavelength interval (λ_i) to the integrated Channel B irradiance, I_B, over the *same* wavelength interval is proportional to the ratio of the prism degradation, $d(t_e)$, at that wavelength interval when the measurements are taken during the *same* solar viewing period, Sun_t (Equation 7.2.1). These measured ratios constrain a functional fit of the degradation with respect to cumulative exposure time, t_e, for each wavelength interval. A channel A-to-C calibration will be used as a check on the degradation correction.

$$\frac{I_A}{I_B} \propto \frac{\left(\frac{Sun_t}{d(t_e^A)}\right)}{\left(\frac{Sun_t}{d(t_e^B)}\right)} = \frac{d(t_e^B)}{d(t_e^A)} \tag{7.2.1}$$

The degradation function, for each λ_i, is determined over time with repeated Channel A to Channel B calibration scans. For example, if we assume an exponential decay in the prism transmission as a function of exposure time, we can determine a decay constant, α, for each wavelength interval.

Note, the exposure times will be corrected to 1-AU conditions to remove the variability in the signal that is due to changes in photon flux from the change in distance between the orbiting spacecraft and the Sun. Because the Sun's output is variable, even a 1-AU corrected solar exposure time will not be exactly equivalent to a photon "flux" exposure time. However, a degradation model based on solar exposure time will be the first approach to the analysis and continued monitoring will determine whether improvements in the degradation model must be made. For TSIS SIM operations, care was taken to match the cadence of Channel A and B exposures to best match common solar viewing conditions. There is no onboard way to monitor non-solar exposure related degradation.

The wavelength dependence of the prism degradation is determined by computing the functional fit of the degradation function at successive wavelength intervals. The degradation function is assumed to be the same for each wavelength interval but with a different decay constant α. The wavelength dependence of the prism degradation is a smooth function allowing us to interpolate the degradation at any wavelength. Figure 53 shows the SORCE SIM degradation function computed using the procedure described above, but using ESR "table scan" [*Harder et al*., 2005a] points between SIM A and SIM B ratios.

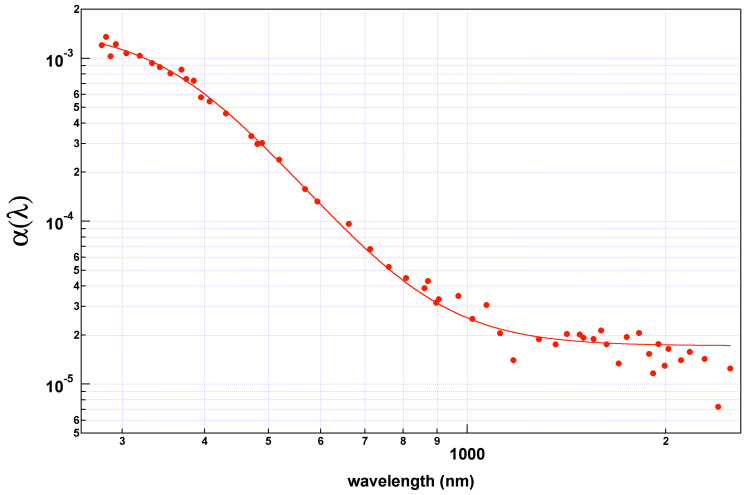

Figure 53: Measured wavelength dependence of prism transmission degradation for SORCE SIM.

The prism degradation function cannot be applied to correct the degradation for the measured photodiode irradiances because TSIS SIM is a refractive system. Each detector is affected by a different degradation, even if the wavelength interval is in common. By correcting the degradation in each ESR channel, we have a measure of the absolute solar irradiance for each measured wavelength interval. The measured photodiode irradiance within these same wavelength intervals will be corrected to give the same solar irradiance.

There are solar exposure and non-solar exposure dependencies in the degradation of the photodiode detectors. We track the solar exposure dependencies in the photodiode degradation in a similar manner as for the prism transmission by monitoring ratios of Channel A to Channel B photodiode measured irradiances over common wavelength intervals during the same solar viewing period. The exposure dependent functions will be unique to each photodiode detector. Corrections for the non-solar exposure dependencies in photodiode detector degradation will be performed by matching, over the common wavelength intervals and the same solar viewing period, the photodiode detector measurements with the absolute solar irradiance determined by ESR measurements.

Channel C is used infrequently enough that it can be considered “pristine”, or negligibly exposed, enabling the TSIS SIM instrument to measure solar spectral trends of less than 0.01% per year. Figure 54 provides a measure of the spectra-to-spectra repeatability for TSIS SIM.

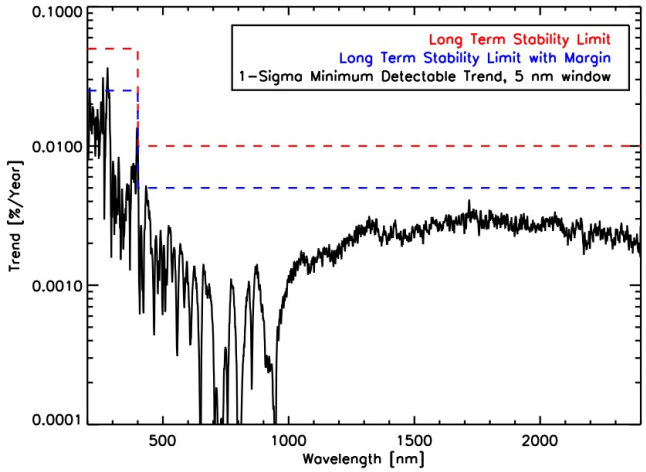

Figure 54: Expected TSIS SIM minimum detectable trends: The SIM Channel A to Channel C degradation uncertainty gives a measure of the minimum detectable trend versus wavelength.

8 Validation

8.1 General Discussion

The validation process is a subset of the both the science analysis and the data quality assurance. The TSIS Science Team oversees this process, which involves a careful examination of all solar data and judges the reasonableness and quality of the data to be released. The validation takes several different forms: 1) based on the confidence in the extensive pre-launch calibration and performance of the instruments in the TSI Radiometer Facility (TRF) and Spectral Radiometer Facility (SRF), 2) based on comparison with previous and simultaneous measurements from other instruments, 3) based on our understanding of the Sun and its variability — an understanding based on solar models and on solar observations at other wavelengths.

8.2 Confidence in Measurements

Through the TSIS pre-flight calibrations and characterization, coupled with in-flight characterizations and verification, the instrument scientists will establish a precision and uncertainty to be ascribed to each observation. This evaluation differs with each instrument and, for the case of SIM, may be a function of wavelength as well. Solar measurements should vary in a consistent manner from day to day, and from wavelength to wavelength. If an anomalous observation is detected, it will be evaluated against other observations.

8.3 Comparison with other Solar Measurements

When two or more independent measurements of the same source are compared, agreement is confirmed if the meaurements overlap within their stated uncertainties. Nevertheless, the magnitude of measurement offsets provides some guidance to possible sources of uncertainty. For example, regarding the comparison of TSI after the launch of SORCE in 2003, some of the instruments with high values were found to have a bias due to scattered light [*Kopp and Lean*, 2009].

There is no simple corrective action that should be taken in the event of measurement offsets. Resolution requires a close working relationship between the independent instrument teams to reconcile the results and to find the solution, much in the manner the TSI offsets were resolved in the SORCE era [Kopp and Lean, 2009]. When biases are found between the TSIS TSI or SSI measurements and other coincident measurements a closer examination of the TSIS uncertainty budget and possible sources of uncertainties will be undertaken. Differences must be reconciled within the uncertainty budgets of respective sensors.

The TSIS data will be compared to other solar measurements. At the time of this writing the future of international meaurements of solar irradiance is uncertain. The most promising overlap between independent TSI instruments is with the Compact and Lightweight Absolute Radiometer (CLARA), scheduled to be launched on NORSAT-1 in June, 2017. CLARA, built by PMOD/WRC, will measure TSI using three radiometer-channels that have been fully characterized and calibrated at the LASP TRF facility. Potential overlap with independent SSI instruments, especially those covering the near-full spectrum similar to TSIS SIM, is even more uncertain. The most-likely candidates for SSI comparisons will be OMI and GOME and SCIAMACHY follow-ons but these instruments do not provide SSI on an absolute scale. The launch opportunity for CSIM in late 2018 offers an additional comparison; this is particularly appealing because both TSIS SIM and CSIM are calibrated in the same facility establishing the same irradiance scale.

The primary activity for TSIS SSI and TSI comparisons will be with the SORCE TIM and SIM and the TCTE TIM if those instruments are still operating when TSIS completes commissioning. Additionally, if CSIM is operating we have a unique opportunity to overlap with common calibrated SSI instruments. Commonality in instrument design and heritage may accelerate resolution of measurement offsets in some cases; in others it may inhibit them.

Ultimately, interpretation of offsets will follow the discussion above: it will require a full examination of instrument error budgets and degradation analyses.

8.4 Quality Control and Diagnostic

The science production system supports both automatic and manual diagnostic statistical analyses of all science products. Deviations from expected or predicted values, flagging of anomalous values, and trends of many parameters and intermediate values, as well as final science values, are all incorporated into final or ancillary science data products. Quality flags in the final science products will be set both automatically and manually, via browse and other visualization tools. The highest quality level, indicating validated, definitive scientific results, must be set manually.

9 Data Product Requirements and Description

9.1 Overview

The TSIS data products are stored in a database. The results from the various processing levels are stored in separate tables. The data from the lower levels are used as inputs when processing the higher data levels.

9.2 TSIS Data Level Definitions

The various data levels used for TSIS are based on the *Earth Science Reference Handbook – A guide to NASA's Earth Science Program and Earth Observing Satellite Missions* [*available online at http://eospso.gsfc.nasa.gov/publications/56; last accessed 23 Oct 2013*]. The various data levels are briefly defined below.

- **Level 0**: Reconstructed, unprocessed instrument/payload data at full resolution; any and all communications artifacts, e.g., synchronization frames, communications headers, duplicate data removed.
- **Level 1A**: Reconstructed, unprocessed instrument data at full resolution, time-referenced, and annotated with ancillary information, including radiometric and geometric calibration coefficients and geo-referencing parameters, e.g., platform ephemeris, computed and appended but not applied to the Level 0 data.
- **Level 1B**: Level 1A data that have been processed to sensor (engineering) units.
- **Level 2**: Derived geophysical variables at the same resolution and location as the Level 1 source data with instrument/spacecraft signature removed. Useable science results at full spectral and temporal resolutions.
- **Level 3**: Temporal and / or spectral averaging of the Level 2 data. Data provided in standard geophysical units.

9.3 Level 2 Products

The Level 2 data consist of fully calibrated solar irradiances at the same temporal and spectral resolution as Level 1 data. The instrument and spacecraft signatures are removed, resulting in data in standard geophysical units (Watts/m^2 or Watts/m^2/nm). The data is generated within one day of receiving the latest Two-Line-Element (TLE) set from NORAD describing the orbital elements of the spacecraft. These are necessary to produce a calibrated data product at 1 AU with Doppler effects removed (see Section 4.2.3). The TLE sets are usually updated every day or so but sometimes it may take several days for an update. To make sure the best TLE is used, the Level 2 processing is delayed up to 7 days from the reception of Level 0 data.

9.4 Level 3 Products

The Level 3 data consist of daily and 6-hour average solar irradiances, with higher time resolution data available to meet secondary science objectives, such as studying the passage of bright faculae and dark sunspots across the visible surface of the Sun. The Level 3 data is interpolated to a pre-defined wavelength grid at full spectral resolution. This may result in a loss of spectral resolution at some wavelengths but has the benefit of providing data in a format most familiar to the scientific community.

Within 24 hours of Level 2 availability, all instrument science data and spacecraft engineering data are processed to derive Level 3 science data products in standard geophysical units (Watts/m^2 or Watts/m^2/nm). This data is made available to the scientific community through data distribution centers.

9.5 Practical Algorithm Considerations

9.5.1 Numerical Computation Considerations

The ground calibration of the TSIS instruments has resulted in a very good understanding of the instrument behavior and performance. The TSIS data processing system will access calibration data through look-up tables for most needs instead of running the full instrument model. This approach considerably improves the processing speed without affecting the accuracy of the processed data. The individual calibration data look-up tables are stored in separate database tables. It is expected that the TSIS instrument model will evolve with on-orbit monitoring instrument performance and behavior. Any subsequent adjustments to the instrument model will require the creation of new calibration look-up tables reflecting these changes. The new tables will be accessed as described above and under configuration management.

10 Production of Science Data

10.1 Overview

All science data production and management activities are provided by the LASP TSIS Science Data System, which resides at LASP in Boulder, Colorado. The TSIS Science Data System consists of both the hardware and software components necessary to capture, manage, process, analyze, validate, and distribute all science data products.

The TSIS Science Data System uses a relational database system, in which all telemetry, calibration data, scientific data products, and ancillary information are stored. All data are stored in the database as individual time-referenced points to provide direct and rapid access to each datum received from the spacecraft or instruments or subsequently processed.

The Science Data System consists of software applications, running on dedicated processing hardware, which read data from the database, compute scientific results, and writes them back to the database. From there, they are available to LASP scientists, and, through the LASP website, to the scientific community.

The TSIS Project Data Management Plan (ref. in Table 1) contains further descriptions of the data handling, design and heritage of the TSIS ground system and Science Operations Center, and data access and availability.

10.2 Data Management

All project data will be managed within a commercial relational database management system (DBMS). This system will maintain, under configuration control, all raw instrument and spacecraft data, engineering data products, science data products, calibration data necessary to produce science products, operations plans, and ancillary data.

Data security will be maintained using standard firewall and system security techniques, while integrity will be guaranteed by employing backup/recovery capabilities.

10.3 Data Processing

The TSIS Science Operations Center (SOC) has full responsibility for all science data production activities.

10.4 Data Structure

The data are stored within the database system as sets of tables. The tables contain, in the case of the SIM data, relational identifiers that allow the precedent data and calculations to be defined and managed by the database system itself. The TIM data tables are based on an older, time-stamp based design, used with SORCE.

10.5 Data Flow

Deliveries of Level 0 data to the SOC will occur at arbitrary times and consist of arbitrary numbers of un-ordered telemetry packets. The Level 0 ingest process will be triggered by these deliveries, and will consist of unpacking and decommutating telemetry frames, quality and limits checking, and population of Level 0 data tables.

It is expected that the delivery and ingest of all definitive Level 0 data (science, engineering, orbit, attitude, ephemeris) for a given calendar day will have been completed within 6 hours after the end of that day.

At regular intervals (6 hours or 24 hours), the processing of all Level 1 through Level 3 science products from recently completed intervals of Level 0 ingests will take place.

Figure 55 and Figure 56 outline the data processing flow for the SIM ESR and diode scans. Figure 57 shows the data processing for the TIM instrument.

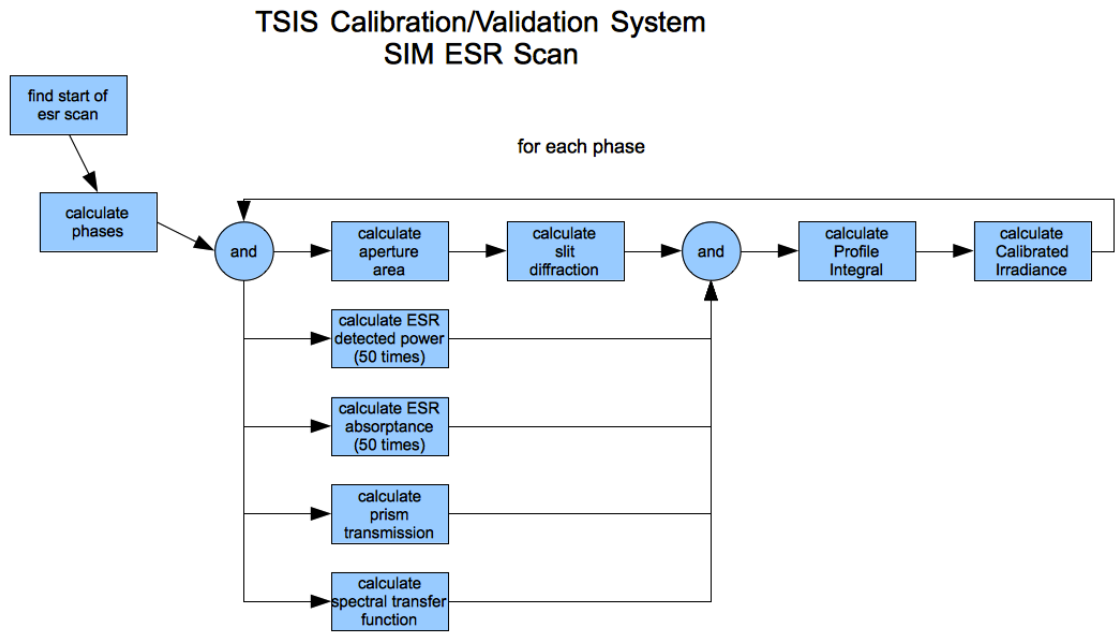

Figure 55: Data processing diagram for the production of SIM ESR data: The data processing system for the SIM ESR extracts the corresponding digital number (DN) from the raw data in-phase with the shutter open-close cycle. Average instrument temperatures are used to determine temperature correction effects in wavelength (the nonlinear dependent of index of refraction on temperature), prism transmission, slit diffraction, spectral transfer function, and the ESR absorptance. In a final step, the integrated instrument profile area is calculated and used to obtain the calibrated irradiance. More details on the SIM instrument, algorithm, and calibration can be found in Sections 3.2, 4.2.2, and 5.3, respectively. The phase sensitive detection was described in Section 4.3.

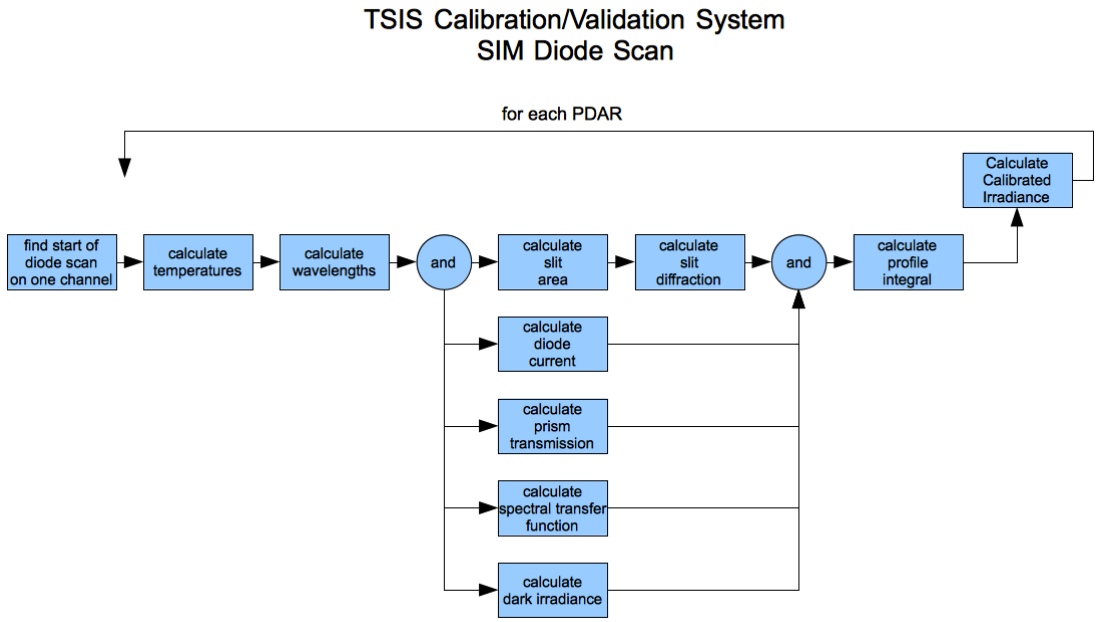

Figure 56: Data processing diagram for the production of SIM diode data: The data processing system for the SIM photodiode converts the Photodiode-Acquisition-Response (PDAR) time to a photodiode current. Average instrument temperatures are used to determine temperature correction effects in wavelength (the nonlinear dependent of index of refraction on temperature), prism transmission, slit diffraction, and the spectral transfer function. From measures of dark current before and after each scan, the dark current value for each PDAR is obtained by interpolation over the time of the scan. In a final step, the integrated instrument profile area for each PDAR is calculated and used to obtain the calibrated irradiance. The TSIS SIM PDAR detection was described in Sections 2.4.3.2 and 3.2.11. More details on the SIM instrument, algorithm, and calibration can be found in Sections 3.2, 4.2.2, and 5.3, respectively.

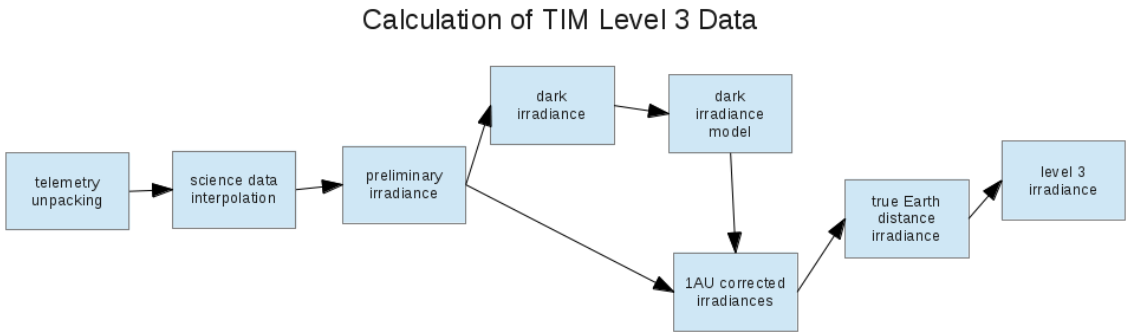

Figure 57: Data processing diagram for the production of TIM data.

10.6 Data Storage Considerations

All mission data will be stored within the LASP DBMS. This Oracle-based system is sized to handle data from many missions, and the TSIS data do not represent a significant strain on the existing system. Provisional storage of 1 terabyte has been allocated, with more available should it become necessary.

10.7 Configuration Management

10.7.1 Software Configuration Management

All software components of the TSIS Science Data System are managed within a software configuration management system. This ensures that all modifications to software are tracked. LASP system administration staff performs daily backups of the software repository.

10.7.2 Documentation Configuration Management

The processing systems for both TIM and SIM contain integrated documentation using Javadoc. Javadoc completely documents the data processing algorithms. This documentation is maintained under the same configuration system as the software, and is kept up to date with all algorithm changes.

10.7.3 Data Configuration Management

The data within the TSIS Science Data System are managed by the Oracle database. This provides complete support for transaction-based processing, password protection of data, and logging of data changes. The DBMS is maintained and operated by LASP system administration database analysts.

11 Appendix A Acronyms

ADC	Analog to Digital Converter
ATBD	Algorithm Theoretical Basis Document
AU	Astronomical Unit
BDRF	Bidirectional Reflectance Function
CCD	Charge Coupled Device
CU	University of Colorado, Boulder
DAAC	Distributed Active Archive Center
DAC	Digital to Analog Converter
DBMS	Database Management System
DN	Data Number
DSP	Digital Signal Processor
EOS	Earth Observing System
ESR	Electrical Substitution Radiometer
EUV	Extreme Ultraviolet
FOV	Field of View
FSS	Fine Sun Sensor
InGaAs	Indium gallium arsenide
ILS	Instrument Line Shape
IR	infrared
LASP	Laboratory for Atmospheric and Space Physics
MOC	Mission Operations Center
NIR	Near infrared
NiP	Nickel phosphorous
NIST	National Institute for Standards and Technology
NRLSSI	Navy Research Lab Solar Spectral Irradiance Model (J. Lean, 2000)
PDAR	Photodiode Acquisition Rate
POWR	NIST Primary Optical Watt radiometer
ppb	Parts per Billion
ppm	Parts per Million (10,000 ppm = 1%, 0.01% = 100ppm)
PWM	Pulse-width Modulation
RDBMS	Relational DBMS
rms	root mean square
SIM	Spectral Irradiance Monitor
SIRCUS	NIST Spectral Irradiance and Radiance responsivity Calibrations using Uniform Sources
SOC	Science Operations Center

SORCE	Solar Radiation and Climate Experiment
SURF	Synchrotron Ultraviolet Radiation Facility
SRF	Spectral Radiometer Facility
SSI	Spectral solar irradiance
SZA	Solar Zenith Angle
TCTE	TSI Calibration Transfer Experiment
TIM	Total Irradiance Monitor
TRF	TSI Radiometer Facility
TSI	Total solar irradiance
TSIS	Total Solar Irradiance Sensor
UARS	Upper Atmosphere Research Satellite
UV	Ultraviolet
VIS	Visible

13 Bibliography

Bailey, S. M., T. N. Woods, L. R. Canfield, R. Korde, C. A. Barth, S. C. Solomon, and G. J. Rottman, 1999, Sounding rocket measurements of the solar soft x-ray irradiance, *Solar Physics*, **186**, p. 243-257.

Bless, R. C., A. D. Code, and E. T. Fairchild, 1976, Ultraviolet photometry from the Orbiting Astronomical Observatory. XXI. Absolute energy distribution of stars in the ultraviolet, *Ap. J*. **203**, p. 410-416.

Bohlin, R. C., A. V. Holm, B. D. Savage, M. A. J. Snijders, and W. M. Sparks, 1980, Photometric calibration of the International Ultraviolet Explorer (IUE): Low Dispersion, *Astr. Ap*. **85**, p. 1-13.

Bohlin, R. C., D. Frimout, and C. F. Lillie, 1974, Absolute flux measurements in the rocket ultraviolet, *Astr. Ap*. **30**, p. 127-134.

Bretagnon, P. & Francou, G., 1988, Planetary theories in rectangular and spherical variables. VSOP87 solutions. *Astron. Astrophys*., **202**, p. 309-315.

Brueckner, G. E., K. L. Edlow, L. E. Floyd, J. L. Lean, and M. E. VanHoosier, 1993, The Solar Ultraviolet Spectral Irradiance Monitor (SUSIM) Experiment on Board the Upper Atmospheric Research Satellite (UARS), *J. Geophys. Res.*, **98**, p. 10695-10711.

Brune, W. H., G. H. Mount, and P. D. Feldman, 1979, Vacuum ultraviolet spectrophotometry and effective temperatures of hot stars, *Ap. J*., **227**, p. 884-899.

Canfield, L. R., J. Kerner and R. Korde, 1989, Stability and quantum efficiency performance of silicon photodiode detectors in the far ultraviolet, *Applied Optics*, **28**, 3940.

Canfield, L. R., R. Vest, T. N. Woods, and R. Korde, 1994, Silicon photodiodes with integrated thin film filters for selective bandpasses in the extreme ultraviolet, *SPIE Proceedings*, **2282**, p. 31-38.

Carruthers, G. R., H. M. Heckathorn, and C. B. Opal, 1981, Far-ultraviolet spectra and flux distributions of some orion stars, *Ap. J.,* **243**, p. 855-873.

Cebula, R. P. and E. Hilsenrath, 1996, SSBUV Measurements of Solar Spectral Irradiance Variations, 1989 - 1996, *EOS Trans. Amer. Geophys. Union,* **77**(46), Fall Meet. Suppl., 579.

Cebula, R. P., E. Hilsenrath, and M. T. DeLand, 1994, Middle ultraviolet solar spectral irradiance measurements, 1985-1992, from the SBUV/2 and the SSBUV instruments, in *The Sun as a Variable Star*, J.M. Pap, C. Fröhlich, H.S. Hudson, and S.K. Solanki, eds., Cambridge University Press, pp. 81-88.

Chapman, G. A., A. M. Cookson, and J. J. Dobias, 1996, Variations in the Total Solar Irradiance During Solar Cycle 22, *JGR*, **101**, A6, p. 13541-13548.

Cleveland, William S., 1985, *The Elements of Graphing Data*, Wadsworth Advanced Books, Monterey, CA.

Coddington, O., J. L. Lean, P. Pilewskie, M. Snow, and D. Lindholm (2016), A Solar Irradiance Climate Data Record, *B Am Meteorol Soc*, 97(7), 1265-1282, doi: 10.1175/Bams-D-14-00265.1.

de Boor, Carl, 1978, *A Practical Guide to Splines*, Springer-Verlag, New York.

Eddy, J. A., 1976, The Maunder Minimum, *Science*, **192**, 1189-1202.

Edlen, B., J. 1953, The dispersion of standard air, *J. Opt. Soc. Amer*., **43**, p. 339-344.

Féry, C, 1910, *Comptes Rendus*, 150, 216.

Feulner, G. (2011), Are the most recent estimates for Maunder Minimum solar irradiance in agreement with temperature reconstructions?, *Geophys Res Lett*, 38, doi: Artn L16706, 10.1029/2011gl048529.

Fontenla, J. M., J. Harder, G. Rottman, T. N. Woods, G. M. Lawrence, and S. Davis, 2004, The Signature of Solar Activity in the Infrared Spectral Irradiance, *AP. J. Lett*., **605**, 1.

Floyd, L. E., P. A. Reiser, P. C. Crane, L. C. Herring, D. K. Prinz, and G. E. Brueckner, 1998, SUSIM UARS measurements of solar cycle 22 UV irradiance variability, *Solar Physics*, **177**, p. 79-87.

Fröhlich, C., and the VIRGO team, 1997, First Results from the VIRGO, The Experiment for Helioseismology and solar irradiance monitoring on SOHO, *Solar Physics*, **170**, p. 1-25.

Fröhlich, C., 1994, *The Sun as a Variable Star*, editors: J. Pap, C. Fröhlich, H. Hudson, and S. Solanki, Cambridge Univ. Press, New York, pp. 28-36.

Fröhlich, C. and J. Lean, 1998, The Sun's Total Irradiance: Cycles, Trends and Related Climate Change Uncertainties since 1976, *J. Geophys. Res*., **25**, 23, p. 4377-4380.

Gray, L. J., J. Beer, J. D. Haigh, M. Lockwood, K. Matthes, U. Cubasch, D. Fleitmann, G. Harrison, L. Hood, J. Luterbacher, G. A. Meehl, D. Shindell, B. van G., W. White, 2010, Solar Influences on Climate, *Rev. Geophys*., **48**, 4.

Hansen, J. E., A. Lacis, D. Rind, G. Russell, P. Stone, I. Fung, R. Ruedy, and J. Lerner, 1994, Climate Sensitivity: analysis of feedback mechanisms, in *Climate Processes and Climate Sensitivity*, J. Hansen and T. Takahashi (eds.), American Geophysical Union, Wash., D.C.

Harber et al., 2006, Aperture edge scatter calibration of the cavity radiometers for the spaceflight Total Irradiance Monitor, *Earth Observing Systems XI*, Edited by James J. Butler, *Proceedings of the SPIE*, Volume 6296, pp. 62961I.

Harder, J. W., J. Fontenla, G. Lawrence, T. Woods, and G. Rottman, 2005, The Spectral Irradiance Monitor: Scientific Requirements: Measurement Equations and Calibration, *Solar Physics*, **230**, 1, p. 169-203.

Harder, J. W., J. Fontenla, O. White, G. Rottman, and T. Woods, 2005, Solar spectral irradiance variability comparisons of the SORCE SIM instrument with monitors of solar activity and spectral synthesis, *Mem. S. A. It*. **76**, 735.

Harder, J. W., G. Lawrence, G. Rottman, and T. Woods, 2000, The Spectral Irradiance Monitor (SIM) for the SORCE Mission, *Proc. SPIE*, **4135**, p. 204-124.

Harder, J. W., G. Lawrence, G. Rottman, and T. Woods, 2000, The Solar Spectral Irradiance Monitor: SIM, *Metrologia*, **37**, 5, doi: 10.1088/0026-1394/37/5/15.

Harder, J. W., G. Lawrence, J. Fontenla, G. Rottman, and T. Woods, 2005a, The Spectral Irradiance Monitor: Scientific requirements, instrument design, and operation modes, *Solar Physics*, **230**, p. 141-167.

Harder, J. W., J. Fontenla, G. Lawrence, T. Woods, and G. Rottman, 2005b, The Spectral Irradiance Monitor: Measurement Equations and Calibration, *Solar Physics*, **230**, p. 169-204.

Harder, J. W., J. M. Fontenla, P. Pilewskie, E. C. Richard, and T. N. Woods, 2009, Trends in solar spectral irradiance variability in the visible and infrared, *Geophys. Res. Lett*., **36**, L07801.

Harder, J. W., G. Thuillier, E. C. Richard, S. W. Brown, K. R. Lykke, M. Snow, W. E. McClintock, J. M. Fontenla, T. N. Woods, P. Pilewskie, 2010, The SORCE SIM Solar Spectrum: Comparison with Recent Observations, *Solar Physics*, **263**, 1-2.

Harvey, K., A. Mustico, and J. Vallimont, 1992, Effects of Long Term Space Environment Exposure on Optical Substrates and Coatings, *Proc. SPIE*, **1761**, p. 2-13.

Heath, D. F., and B. M. Schlesinger, 1986, The Mg 280-nm doublet as a monitor of changes in solar ultraviolet irradiance, *J. Geophys. Res*., **91**, p. 8672-8682.

Hengstberger, F., 1989, *Absolute Radiometry: Electrically Calibrated Thermal Detectors of Optical Radiation*, Edited by F. Hengstberger, Academic Press Inc., San Diego, CA.

Henry, R. C., A. Weinstein, P. D. Feldman, W. G. Fastie, and H. W. Moos, 1975, Low-resolution ultraviolet spectroscopy of several hot stars observed from Apollo 17, *Ap. J*., **201**, p. 613-623.

Heuerman et al., 2006, Calibration of the absorptance cavities for the spaceflight solar radiometer TIM, *Earth Observing Systems XI*. Edited by Butler, James J., *Proceedings of the SPIE*, Volume 6296, pp. 62961I.

Hickey, J., B. Alton, H. Kyle, and E. Major, 1987, Solar Irradiance Measurement by Nimbus-7 ERB Experiment: an Update of 100 Months, in *Solar Radiative Output Variation*, P. Foukal (editor), p. 189.

Hock, R., 2012, The Role of Solar Flares in the Variability of the Extreme Ultraviolet Solar Spectral Irradiance, Ph.D. thesis, University of Colorado at Boulder.

Holberg, J. B., W. T. Forrester, and D. E. Shemansky, 1982, Voyager absolute far-ultraviolet spectrophotometry of hot stars, *Ap. J*., **257**, 656-671.

Hood, L. L., 1991, Effects of Short-Term Solar UV Variability on the Stratosphere, *J. Atmos. Sol. Terr. Phys*., **61**, p. 45-51.

Jamar, C., D. Macau-Hercot, A. Monfils, G. I. Thompson, L. Houziaux, and R. Wilson, 1976, Ultraviolet Bright Star Spectrophotometric Catalogue, ESA SR-27.

Johnson, C. E., 1980, Ultra-Black Coating Due to Surface Morphology, U.S. Patent No. 4233107.

Kiehl, J., and K. Trenberth, 1997, Earth's Annual Global Mean Energy Budget, *Bull. Amer Meteor. Soc.,* **78**, p. 197-208.

Kopp, G. (2014), An assessment of the solar irradiance record for climate studies, *J Space Weather Spac*, 4, doi: ARTN A14, 10.1051/swsc/2014012.

Kopp, G., A. Fehlmann, W. Finsterle, D. Harber, K. Heuerman, and R. Willson, 2012, Total solar irradiance data record accuracy and consistency improvements, *Metrologia*, **49**, S29-S33.

Kopp, G., Heuerman, K., Harber, D., and Drake, V., 2007, The TSI Radiometer Facility - Absolute Calibrations for Total Solar Irradiance Instruments, *Proc. SPIE* 6677, 667709, doi:10.1117/12.734553.

Kopp, G., and G. Lawrence, 2005, The Total Irradiance Monitor (TIM): Instrument Design, *Solar Physics*, **230**, p. 91-109.

Kopp, G., and J. Lean, 2011, A new, lower value of total solar irradiance: Evidence and climate significance, *Geophys. Res., Lett*., **38**, L01706.

Kopp, G., and J. Lean, 2013, *The solar climate data record: scientific assessment of strategies to mitigate an impending gap in total solar irradiance observations between the NASA SORCE and NOAA TSIS missions (Study B)*, NRC Report solicited by NOAA NCDC.

Kopp, G., K. Heuerman, and G. Lawrence, 2005a, The Total Irradiance Monitor (TIM): Instrument Calibration, *Solar Physics*, **230**, p. 111-127.

Kopp, G., G. Lawrence, and G. Rottman, 2005b, The Total Irradiance Monitor (TIM): Science Results, *Solar Physics*, **230**, p. 129-139.

Korde, R. and L. R. Canfield, 1989, Silicon photodiodes with stable, near theoretical quantum efficiency in the soft x-ray region, *SPIE Proceeding*, **1140**, 126.

Korde, R., L. R. Canfield, and B Wallis, 1988, Stable high quantum efficiency silicon photodiodes for vacuum ultraviolet applications, *SPIE Proceeding*, **932**, 153.

Korde, R. and J. Geist, 1987, Quantum efficiency stability of silicon photodiodes, *Applied Optics*, **26**, 5284.

Kren, A. C., P. Pilewskie, and O. Coddington (2017), Where does Earth's atmosphere get its energy?, *J. Space Weather Space Clim.*, 7, A10, doi: 10.1051/swsc/2017007.

Kurucz, R. L., I. Furenlid, J. Brault, L. Testerman, 1984, Solar Flux Atlas from 296 to 1300 nm, National Solar Observatory Atlas, Sunspot, New Mexico: National Solar Observatory.

Kyle, H. L., D. V. Hoyt, J. R. Hickey, R. H. Maschoff, and G. J. Vallette, 1993, Nimbus-7 Earth Radiation Budget Calibration History - Part 1: The solar channels, *NASA Reference Publication,* **1316**.

Lawrence, G. M., Kopp, G., Rottman, G., Harder, J., Woods, T., and Loui, H., 2003, Calibration of the Total Irradiance Monitor, *Metrologia,* **40**, S78-S80.

Lawrence, G. M., G. Rottman , J. Harder, T. Woods, 2000, The solar Total Irradiance Monitor: TIM, *Metrologia*, **37**, p. 407-410.

Lawrence, G. M., J. Harder, G. Rottman, T. Woods, J. Richardson, G. Mount, 1998, Stability considerations for a solar Spectral Intensity Monitor (SIM), *SPIE Conference on Long-Term Degradation of Optical Systems*, San Diego, CA, **3427**.

Lawrence, G.M., G. Rottman, G. Kopp, J. Harder, W. McClintock, and T. Woods, 2000, The Total Irradiance Monitor (TIM) for the EOS SORCE Mission, *Earth Observing Systems V Proc. SPIE*, **4135**, 21, p. 215-224.

Lawson, Charles L., and Hanson, Richard J., 1974, *Solving Least Squares Problems* (esp. chap. 27). Prentice-Hall, Englewood Cliffs, NJ.

Lean, J. L., 2000, Evolution of the Sun's Spectral Irradiance Since the Maunder Minimum, *Geophys. Res. Lett*., **27**, 16, p. 2425-2428.

Lean, J. L., J. Beer, and R. Bradley, 1995, Reconstruction of solar irradiance since 1610: Implications for climate change, *Geophys*. *Res*. *Lett*., doi: 10.1029/95GL03093.

Lean, J. L., and D. Rind, 1998, Climate Forcing by Changing Solar Radiation, *J. Climate*, **11**, p. 3069-3094.

Lean, J. L., G. Rottman, H. Kyle, T. Woods, J. R. Hickey, and L. C. Puga, 1997, Detection and parameterization of variations in solar mid- and near-ultraviolet radiation (200-400 nm), *J. Geophys. Res*., **102**, p. 29939-29956.

Lean, J. L., G. Rottman, J. Harder, and G. Kopp, 2005, SORCE contributions to new understanding of global change and solar variability, *Solar Physics*, **230**, 27-53.

Lee, R. B., M. A. Gibson, R. S. Wilson, and S. Thimas, 1995, Long-term total solar irradiance variability during sunspot cycle 22, *J. Geophys. Res.,* **100**, p. 1667-1675.

Macau-Hercot, D., C. Jamar, A. Monfils, G. I. Thompson, L. Houziaux, and R. Wilson, 1978, Supplement to the Ultraviolet Bright Star Spectrophotometric Catalogue, ESA SR-28.

Malitson, I. H., 1965, Interspecimen comparison of the refractive index of fused silica, *J. Opt. Soc. Amer*., **55**, p. 1205-1209.

Meehl, G. A., J. M Arblaster, K. Matthes, F. Sassi, H. van Loon, 2009, Amplifying the Pacific Climate System Response to a Small 11-year Solar Cycle Forcing, *Science*, **28**, vol. 325, p. 1114-1118.

Merkel, A. W., J. W. Harder, D. R. Marsh, A. K. Smith, J. M. Fontenla, and T. N. Woods, 2011, The impact of solar spectral irradiance variability on middle atmospheric ozone, *Geophys. Res. Lett*., **38**, L13802, doi:10.1029/2011GL047561.

Mihalas, d., and J. Binney, 1981, *Galactic Astronomy Structure and Kinematics*, W. H. Freeman, New York, p. 135-139.

Moré, Jorge J., Gabow, Burton S., Hillstrom, Kenneth E., 1980, *User Guide For Minpack-1*, Argonne National Laboratory, Argonne, Ill.

Parkinson, C. L., A. Ward, and M. D. King (editors), 2006, Earth Science Reference Handbook, A guide to NASA's Earth Science Program and Earth Observing Satellite Missions, National Aeronautics and Space Administration, Washington, D. C.

Pilewskie, P., G. Rottman, and E. Richard, 2005, An Overview of the Disposition of Solar Radiation in the Lower Atmosphere: Connections to the SORCE Mission and Climate Change, *Solar Phys*., **230**, p. 55-69.

Powell, F. R., P. W. Vedder, J. F. Lindblom, S. F. Powell, 1990, Thin film filter performance for extreme ultraviolet and x-ray applications, *Optical Eng*., **26**, 614.

Reid. G. C., 1991, Solar total irradiance variations and the global sea surface temperature record, *J. Geophys. Res*., **96**, p. 2835-2844.

Reid, G. C., 1997, Solar forcing and global climate change since the mid-17th century, *Climatic Change*, **37**, p. 391-405.

Reid, G. C., 1999, Solar Variability and its Implications for the Human Environment, *J. Atmos. Sol. Terr. Phys*., **61**, p. 3-14.

Rottman, G., 1988, Observations of solar UV and EUV variability, *Adv. Space Res*., **8**, 7, p. 53-66.

Rottman, G., 2006, Measurement of Total and Spectral Solar Irradiance, *Space Science Rev*., **125**, 1-4, p. 39-51.

Rottman, G., G. Mount, G. Lawrence, T. Woods, J. Harder, S. Tournois, 1998, Solar spectral irradiance measurements: visible to near infrared, NEWRAD'97, *Metrologia*, **35**, p. 707-712.

Rottman, G. J., T. N. Woods, 1995, SOLSTICE technique for measuring long-term solar variability, *Proc. SPIE* Vol. 2583, Advanced and Next-Generation Satellites, Hiroyuki Fujisada and Martin N. Sweeting (Editors), p. 347-355.

Rottman, G. J., T. N. Woods, and T. P. Sparn, 1993, SOLar STellar Irradiance Comparison Experiment 1: 1. Instrument design and operation, *J. Geophys. Res*., **98**, p. 10,667-10,677.

Rottman, G. J., C. A. Barth, R. J. Thomas, G. H. Mount, G. M. Lawrence, D. W. Rusch, R. W. Sanders, G. E. Thomas and J. London, 1982, Solar Spectral Irradiance, 120 to 190nm, October 13, 1981 - January 3, 1982, *Geophys. Res. Letters*, **9**, p. 587-590.

Rottman, G., J. Harder, J. Fontenla, T. Woods, O. R. White, and G. Lawrence, 2005, The Spectral Irradiance Monitor (SIM): Early Observations, *Solar Physics*, **230**, p. 205-224.

Schmutz, W., A. Fehlmann, G. Hülsen, P. Meindl, R. Winkler, G. Thuillier, P. Blattner, F. Buisson, T. Egorova, W. Finsterle, N. Fox, J. Gröbner, J. –F. Hochedez, S. Koller, M. Meftah, M. Meisonnier, S. Nyeki, D. Pfiffner, H. Roth, E. Rozanov, M. Spescha, C. Wehrli, L. Werner, and J. U. Wyss, 2009, The PREMOS/PICARD instrument calibration, *Metrologia*, **46**, 4.

Sellers, W. D., 1965: Physical Climatology. Chicago: University of Chicago Press

Shapiro, A. I., W. Schmutz, E. Rozanov, M. Schoell, M. Haberreiter, A. V. Shapiro, and S. Nyeki (2011), A new approach to the long-term reconstruction of the solar irradiance leads to large historical solar forcing, *Astron Astrophys*, 529, doi: Artn A67, 10.1051/0004-6361/201016173.

Solanki S., and Y. Unruh, 1998, A Model of the Wavelength Dependence of Solar Irradiance Variations, *Astron. Astrophys*., **329**, p. 747-753.

Solomon, S. C., C. A. Barth, P. Axelrad, S. M. Bailey, R. Brown, R. L. Davis, T. E. Holden, R. A. Kohnert, F. W. Lacy, M. T. McGrath, D. C. O'Connor, J. P. Perich, H. L. Reed, M. A. Salada, J. Simpson, J. M. Srinivasan, G. A. Stafford, S. R. Steg, G. A. Tate, J. C. Westfall, N. R. White, P. R. Withnell, and T. N. Woods, 1996, The Student Nitric Oxide Explorer, *SPIE Proceedings*, **2810**, p. 121-132.

Standish, E.M., 1982, Orientation of the JPL Ephemerides, DE200/LE200, to the Dynamical Equinox of J2000, Astronomy & Astrophysics, **114**, p. 297-302.

Standish, E.M., 1990, The Observational Basis for JPL's DE200, the planetary ephemeris of the Astronomical Almanac, *Astronomy & Astrophysics*, **233**, p. 252-271.

Stephens, G. L., J. L. Li, M. Wild, C. A. Clayson, N. Loeb, S. Kato, T. L'Ecuyer, P. W. Stackhouse, M. Lebsock, and T. Andrews (2012), An update on Earth's energy balance in light of the latest global observations, *Nat Geosci*, 5(10), 691-696, doi: 10.1038/Ngeo1580.

Stronglyis, G. J. and R. C. Bohlin, 1979, Absolute calibration in the 1750 Å - 3350 Å region, *Publ. Astron. Soc. of Pacific*, p. 205-213.

Tennyson, P.D., P. D. Feldman, and R. C. Henry, 1987, Search for ultraviolet shuttle glow, *Adv. Space Res*., **7**, 207-210.

Thuillier, G., M. Herse, P. Simon, D. Labs, H. Mandel, and D. Gillotay, 1998, Observation of the UV Solar Spectral Irradiance between 200 and 360 nm during the ATLAS-1 Mission by the SOLSPEC Spectrometer, *Solar Physics,* **177**, p. 41-61.

Trenberth, K., J. T. Fasullo, and J. Kiehl, 2009, Earth's Global Energy Budget, *Bull. Amer. Meteor. Soc*., **90**, p. 311-323.

Tropf, W. J. and Thomas M. E., 1998, Infared Refractive Index and Thermo-optic Coefficient Measurement at APL, APL Technical Digest, vol.19, number 3.

Usoskin, I. G., 2013, A History of Solar Activity over Millennia, *Living Rev. Solar Phys*., **10**, 1.

VanHoosier, M, J. Bartoe, G. Brueckner, and D. Prinz, 1988, Absolute Solar Spectral Irradiance 120 nm – 400 nm (Results from the Solar Ultraviolet Spectral Irradiance Monitor –SUSIM-Experiment on Spacelab 2), *Astro. Lett. and Communications,* **27**, p. 163-168.

Warren, D. W., J. A. Hackwell, and D. J. Gutierrez, 1997, Compact prism spectrograph based on aplanatic principles, *Optical Engineering*, **36**, p. 1174-1182.

White, O. R. and W. Livingston, 1978, Solar luminosity variation. II. Behavior of Calcium H and K at solar minimum and the onset of cycle 21, *Ap. J*, **226**, p. 679-686.

White, O. R., G. J. Rottman, T. N. Woods, S. I. Keil, W. C. Livingston, K. F. Tapping, R. F. Donnelly, and L. Puga, 1994, Change in the UV Output of the Sun in 1992 and its Effect in the Thermosphere, *J. Geophys. Res*., **99**, p. 369-372.

Wild, M., D. Folini, C. Schar, N. Loeb, E. G. Dutton, and G. Konig-Langlo (2013), The global energy balance from a surface perspective, *Clim Dynam*, 40(11-12), 3107-3134, doi: 10.1007/s00382-012-1569-8.

Willson, R. C., 1977, Total Solar Irradiance Trend in Solar Cycles 21 and 22, *Science,* **277**.

Willson, R. C., 1994, Irradiance observations of SMM, Spacelab-1, UARS, and ATLAS Experiments, *The Sun as a Variable Star*, editors: J. Pap, C. Fröhlich, H. Hudson, and S. Solanki, Cambridge Univ. Press, New York, p. 54-62.

Willson, R. C., 1984, Measurement of Solar Total Irradiance and its Variability, *Space Sci. Rev*., **38**, p. 203-242.

Willson, R. C., The ACRIMSAT/ACRIM3 Experiment—Extending the Precision, Long-Term Total Solar Irradiance Climate Database, Earth Observ., 13, 14– 17, 2001.

Woods, T. N., G. J. Rottman, S. M. Bailey, S. C. Solomon, and J. Worden, 1998a, Solar extreme ultraviolet irradiance measurements during solar cycle 22, *Solar Physics*, **177**, p. 133-146.

Woods, T., G. Rottman, J. Harder, G. Lawrence, W. McClintock, G. Kopp, and C. Pankratz, C., 2000, Overview of the EOS SORCE Mission, *SPIE,* **4135**, p. 192-203.

Woods, T. N., F. G. Eparvier, S. M. Bailey, S. C. Solomon, G. J. Rottman, G. M. Lawrence, R. G. Roble, O. R. White, J. Lean, and W. K. Tobiska, 1998b, TIMED Solar EUV Experiment, *SPIE Proceedings*, **3442**, p. 180-191.

Woods, T. N., F. G. Eparvier, J. Fontenla, J. Harder, G. Kopp, W. E. McClintock, G. Rottman, B. Smiley, and M. Snow, 2004, Solar irradiance variability during the October 2003 solar storm period, *Geophys. Res. Lett*., **31**, 10.

Woods, T. N., D. K. Prinz, J. London, G. J. Rottman, P. C. Crane, R. P. Cebula, E. Hilsenrath, G. E. Brueckner, M. D. Andrews, O. R. White, M. E. VanHoosier, L. E. Floyd, L. C. Herring, B. G. Knapp, C. K. Pankratz, and P. A. Reiser, 1996, Validation of the UARS solar ultraviolet irradiances: Comparison with the ATLAS 1 and 2 measurements, *J. Geophys. Res*., **101**, p. 9541-9569.

Woods, T. N., R. T. Wrigley, G. J. Rottman and R. E. Haring, 1994, Scattered light properties of diffraction gratings, *Applied Optics*, **33**, p. 4273-4285.

Woods, T. N., G. J. Rottman, and G. Ucker, 1993, Solar Stellar Irradiance Comparison Experiment I: 2 Instrument Calibration, *J. Geophys. Res*., **98**, p. 10,679-10,694.

Woods, T. N. and G. J. Rottman, 1990, Solar EUV irradiance derived from a sounding rocket experiment on 10 November 1988, *J. Geophys. Res*., **95**, p. 6227-6236.

Woods, T. N., P. D. Feldman, and G. H. Bruner, 1985, The absolute flux of six hot stars in the ultraviolet (912-1600 Å), *Ap. J*., **292**, p. 676-686.